Università degli Studi di Roma "La Sapienza"

Facoltà di Scienze Matematiche Fisiche e Naturali

Tesi di Dottorato in Scienza dei Materiali

(XVII ciclo)

Functionalization of c-Silicon surfaces for nanoscopic devices

Relatore :
Prof. C. Coluzza

Dottorando :
Giovanni Di Santo

Coordinatore del Dottorato
Prof. M. Capizzi

A. A. 2003-2004

“Studia prima la scienza, e poi seguita la pratica, nata da essa scienza. Quelli che s’innamoran di pratica senza scienza son come ’l nocchier ch’entra in navilio senza timone o bussola, che mai ha certezza dove si vada”

“First study science, then do practice, born from science itself. Those who loves most practice without science are like a seaman who sails without helm or compass, never being sure of destination”

LEONARDO DA VINCI

Introduction

In this work we will present and discuss experimental results of our surface study on Silicon functionalization with organic molecules by wet chemistry approach. Presently Individual molecules are hundreds of times smaller than the smallest features conceivably attainable by semiconductor technology. Different kind of molecules has been studied particularly for their possibilities of self-assembling on metals. The goal of the basic and applied studies on the new “molecular electronics” is to find the conditions for a certain molecular specie to be able to self-assemble and to communicate with semiconductors. That’s why several publications have addressed, in the last decade, the issue of organic derivatization of silicon surfaces. Molecular organizing is indeed a fine modification of a Si surface. It makes possible the functionalization by specific molecular acceptors and the device development on the nanometer scale [**2**].

The substrates chosen for this work where hydrogenated n- and p-type Si(100) surfaces, being the hydrogenation, at first step, a way to protect the reactive Si bare surface from immediate oxidation. The molecules under investigation are several types of ferrocenes and alkyl chains molecules, in both cases with functional groups to be anchored on Si(100). The localization of these anchoring species, in the microscopic and nanoscopic scale, makes necessary the use of several spectro-microscopic techniques. AFM, XPS are used to characterize the morphology and the chemical composition of the hybrid surfaces which was tested from electrochemistry measurements to be a a promising molecular switching device (ferrocenes). Syncrothron radiation spectro-microscopy experiments investigate the homogeneity of functionalized surfaces. Moreover the development of novel techniques such as Mercury drop soft contacts for electrical characterization of the hybrids (alkyl chains molecules)

allows to extract informations both on the stability and activity of such modified surfaces. Barrier height and ideality factor measurements are extracted from current-voltage characteristics on mercury/silicon and mercury/molecule/silicon junctions, while photocurrent threshold are measured by internal photoemission experiment.

In the following points are summarized the main parts of this thesis:

- ⋆ description of the actual research status on the specific field of Si functionalization (chapter 1);
- ⋆ presentation of our measurements apparatus, of experimental techniques used to characterize samples and their preparation procedure (chapter 2);
- ⋆ presentation and discussion about the results (chapter 3 and 4).

Contents

Introduction 2

Chapter 1. Semiconductor Surface and Functionalization 6

1.1. Development of semiconductor technology 6

1.2. Molecular Electronics 9

1.3. Surface and Interfaces studies 12

1.4. Scanning Probe Microscopy 15

1.5. X-ray Photoemission Spectroscopy 19

1.6. Spectromicroscopy 31

1.7. Mercury-drop electrode and IPE 34

Chapter 2. Experimental Apparatus and sample preparation 42

2.1. UHV System: setting up 42

2.2. AFM-STM 44

2.3. Spectromicroscopy with PEEM and SR 52

2.4. Mercury-Silicon junction apparatus 55

2.5. IPE experimental setup 57

2.6. The substrate: Si(100) 57

2.7. Wet Chemistry process 58

Chapter 3. Ferrocenes on Si 66

3.1. Ferrocene on Si: Introduction 66

3.2. VFC/Si: AFM 69

3.3. FCE/Si: AFM 71

3.4. VFC/Si: XPS 74

3.5. Selected Ferrocenes on Si: XPS study 81

3.6. VFC/Si: Spectromicroscopy 85

Chapter 4. Alkyl chains on Si 87

4.1. Alkyl chains on Si: XPS 87

4.2. Alkyl chains on Si: I-V characteristics 88

4.3. Molecule induced junction behavior 88

4.4. Barrier height measurement 91

4.5. IPE experiment 92

Conclusion 95

Bibliography 96

CHAPTER 1

Semiconductor Surface and Functionalization

1.1. Development of semiconductor technology

Semiconductor technology has been the most important research field in materials science for the last 50 years. Many efforts and consequent results has been put on semiconductors since the invention of the transistor. A line has been drawn from the beginning and it is nowadays followed as well as before: it is related to decreasing of devices components dimensions and it lead to micro- and nano-electronics.

The field of microelectronics began in 1948 when the first transistor was invented. This first transistor was a point-contact transistor, which became obsolete in the 1950s following the development of the bipolar junction transistor (BJT). The first modern day junction field-effect transistor (JFET) was proposed by Shockley (1952) [**1**]. Since the early 60's these devices has been developed and their principle of operation are in the heart of almost every electronic device we have around us, but it was the development of integrated circuits (ICs) in 1958 that spawned todays computer industry.

The other factor, of not less importance, in the development of solid state devices is the miniaturization of such devices. In the last decades the number of transistors in a microprocessor (chip) of fixed dimensions was always increasing. Indeed the evolution of digital technology followed the well-known Moore's Law, which states that *"every eighteen to twenty four months, for the foreseeable future, chip density and hence computing power would double while cost remained constant"*(see fig. 1.1). We have good evidence that since 1960's the evolution of computer technology has strictly followed this law. The implication from the point of view of material science is that both the knowledge about smaller dimension devices and

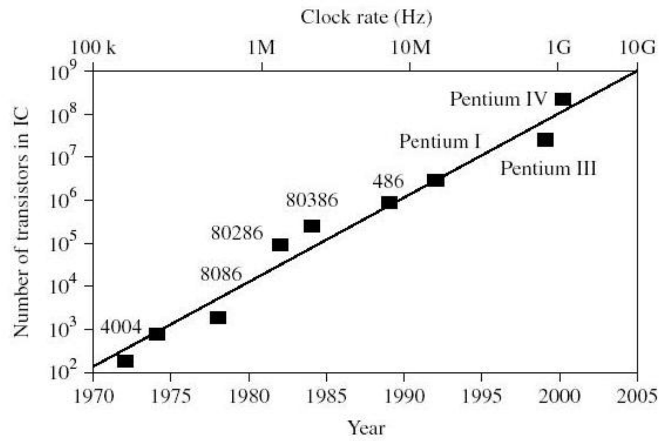

FIGURE 1.1. Moore's law for integrated circuits: exponential growth in the number of transistors in an IC during the past 30 years.

the scientific tools to study them had to follow that trend. Anyway the Moore's law has its limit in the definite dimensions of atoms and molecules.

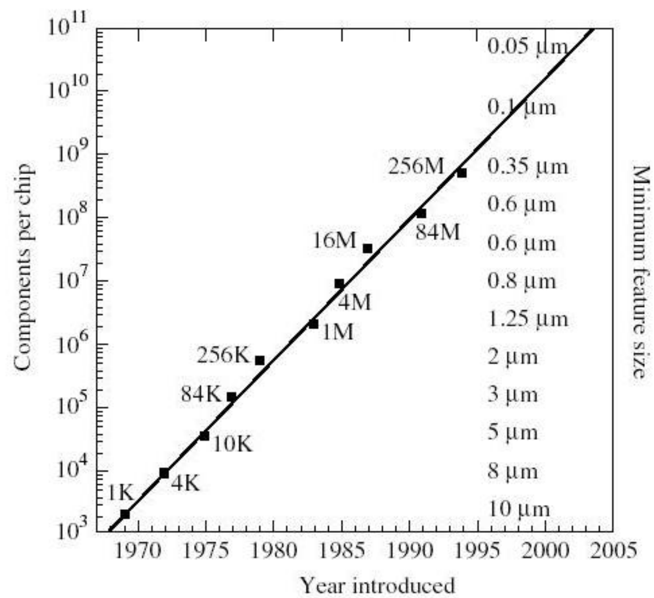

FIGURE 1.2. Size of memory chips (DRAM) and minimum feature size as a function of time. From Campbell (1996) [**3**].

As it can be seen in fig 1.2 the minimum features size of IC elementary components is going to reach in these years the low nanometer scale. We are dealing with blocks that cannot be built using the "classical" lithographic techniques. A single molecule

is not enough for an electronic signal so the building blocks of the future ICs are objects consisting of small groups of atoms or molecules equivalent each others. From this point of view in the last years increasing attention has been paid to systems of atoms or molecules with self-assembling properties. Hundreds of different kind of molecules has been studied particularly for their possibilities of self-assembling on metals. The goal of the basic and applied studies on the new "molecular electronics" is to find the conditions for a certain molecular specie to be able to self-assemble and to communicate with semiconductors better than with metals. Surface functionalization started to be one of the most used technique for the preparation of interfaces between semiconductors and organic species. Generally a semiconductor surface need to be prepared for anchoring a certain molecule with a coverage ratio as high as possible.

Molecular self-assembling on a substrate like Si is a fine modification of the surface. It makes possible the functionalization by specific molecular acceptors and the device development on the nanometer scale [**2**]. Moreover the localization of anchoring species both in space and time makes necessary the use of several spectromicroscopic techniques. The results of recent studies already had several applications dealing with corrosion, chemical and biological sensors, photolithography.

The main purposes of the present work are:

- ⋆ to product new materials via chemical reactions, in solution, with organic molecules [**5**], that are modified to be berthed by covalent bonds and in some case to have self-assembling properties;
- ⋆ to anchor the chosen species on Silicon substrates, prepared by synthetic methods;
- ⋆ to study as deeply as possible these new systems by spectroscopic and microscopic techniques and investigate their charge transfer properties by means of novel tools.

The goal is to have the possibility to control these materials as “two step devices” (molecular switch) or to reveal their modifications in certain conditions, then use them as molecular sensors.

1.2. Molecular Electronics

The field of molecular electronics seeks to use individual molecules to perform functions in electronic circuitry performed by semiconductor devices. Individual molecules are hundreds of times smaller than the smallest features conceivably attainable by semiconductor technology. Because it is the area taken up by each electronic element that matters, electronic devices constructed from molecules will be hundreds of times smaller than their semiconductor-based counterparts. Moreover, individual molecules are easily made exactly the same by the billions and trillions. The dramatic reduction in size, and the sheer enormity of numbers in manufacture, are the outstanding benefits offered by the field of molecular electronics [**4**].

Several publications have addressed, in the last decade, the issue of organic derivatization of silicon surfaces, mainly in view of their potential applications in different fields, as molecular electronics, dielectric films, sensoring.[**6**][**7**] Basic issues of momentum importance are still open, notably the role played by the presence of a covalent bond, established between organic moiety and silicon, in determining the hybrid chemical behaviour, its electronic addressability and robustness.[**8**][**9**] A few recipes for a covalent molecular anchoring on silicon have been reported, sometimes associated with claims of a superior and long-term stability of the $Si-C$ bond in hydrolytic conditions, which instead severely affects $Si-O-R$ bonds.[**7**][**8**][**10, 11**] The electronic communication between silicon substrate and attached molecules has also been tested, mainly by means of electrochemical methods in a solution[**9**][**12, 13**] and, in a limited number of cases, in the solid state[**14, 15**], and the importance of the nature of the contact has been discussed. However, it has not yet been clarified in the literature on Si-organics hybrids, if the roadmap to robust and reliable Si

based molecular electronics should select one among the existing Si-organics covalent bond already tested (mainly $Si-C$, $Si-O$, $Si-P$), or explore futher ones. Part of the uncertainty could also come from a limited knowledge, from the point of view of surface science, of the resulting hybrids and of their reactivity in operating conditions. The heart of the hybrid being the peculiar molecular functionality, it has to be assessed if the molecular nature is maintained through use of the hybrid. In a wider view, it is crucial to assess the quality of the hybrid from the two sides: the molecule and the substrate, not only at the stage of as prepared species but also upon/after its use.

Some of these issues have been addressed here, by selecting a commercial molecule, vinylferrocene (VFC), as the starting material for the deposition of molecular electroactive monolayers, covalently anchored on the surface of H-terminated $Si(100)$ through wet-chemistry methods. The electrochemical properties of free and anchored ferrocene and substituted ferrocenes have been deeply investigated in the last 50 years. More recently, ferrocenes have been proposed among the more suitable anchored electroactive species in molecular electronics, mainly due to well known advantages in terms of chemical and thermal stability, robustness and reversible cyclability of the ferrocene/ferrocenium redox couple, wide synthetic availability of substituted ferrocene analogues and tunability of the corresponding redox potential [**9**][**16**].

The step from charge *storage* systems to charge *transfer* system has been done by the substitution of ferrocene with alkyl chains molecules. The coverage of Si surface by these species is now very efficient, so their use as molecular wires for charge conduction is promising to be effective. However in this case there is a big difference with charge storage molecules, like ferrocenes: charge can only be transferred through but not collected by them. The easiest way to get rid of this problem was to include the molecule mono/multi-layer into metal-semiconductor junctions. A novel study technique has been designed recently to fulfill this goal: a soft metal contact by mercury micro-drop can easily be done on the alkyl layer berthed on Si

[**17**]. Current-voltage characteristics give informations on the transport mechanisms at the junction. It is indeed a real metal-insulator-semiconductor (MIS) junction where the insulator is very thin (few tens of Å).

The metal-semiconductor (M-S) junction is one of the most important solid-state components in microelectronic integrated circuits. It has been widely used in creating Ohmic contacts, Schottky diodes, and M-S field-effect transistors. The fabrication and characterization of these junctions directly affect the process, characteristics, and performance of these important devices. With the emergence of molecular modification and self-assembly techniques, research activities have been bolstered with the aim of obtaining a full understanding of the formation of metal/molecule/semiconductor junctions and the molecular tunablility of interfaces. The understanding of the exact electrical properties of oxide-free metal/molecule/silicon junctions is still very limited. In contrast, great progress has been made during the past decade in the fabrication and application of chemically robust Si-C bonded monolayers on silicon. It has been reported how an alkyl monolayer can tune a resistor (such as a direct mercury/silicon contact) to a diode (to a mercury/molecule/silicon junction), and described how the electron transport correlates to the device performance in these genuine metal/molecule/semiconductor junctions [**17**]. The use of mercury as a soft metal contact, initiated 30 years ago [**18**], has regained its popularity in the recent studies of the unique electron transport property across metal/monolayer/ metal junctions [**19**], and the intriguing electrical behavior of Hg/monolayer/SiOx/p-Si systems. Moreover by using monochromatic light, in the visible and near infra-red range, as a pumping probe for controlling the transport mechanisms it is possible to get accurate measurements on the interface properties. Internal photoemission (IPE) studies allow to measure the exact value of the barrier height ϕ_b at the junction interface. Moreover by the analysis of IPE spectra it is possible to recognize interface states, mainly due to defects, which deeply affect the conduction mechanisms over the junction. A key parameter determining the opto-electronic properties of a semiconductor is its energy gap: IPE technique can easily

offer evidence of those states "living" inside the band gap and/or tell us if organics adsorbates can interact with them, which is very important for the understanding of hybrid molecule-semiconductor interfaces.

1.3. Surface and Interfaces studies

However there are several open problems in the understanding of the mechanisms with which molecular blocks "talk" with Silicon. The explanation of these hybrid devices behavior are achievable by surface techniques: core level spectroscopy and scanning probe microscopy with the support of other spectro-microscopic techniques tell us about chemical bonds and morphological structures; transport measurements by soft metal contact (Hg drop electrode) both with $I-V$ characteristics and IPE studies open the way to the understanding of charge transfer mechanism between semiconductors, especially Si, and molecules, which is one of the aims of molecular electronics.

1.3.1. Electrochemistry results on Ferrocenes draw the line... Representative cyclic voltammograms (cv) for vinylferrocene on silicon (VFC/p-Si(100)) are shown in Fig. 1.3(a). The electrolyte solution contained no deliberately added electroactive species, and the voltammetric peaks can be unambiguously attributed to the attached redox species.

The electrode potential was scanned from the lower to the higher limit and back, at scan rates varying from 1 to 9 V/s, inducing the reversible oxidation of the ferrocene derivative group. The cvs were run in the dark and under laser light, and no difference was found. The scan rate dependence of cv was further analyzed. As can be inferred from inspection of Fig. 1.3(b), the anodic and cathodic peak currents were found to scale linearly with the scan rate v rather than with $v^{1/2}$, indicating a surface redox process. Furthermore, this trend is characteristic of a reversible (Nernstian) electrochemical process, wherein the relative activity of the ferrocene and ferrocenium sites is uniform throughout the film and at equilibrium with each applied electrode potential. According to such an electroactive species

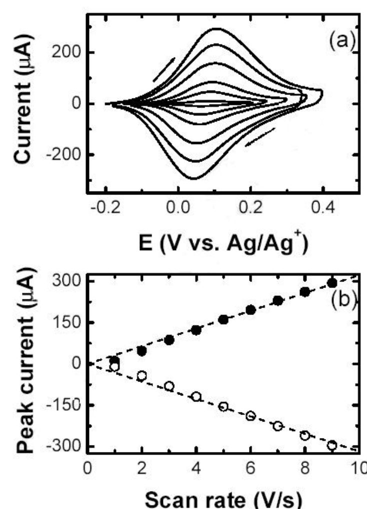

FIGURE 1.3. Representative cyclic voltammograms of a VFC/p-Si(100) functionalized electrode as a function of the potential scan rate. (b) Anodic (•) and cathodic (∘) peak currents as a function of cyclic voltammetry scan rate, obtained from Fig. 1.3a. Dashed lines correspond to linear fittings, with correlation coefficients of 0.9999.

confinement at the Si electrode surface, diffusion plays no role in current control. Peak currents are then directly proportional to the scan rate, as is given by

$$I_{peak} = n^2 F^2 v A \Gamma (4RT)^{-1} \tag{1.1}$$

where n is the number of electrons, F is the Faraday constant, v is the scan rate (V/s), A is the electrode surface area (cm^2), Γ is the surface coverage in moles of attached molecules per unit surface area, R and T have their usual meanings.

The surface coverage of the covalently attached molecules can be determined by either using the scan-rate dependence of the anodic and cathodic peak currents via the above equation, or directly integrating the voltammetric waves. The first procedure yields surface coverage values of 1.0×10^{-10} $mol\ cm^{-2}$ for the VFC/p-Si(100) monolayer, taking for A the geometric area of the electrode. Note in Figure 4(a) that the difference between the peak potential of the anodic and cathodic peaks, ΔE_{pp}, increases with the scan rate. These values differ from the zero (and

independent of scan rate) peak-to-peak separation theoretically predicted for an ideal surface-confined redox couple.[**20**] The increase in peak splitting indicates that the scan rate becomes comparable to the electron transfer rate at higher sweep speeds. ΔE_{pp} was found to scale linearly with $ln(v)$ at high scan rates. From the peak-to-peak separation values in these cvs, the standard electron transfer rate constants, k_0, were obtained, according to Lavirons approach for the reaction of electroactive species immobilized onto an electrode surface [**20**]. In spite of the fact that the voltammetric waves for $p - Si(100)/VFC$ were quite persistent to repeated oxidation-reduction reaction (over 1000 cycles), the ΔE_{pp} increases with the number of redox cycles performed, suggesting a progressive departure from reaction reversibility. At the same time, also the redox capacitance of the monolayer drops with ageing. Both results indicate that the electron transfer rate constant decreases with electrode ageing, and this has been interpreted as due to the hindrance to the motion of the counter-ions by the growing Si oxide layer. These results demonstrate that silicon surfaces can be modified with VFC which have the capability to cycle from two definite redox states being chemically berthed to the surface. This can be addressed as one of the example of working *molecular switch* system bonded to the surface of a semiconductor widely used as Si.

However even without suffering substantial loss of electroactive material from the electrode, usually this system evolve with time, according to the chemical reactions taking place at those surface sites that have not been adequately protected from the formation of silica by the presence of the attached organic molecules.

The described positive electrochemical response of these prototype devices pushed the surface and interface characterization towards a complete explanation of the basic phenomena involved in chemical bonds formation and structures more than in the modification of the substrate electrical properties.

1.4. Scanning Probe Microscopy

1.4.1. STM. The development of scanning tunneling microscopy (STM) by Binnig et al (1982 [**22**],[**23**]) has provided an atomically resolved microscopic view of clean and adsorbate covered semiconductor surfaces. The experimental technique which has been described in numerous publications (see, for example, Güntherodt and Wiesendanger 1992) is conceptually simple: a sharp metal tip is brought into close proximity (typically 1 nm) of a sample surface. If a voltage U is applied between tip and an electrically conducting sample (the so-called sample bias voltage) a tunneling current I is generated which may be used for regulating the sample tip distance to a constant value. Under the conditions of a constant tunneling current the sample is scanned and an image may be constructed which contains both information on the structural and local electronic properties of the surface. The first

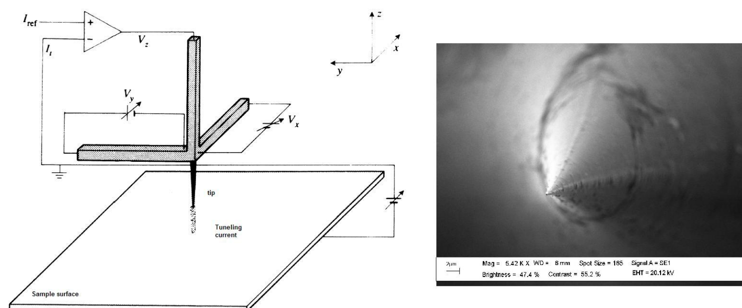

FIGURE 1.4. Setup scheme for an STM (left) and a typical W tip view by electron microscopy (right).

application of STM to a semiconductor surface has also been reported by Binnig et al (1983 [**24**]). They were able to resolve the adatom structure of the 7×7 reconstruction of Si(111) which certainly contributed to the breakthrough of STM in surface physics. In the early STM studies the atomic structure of clean semiconductor surfaces was one of the main aims of experiments. Since, at first approximation, the local electronic states at the Fermi level E_F (Tersoff and Hamann 1985 [**25**]) determine the tunneling current, STM can also be used for a local spectroscopy of

electronic states. This means that STM images always contain the combined influences of both structural and electronic properties which have to be unraveled to gain information on atomic models of surfaces. Measurements on semiconductors have always been used to demonstrate these relations and to develop techniques for improved experiments and data analysis. One reason for the adequacy of semiconductor samples in this respect is that they can be prepared in the form of very clean and well-ordered single-crystal surfaces and that in some cases the large lateral separation of surface atoms (approximately 0.7 nm for 7x7 reconstructed Si(111)) are ideally suited for atomically resolved measurements. On the other hand, electrons on metallic surfaces are delocalized.and not resolved by STM measurements.

1.4.1.1. *Theory.* Tunneling through a potential barrier had already been treated before development of STM, e.g., to explain field emission (Müller 1956) or characteristics of electrical current through a metal-insulator-metal (MIM) structure (Simmons 1963). The measured quantity in most cases is the local tunneling current I which, at the chosen sample bias voltage U, is regulated to a constant value by a feed-back circuit of the STM. What apparently is needed for the description of STM is an expression for the spatially varying tunneling current between tip and sample surface. Following the work of Bardeen (1960) on the tunneling current through a MIM structure Tersoff and Hamann have given an expression for the tunneling current I in the form of

$$I = \frac{2\pi e}{\hbar} \sum_{\mu}^{\nu} f(E_\mu)[1 - f(E_\nu + eU)]|M_{\mu\nu}|^2 \delta(E_\mu - E_\nu); \tag{1.2}$$

where $f(E)$ is the Fermi function, $M_{\mu\nu}$ the tunneling matrix element between states ψ_μ of the metal probe tip and ψ_ν of the sample surface, E_μ and E_ν the unperturbed states in the absence of tunneling and U the sample bias voltage. The contribution of reverse tunneling has been neglected here. The tunneling matrix element $M_{\mu\nu}$ may be computed by using the quantum mechanical expression for the current between states ψ_μ and ψ_ν independent on the height and form of the potential barrier between sample and tip. For modeling the tunneling tip by a point probe, small sample bias

voltage and low temperature, the equation for the local tunneling current may be reduced to

$$I \propto \sum_{\nu} |\psi(\vec{r_0})|^2 \delta(E_\nu - E_F). \tag{1.3}$$

This expression corresponds to the charge density of states at the Fermi level E_F at the position $\vec{r_0}$ of the point probe. Using a tip with spherical symmetry corresponding to an atomic s wavefunction Tersoff and Hamann estimated the lateral resolution of STM which, under the assumption of a reasonable size of the tip apex, was for reconstructed metal surfaces consistent with experimental data. In the case of measurements of semiconductor surfaces a transfer of semiconductor atoms is not unlikely. Since on normally doped semiconductor surfaces the Fermi energy is located within the bulk band gap, in the absence of metallic surface states, tunneling is only possible from the high-lying valence band states or into the low-lying conduction band states. Experience has shown that for measurements on semiconductor surfaces stable tunneling conditions are more easily achieved if a sample bias voltage of about 2 V is used. This means that tunneling is accomplished by electronic transitions from a range of energy levels of the substrate and the tip and the tunneling current can no longer be proportional to the density of states at a certain energy level (e.g., E_F for a metallic surface). In a golden-rule formulation of the tunneling current one has to integrate the contributions corresponding to transitions from or into the energy levels of the sample (depending on the polarity of the sample bias voltage) which have to be weighted by an appropriate tunneling probability. According to the planar electrode model the tunneling probability is proportional to $e^{constUd/\phi^{1/2}}$. This means that the tunneling current from a certain occupied state of the semiconductor into an empty state of the tip will increase exponentially with the sample bias voltage. Therefore a simple relation between the tunneling current and the spatial distribution of the charge density of the sample does not exist. Another effect which might complicate the analysis of tunneling current from a semiconductor surface in terms of local density of states is a possible

voltage drop by the spreading resistance in the semiconductor sample (Flores and García 1984). For low-conductivity samples ($\rho = 100\Omega cm$) and a tunneling current of 5 nA the voltage drop may be larger than 2 V. While the Tersoff and Hamann model has found wide acceptance in the literature other theoretical work has also to be mentioned which contributed to our understanding of the STM results.

The influence of an adsorbed atom on the local tunneling current was computed by Lang (1985 [**26**]) for the first time. He used a two-electrode model where the tip was represented by a single W atom on a metal half space opposite to the adsorbed species on a second half space. The importance of this work was the demonstration that an adsorbed species may be visible either in the form of a protrusion or as a depression depending on the electronic states of the adsorbate. In the case of an adsorbate/semiconductor system, changes of local electronic structure at adsorbate site and its neighborhood always lead to a contrast in the STM images which is not known *a priori* and may give rise to difficulties in the interpretation as will be shown later. The Tersoff and Hamann picture provides a simple interpretation of the STM results. However, since the influence of the tunneling barrier, the structural and electronic properties of the tip and its interaction with the sample surface are not included in this model, more exact theoretical formulations of the STM problem have been developed. The role of the tunneling barrier has been exploited by Lucas et al [**27**](1988) by using a scattering theoretical approach. In principle effects of band structure and the actual corrugation of the surface can be treated. A non-perturbative theory of STM by using a Greens-function formalism has been presented by Noguera (1990) [**28**]. It was the purpose of the latter work to show to what extent the perturbative approaches such as that by Tersoff and Hamann may describe the tunneling current. According to Noguera's work a simple proportionality between the local density of states and the tunneling current does not exist. In particular, in a one-dimensional theory, the tunneling current was found to be independent on potential outside the sample, i.e., on the potential barrier between

sample and tip. This means at the same time that the current does not contain contributions from surface states. This is qualitatively clear, since in a one-dimensional system surface states cannot carry momentum perpendicular to the surface. The results are different in a three-dimensional system, where propagating surface states parallel to the surface may exist. It is still unclear at present how these states couple to the bulk states if they are located in a band gap. Such a case will later be discussed for Si(111)7 $\times$ 7, where stable tunneling conditions may be achieved by using the characteristic metallic-like surface states which lie well within the band gap.

1.5. X-ray Photoemission Spectroscopy

1.5.1. Introduction. In photoelectron spectroscopy, photons (typically from the visible to the X-ray region) act as the probe, while electrons coming out from the matter constitute the analyzed particles. Such a spectroscopy allows investigation of the occupied electronic states, it gives information on the dielectric (insulator, semiconductor or metal) and chemical state.

Photoelectron spectroscopy has become one of the main techniques for studying solid surfaces, low-dimensional systems, interfaces between different materials, chemisorption of gases at surfaces, surface and interface chemical interactions, correlation effects. This is due to the high surface sensitivity attainable with an appropriate choice of the experimental parameters, and to the direct measurability of the electronic states. Moreover, synchrotron radiation widens the investigation field, thanks to the availability of the widest photon energy range with different excitation cross section, and to the variety of methodologies of data collection, using parallel modification of photon energy and electron kinetic energy analysis.

1.5.2. Historical introduction. The Einstein's explanation in 1905 of the photoelectric effect as a quantum effect, thus impossible to be interpreted within the classical electrodynamics theory, follows a series of various experimental observations. The first experimental evidence ascribable to the photoelectric effect is

the increase of electric discharge yield between two electrodes, when the cathode is illuminated by ultraviolet (UV) light. This experiment was performed by Hertz in 1887 [**29**].

The experimental and theoretical work proceeded on the mainstream of determining the metal work function, despite the bad vacuum conditions and consequent experimental problems connected with surface cleanness (as it was realized later on). Among the large variety of works on this subject, we would quote the small escape depth determination for the photoemitted electrons, with the consequent surface sensitivity achieved by the technique [**30**], the test of the Sommerfeld's theory of metals [**31**], the Fowler's theory to determine , the alkali metal-induced lowering of the work function ϕ [**61**], and the Bardeen's theories during the 30's [**33**]. Finally, starting from the 60's, photoelectron spectroscopy has been extensively used as experimental technique for the solid state electronic structure [**34**]. In parallel with the theoretical investigations, it became the most important tool for the electronic band structure determination in solids. This development was possible also thanks to the improvement of the ultra-high-vacuum (UHV) techniques (pressures lower than 10^{10} mbar), and thanks to the availability of high intensity UV radiation sources. In the same period, there was also development of the X-ray photoelectron spectroscopy (XPS), or Electron Spectroscopy for Chemical Analysis (ESCA), thanks to Siegbahn's work [**35**]. The XPS approach to photoemission is particularly sensitive to the chemical state of atoms, molecules and solids, by studying the atomic species core levels. Eventually, starting from the 70's, there is rapid development of the synchrotron radiation (SR) sources, producing an almost continuous electromagnetic spectrum from the infrared to the hard X-rays region (which energy range obviously depends on the particular accelerator machine).

1.5.3. Elements of photoemission theory.

1.5.3.1. *The photoelectron current.* In the photoemission process, the sample is left in an ionized state when the electron is emitted. Both the sample (atom, molecule or solid) and the emitted electron can be viewed as an excited state, differing from the fundamental state by the incident photon energy. This rigorous picture can be often simplified in a single-particle picture, where the photoemitted electron maintains its energy while leaving the sample, so that its energy can be written as the photon energy subtracted by the binding energy of the original occupied orbital. In such a description, the analysis of the photoemitted electron distribution gives information on the energy and density of states of the corresponding occupied one-electron levels. The photoemitted electron current J, as measured by an ideal spectrometer resolving energy, angle, and photon and electron polarization states, is a function of 10 variables, as shown in fig. 1.5:

$$J = f(h\nu, \vec{\epsilon}, \theta, \Phi; E_e, \vec{\sigma}, \theta_e, \Phi_e) \tag{1.4}$$

where $h\nu$, $\vec{\epsilon}$, θ and Φ are energy, polarization direction and polar and azimuthal angle of the incident photon, while E_e, $\vec{\sigma}$, θ_e and Φ_e are energy, spin polarization, polar and azimuthal angle of the emitted electron. In a typical experiment, only a few of these parameters are varied, while the others are kept constant or integrated.

For example, in the Energy Distribution Curve (EDC) method, the current J is measured as a function of the photoelectron energy E_e, while keeping the other variables fixed. In the angular resolved mode, the θ_e and Φ_e angles are resolved, otherwise the technique is angular integrated. In the Constant Initial State (CIS) mode, $h\nu$ and E_e are varied while keeping constant their energy difference, and in the constant Final State (CFS) mode $h\nu$ is varied and electrons are analyzed at constant E_e. Moreover, if it is possible to analyze the photoelectron spin state $\vec{\sigma}$, the technique gives information on the magnetic state of the analyzed system. Before entering into the details of the general theoretical aspects of photoemission, it's worth noting the

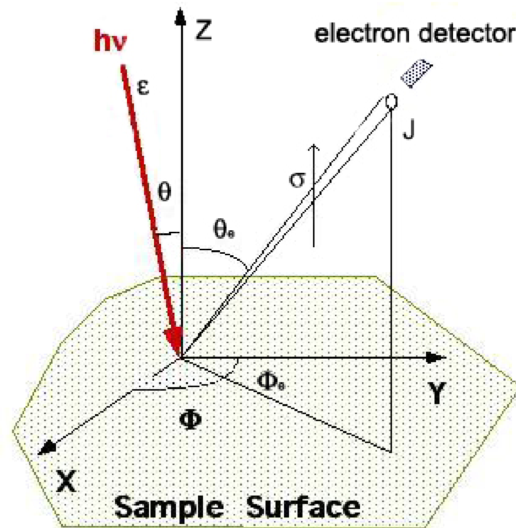

FIGURE 1.5. Schematic diagram of the photocurrent J and related parameters.

high surface sensitivity of this technique. In fact, while photons typically penetrate the solid for hundreds of Å(tens of nm), obviously depending on the material type and photon wavelength, the typical energy of the photoemitted electrons lies in the 5-1500 eV energy range, with penetration length λ in the range between a few Åto a few tens of Å. Such a penetration length corresponds to the escape depth for the photoemitted electrons escaping in vacuum. It can be phenomenologically described as an exponential attenuation behavior as a function of the penetration region. The λ value is limited by the electron-electron scattering, the excitation of collective modes (plasmons), and by recombination processes (Auger), while the electrons escape into vacuum from the solid. Thus, a fraction of photoelectrons (primary electrons) escapes into vacuum without suffering scattering and energy losses, while a large part of photoexcited electrons (secondary electrons) scatter and suffer various energy losses. The escape depth as a function of the electron kinetic energy follows a general behavior, with a minimum value (thus a maximum surface sensitivity) roughly between 70 and 100 eV. There are analytical functions derived for the different materials as shown in fig. 1.6.

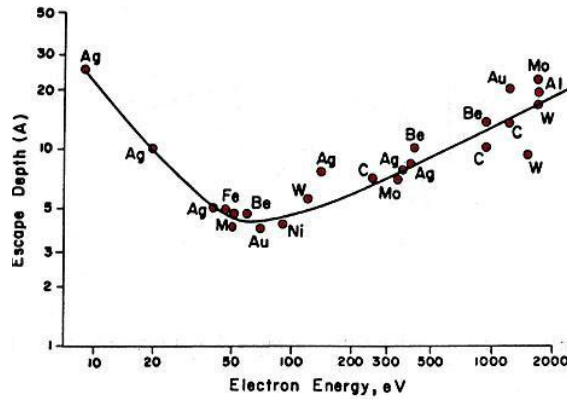

FIGURE 1.6. Electron mean-free-path in a solid, as a function of energy [**36**].

1.5.3.2. *General theoretical aspects.* The photoelectric process can be described as the transition of one electron from an initial occupied state to a final empty free-electron level in vacuum. In the case of an atom, the final state corresponds to the final state of an optical excitation, in a solid this is not necessarily the case. In fact, the optically excited electron must travel towards the surface, come through it, and escape into vacuum as a photoelectron. We can synthesize the two processes, optical absorption and photoemission, in the diagrams plotted in fig. 1.7 where an atom, initially in the $|i\rangle$ state, absorbs one photon with wavevector k_L, and polarization $\vec{\epsilon}$, at the time t, reaching the excited final state $|f\rangle$. If the photon energy is high enough a photoelectron with wavevector k_e and spin polarization σ can be created, i.e. an electron with free empty state in vacuum. Within this description the two processes, optical absorption and photoemission, are similar, apart from the generation of an electron in the second case.

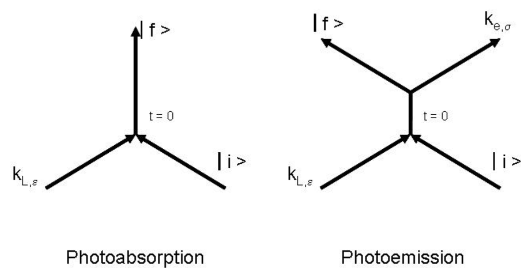

FIGURE 1.7. Schematic representation of the photoabsorption and photoemission processes

We can describe the N electrons initial state $|i\rangle$ as a stationary state, thus as a solution of the Schrödinger equation:

$$\mathcal{H}_0|i\rangle = E_0|i\rangle \tag{1.5}$$

with the hamiltonian $\mathcal{H}$ constituted by four terms, kinetic, electron-nucleus interaction, electron-electron, and spin-orbit interaction. Only the spin-orbit term mixes spatial and spin coordinates. All operators are single particle operators, with the exception of the electron-electron interaction, a two-particles operator:

$$\mathcal{H}_0 = \sum_{i=1}^{N} \frac{p_i^2}{2m} + \sum_{i=1}^{N} \frac{-Ze^2}{r_i} + \sum_{i,j}^{N} \frac{1}{2} \frac{e^2}{r_{ij}} + \sum_{i=1}^{N} \zeta(r_i)\vec{l}_i \cdot \vec{s}_i. \tag{1.6}$$

The relation between the final and the initial state is the principal information that a theoretical model has to explain since, from an experimental point of view, the final state is object of measurement and the initial state is object of study.

By means of the time-dependent perturbation theory is possible to calculate the transition probability W_{fi} from the unperturbed state $|i\rangle$ at energy E_i to a state $|f\rangle$ at energy E_f:

$$W_{fi} = \frac{2\pi}{\hbar^2}|\langle f|H_i|i\rangle|^2\delta(E_f - E_i - h\nu) \tag{1.7}$$

Of course the key term in this expression is the interaction hamiltonian H_i which define the excitation matrix element; by assuming that the dielectric properties remain constant it can be expressed as:

$$\mathscr{M}_{fi} \propto \frac{e}{c}\langle f|(\vec{A} \cdot \vec{p} + \vec{p} \cdot \vec{A})|i\rangle \tag{1.8}$$

This therm is directly present in the mathematical expression of the photoemission current J:

$$J(E, h\nu) \propto \sum_{i,f} \int |\mathscr{M}_{fi}|^2\delta(E_f(\vec{k}) - E_i(\vec{k}) - h\nu)\delta(E_f(\vec{k}) - E)d\vec{k}. \tag{1.9}$$

In this equation is included all the physical information of photoemission process, since the sum and integral operators take into account all the possible excitations

from the occupied states or bands $E_i(\vec{k})$, to the empty states or bands $E_f(\vec{k})$, keeping the momentum conservation (direct transitions). The first δ function represents the energy conservation in the photoelectric process, while the second one selects from all the possible optical transitions only those which final energy E_f is equal to the energy E of the analyzer.

1.5.3.3. *Beyond the three steps model.* Of course the photoelectron current density expressed in eq. 1.9 is not exactly the measured quantity in a photoemission experiment. The Energy Distribution Curve (EDC) corresponds to the photoemitted electron current $I(E, h\nu)$, sum of a primary electrons distribution current I_p and of a secondary electron current I_s, due to inelastic scattering processes accompanied by energy loss processes:

$$I(E, h\nu) = I_p(E, h\nu) + I_s(E, h\nu) \tag{1.10}$$

Although it is unstructured, the secondary electron current I_s appearing almost as a continuum background at low kinetic energies (about 0-10 eV) due to the multiple energy losses, it can present some significant feature overlapped to the background, due to energy loss peaks caused by plasmon excitations (collective excitations of electron-gas). The distribution of primary electrons in the framework of the so called "three steps model" can be factorized in three terms, each associated to a step of the process: J to the optical transition (eq. 1.9), T to the propagation through the solid, and D to the escape into vacuum:

$$I_p(E, h\nu) = J(E, h\nu) \times T(E_f, h\nu) \times D(E_f). \tag{1.11}$$

Although it is widely accepted since it was proposed by Berglund and Spicer [**34**] it's validity is limited to systems where the *volume effect* is dominant to the *surface effect*(see for a detailed discussion ref. [**37**]). This model works well when it is possible to separate the three contribution to the primary current but it is limiting the analysis when the photoemission signal itself (J) is affected by changes in the propagation (T) and escape (D) terms. These changes are possible for systems

like those treated in this work: adsorbate induced electronic states on semiconductor surfaces make the surface effect dominant or concurrent with the volume one, breaking the first assumptions of the three steps model.

However, fine modifications of the photoelectron signal due to surface effect are more evident in low temperature conditions, in the valence band regions of the spectra and/or in high energy-resolved experiments. In our case the experiments has been made at RT, on core level peaks and carried out with a non monochromatic X-ray source with an analyzer resolution of 0.8 eV. Thus the instrumental broadening of the XPS signal doesn't allow speculations about fine effects.

1.5.4. Core level photoemission. The binding energy of a core level is defined as $E = h\nu - E_k$ (where $h\nu$ is the energy of the impinging monochromatic photons; E_k is the kinetic energy as measured relative to the material Fermi energy). The binding energy values are, within few percent, a unique characteristic of each core level line of a particular atomic species in whatever form or alloy it is analyzed. The knowledge of such values has been the first result of core level photoemission, since it is cleat that it is possible by means of these technique (known also as ESCA) to identify unknown atoms present on the analyzed surface. A more careful analysis of a core level line shape in addition to the knowledge of the binding energy of the peak center, give an extremely powerful tool to study matter. On top of this preliminary chemical analysis it is possible to obtain far richer information analyzing in details the peak structure and not only its energy position. We will see that each single core level line it is formed by more lines centered at slightly different energies and with characteristic shape and intensities.

1.5.4.1. *Core level binding energy: initial and final state effects.* Formally the core level binding energy measured in photoemission is defined as the energy difference between the total energy of the final state photoemitted electron plus a core hole in a solid with N-l electrons and the unperturbed N-electron state (Koopmans'

theorem [**38**]):

$$E_B = E_T(N-1) - E_T(N). \quad (1.12)$$

What we analyze are the small shifts from core levels of the same atomic species but in different chemical, geometrical and electronic configurations. Let us define ΔE_B as the difference between the measured electron binding energy and its energy in the ground state. ΔE_B will be essentially the sum of two contribution: the first takes into account differences in the ground state $E_T(N)$, the second is induced by the presence in the final state of a core-hole. We can than write:

$$\Delta E_B = \Delta E_{initial} + \Delta E_{final} \quad (1.13)$$

and analyze the two contribution separately.

The initial state contribution $\Delta E_{initial}$ reflects the electrostatic potential changes in the core level region, occurring when the atom from which the core level photoelectron is extracted changes its electronic structure and chemical environment, and can be schematized as the sum of different terms:

$$\Delta E_{initial} = \Delta E_{conf} + \Delta E_{charge} + \Delta E_{Madelung} \quad (1.14)$$

where: ΔE_{conf} represents binding energy variation of a core level induced by the variation in configuration of the emitting atom. Such differences clearly influence the valence electronic charge distribution and its Coulomb interaction with the deeper lying core level electrons, hence affecting their energy position. ΔE_{charge} represents the variation of the valence electronic charge around an atom, when this atom participates to a directional chemical bond. This is a very important contribution in the chemical shifts observed on semiconductors reconstructed surfaces or during the formation of metal semiconductor interfaces, when, either the atomic rearrangement or a chemical bond between substrate and metallic ad-atom, causes a charge transfer. The term $\Delta E_{Madelung}$ keeps track of the effects on the core level binding energies as induced by changes of lattice atoms close to the photo-emitter. This effect is particularly strong in ionic solids. Such effect, calculated as a Madelung summation over

lattice atomic sites, tends to partially compensate the core level shifts as calculated by considering only intra-atomic terms.

With a strong approximation one can neglect the term $\Delta Efinal$ if one considers the N-l electrons completely independent to the core hole left by the photo-emitted electron. This approximation is the basic concept behind the Koopman theorem, which defines the binding energy of a photo-emitted electron as the orbital energy of photo-emitted electron. So that ΔE_{final} bring information of binding energy variation by core induced relaxation. Schematically we can write:

$$\Delta E_{final} = \Delta E_{relax} = \Delta E_{intra} + \Delta E_{extra} \tag{1.15}$$

ΔE_{intra} considers the effect of intra-atomic relaxation. The photoemission process, in fact, induces big changes in the electronic configuration of isolated atom. The external orbitals will relax as a consequence of nucleus higher effective charge acting in presence of a deeper lying core. For this reason the measured energies results several eV smaller than that of the isolated and unperturbed atom. It is worth noting that such relaxation not always results in the fundamental state of the atom-core hole ("Shake up" satellites).

ΔE_{extra} term takes into account the changes induced by the charge redistribution occurring to screen the core-hole left on the excited atom. It is important to notice that such binding energies variations are strongly affected the detailed chemistry of the material, like its ionic character, the screening etc. For instance such shifts will depends on the angular momentum of the electrons screening the core hole (bigger for s or p, rather than the more localized d electrons). A typical example of final state effect is the observed asymmetry in core level photoemission from a metal. Such asymmetric core level line shape is named Doniach-Sunjic and shows itself in the increasing of the photoemission signal towards lower kinetic energies. A photo-emitted electron can transfer part of its energy to electrons at the Fermi energy. This distorted line-shape is clearly only present in metallic systems.

1.5.4.2. *Core level line width.* The width of a core level spectrum is the convolution of different contributions. One is the Gaussian broadening due to the finite resolution of the experimental set-up. Such Gaussian broadening is the convolution between the resolution of the electron energy analyzer and of the X-ray source, that in a well designed experiment should be similar (see par. 2.2.4).

A very important contribution to the total core level width is the one associated with the electron-phonon interaction, which depends on their coupling strength in the material under analysis and is also assumed to be Gaussian. The Franck-Condon principle shows how the lattice vibrations occurring at finite temperature can be observed in the core level width. Small variations around the atom equilibrium position strongly affect the transition energy (initial state-final state) in the photoemission process due to the different number of phonons excited in the final state. At room temperature the phonon broadening can be quite big (comparable or even bigger than the one induced by the experimental resolution), but one can reduce it lowering the experiment temperature. A third contribution to the total core level line width is that caused by the finite lifetime of a core-hole. Heisenberg uncertainty principle states that the less is the decay time of a core hole the bigger is the uncertainty on its energy hence its core level width. Such life-time broadening has a Lorentian shape of the kind:

$$I(E) = I(E_0)\frac{\Gamma_L}{(E - E_0)^2 + \Gamma_L^2} \tag{1.16}$$

where $I(E)$ is the signal intensity at the energy E; E_0 is the energy of the peak maximum; Γ_L is the full width at half maximum (FWHM) related to the broadening induced by the core-hole decay time. It can be written as:

$$\Gamma_L = FWHM = h/\tau = 6.58 \cdot 10^{-16}/\tau eV \tag{1.17}$$

where τ is the core-hole life time and Γ_L can assume values between 0.1 and 100 eV.

Let us see in more details how a core-hole decays: this occurs via two channels (a scheme is proposed in fig. 1.8). One channel involve the replacement of the photo-emitted electron by transferring an electron lying in an higher energy state

into the core hole with a consequent emission of a photon (fluorescence). The other channel involves two outer-shell electrons, one filling the deeper-lying core-hole, the other being emitted with the right kinetic energy balance energy conservation (Auger process). The final state of an Auger process consist of two holes and is named according to the following rules: first one mention the initial state orbitai (K if the exited electron Comes from a $1s$; L_1 if it comes from a $2s$ level; L_2 from $2p_{1/2}$; L_3 from $2p_{3/2}$; M_1 from $3s$ etc.) followed by the name of the orbitals with the holes in the final state. One can easily see that the decay time of a core-hole decrease with the atomic number Z to the bigger orbital contraction in the high Z atoms. Also, the relative weight of the two decay channels (fluorescence or Auger) varies with atomic number: florescence yield varies as Z^4 while the Auger decay as Z^2. If one of the final state core-hole the same quantum number of the excited electron (eg. L_1L_2M process), is called Coster-Kronig transition. If both final state core-holes have the same quantum number of the exited electron (eg. $L_1L_2L_3$ process), this is called Super-Coster-Kronig transition. The presence of different Auger transitions available, clearly increases the Auger decay speed, causing an increase in the photoemission core level line shape. From this simple analysis it results that, to be able to single out chemical shift as small as possible, one should study as sharp as possible core level lines. For this reasons the most studied levels are the shallow one with a high angular momentum to reduce the role played by Coster-Kronig and Super-Coster-Kronig transition. The broadening of a core level is also induced by structural disorder or surfaces inhomogeneities, contributions that are very difficult to predict and analyze. Such spurious contributions can mask the interpretation of core level line width only in terms of experimental, phonon, and life-time induced effects.

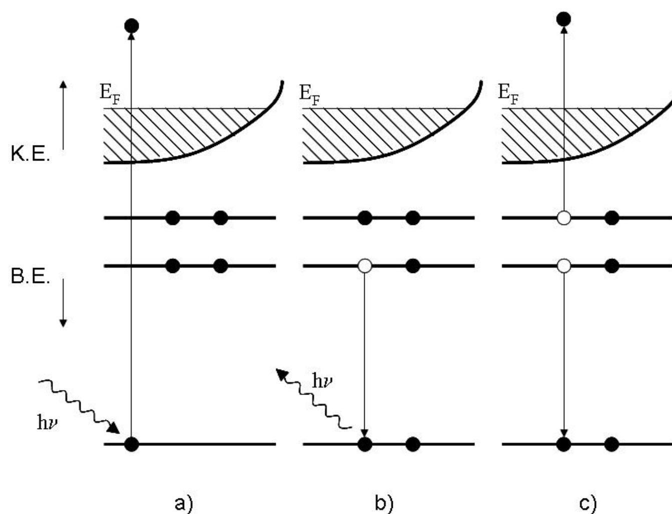

FIGURE 1.8. Schematic diagram of: a) photoemission process from a core level; b) core-hole decay by emission of a photon; e) Auger core-hole decay.

1.6. Spectromicroscopy

Molecule modified surfaces can present locally ordered structures. A chemical contrast experimental technique is crucial for the chemical/morphological characterization of such surfaces only locally homogeneous. This technique is Photoemission Electron Microscopy (PEEM).

1.6.1. Types of Contrast. Photoemission of an electron can be explained in terms of a simple model which assumes three steps:

(1) excitation of a photoelectron by the incident light,
(2) transport of this electron to the surface, and
(3) penetration of the electron through the surface into vacuum.

1.6.1.1. *Workfunction Contrast.* The third step is of major importance for PEEM using UV light (briefly called UV-PEEM). It is governed by the work function O, which can be viewed as a potential barrier with a field oriented perpendicular to the surface. Photoelectrons need to have a sufficiently high kinetic energy in order to overcome this barrier and eventually be emitted from the surface. The light source to be used for UV-PEEM should provide a pronounced intensity maximum at energies $h\nu$ in the range between the lowest and the highest work functions of the

surface to be imaged. This way maximum contrast is achievable, because surface areas exhibiting a high work function will have a very low photoelectron yield and thus appear dark in the PEEM image, whereas low work function areas will appear bright (see Fig. 1.9 , taken using the Hg source). Values found for the work function of metals range from less than 2 eV to 6 eV; a typical value for transition metals is 5 eV. Consequently suitable light sources are the Hg UV lamp exhibiting an intensity maximum around $h\nu = 4.9eV$, or a Deuterium discharge lamp with a broad maximum between $h\nu = 5.2eV - 6.2eV$. The most suitable excitation spectrum can be taylored via the appropriate choice of the excitation source in combination with the transmission cutoff of the entrance window. Other excitation sources of higher energy, such as a H-Lyman α-source ($h\nu = 10.2eV$) are suited for large gap insulators (like diamond) but the workfunction contrast is not pronounced.

1.6.1.2. *Topographic Contrast.* This type of contrast is always present if 3D structures on a surface are imaged. The mechanism is comparable to the effect of the direction of illumination in a scanning electron microscope (SEM) image. Since the exciting photon beam is impinging at a relatively small angle with respect to the surface (typically 20-30 degrees), a shadowing effect occurs which gives rise to a pronounced contrast. The regions of the structures which are oriented towards the direction of photon illumination will appear brighter, whereas regions away from the photon beam will exhibit dark shadows. The widths of these shadow regions are a measure of the height of the imaged structures. Note in addition that areas parallel to the surface will generally appear brighter than those being strongly tilted or even perpendicular to the surface, because the contrast aperture will discriminate against large takeoff angles thus giving rise to orientational contrast (cf. Fig. 1.5). The contributions of sample illumination and orientational contrast resulting from the contrast aperture are always simultaneously present.

1.6.1.3. *Chemical Contrast at Higher Photon Energies (Element-Specific Imaging).* Higher excitation energies are extremely useful in element-specific imaging using tuneable Synchrotron radiation. In this mode of operation the characteristic

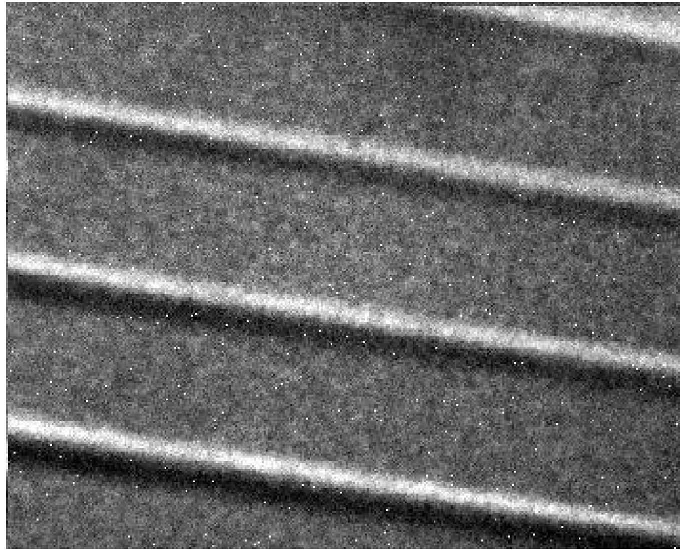

FIGURE 1.9. PEEM image $40 \times 30\ \mu m^2$ on a test sample of Pd stripes on Si. The light source used was a Deuterium discharge lamp.

structure of an X-ray absorption (XAS) spectrum is utilized for imaging. When the photon energy is tuned to the maximum of an absorption edge of a certain element, this element will appear bright ('light up') in the image. Thus it's lateral distribution becomes visible on the screen. The 'background' of electron emission (corresponding to all lower-lying photo-absorption edges) can easily be eliminated by taking a second image at a photon energy below the edge and by digital subtraction of the second from the first. The integral sample stage PEEM (IS-PEEM) ensures that no sample drift or vibration will influence this digital subtraction method. The resulting difference image directly shows the distribution of the selected element. At the maximum of the absorption edge the kinetic energy of the corresponding photoelectrons is small, thus the electron optics is adjusted to the low-energy maximum of the energy distribution. Note that direct transitions from all higher-lying core levels of all elements present on the sample will lead to electron signals with higher kinetic energies. These electrons may cause a diffuse (non-focused) background in all single images. It should, however, cancel in the difference image. At high photon energies (much larger than the workfunction ϕ) it must be taken into account that

a wide electron kinetic-energy distribution will generally tend to diminish the maximum achievable spatial resolution. In practice, a well defined electrostatic field is applied between the sample and the outermost surface of the objective, and hence the sample is an integral part of the electrostatic lens system of the PEEM. The strength and shape of this field is critical for the resolution. In the ideal case all photoelectrons should start with zero kinetic energy when penetrating through the surface; then the electrons will be accelerated towards the objective by means of the applied field. Excess excitation energy, however, which exceeds the value necessary for electrons to just leave the surface, will be converted into electron kinetic energy. The amount and direction of the corresponding electron momentum will alter the electron trajectories and influence the focusing properties of the objective (chromatic aberration).

1.7. Mercury-drop electrode and IPE

In a recent communication [**17**], it has been reported that an alkyl monolayer can tune a resistor (a direct mercury-silicon contact) to a diode-like behavior (a mercury/molecule/silicon junction). It was also described how the electron transport correlates to the device performance in these metal/molecule/semiconductor junctions . These preliminary studies explored the use of organic monolayers on oxide-free silicon to change the interfacial nature of metal/semiconductor junctions, that is, effectively passivating the silicon surfaces and molecularly tuning the effective barrier heights of these diode junctions. Mercury contact on functionalized surfaces is a novel technique which is promising to extract information on the electrical properties of that type of interface. Specifically the alkyl chains molecules were not suitable to give a response to cyclic voltammetry like ferrocenes (see par. 1.3.1) which are redox species; in fact, to understand the electrical properties of those layers and their modifications of the Si surface, mercury drop contact experiments has been carried out. Information about resistive or rectifing character of

the created junctions and physical quantities like barrier height and contact resistance are possible to investigate with this technique. Moreover we present a system to perform Internal Photoemission (IPE) measurements on these kind of junctions; independent measurements of junction barrier height by IPE experiments allow to explain the behavior of the hybrid interface in parallel with I-V characteristics. In the following sections it is reported a brief discussion about the theoretical models used to interpret the data and the description of the home made experimental setup.

1.7.1. Metal-Semiconductor Contacts. Metal-semiconductor contacts are an obvious component of any semiconductor device. At the same time, such contacts cannot be assumed to be as low resistance as that of two connected metals. In particular, a large mismatch between the Fermi energy of the metal and semiconductor can result is a high-resistance rectifying contact. A proper choice of materials can provide a low resistance ohmic contact. However for a lot of semiconductors there is no appropriate metal available. Instead one then creates a tunnel contact. Such contact consists of a thin barrier obtained by heavily-doping the semiconductor through which carriers can readily tunnel. Contact formation is also affected by thin interfacial layers and is typically finished off with a final anneal or alloy formation after the initial deposition of the metal.

1.7.2. Ohmic contacts. A metal-semiconductor junction results in an ohmic contact (i.e. a contact with voltage independent resistance) if the Schottky barrier is zero or negative. In such case, the carriers are "free" to flow in or out of the semiconductor so that there is only a minimal resistance across the contact more than the intrinsically present contact resistent. For an n-type semiconductor, this means that the workfunction of the metal must be close to or smaller than the electron affinity of the semiconductor. For a p-type semiconductor, it requires that the workfunction of the metal must be close to or larger than the sum of the electron affinity and the bandgap energy.

1.7.3. Tunnel contacts. An alternate and more practical contact is a tunnel contact. Such contacts do have a positive barrier at the metal-semiconductor interface, but also have a high enough doping in the semiconductor that there is only a thin potential barrier separating the metal from the semiconductor. If the width of the depletion region at the metal-semiconductor interface is very thin, on the order of 3 nm or less, carriers can readily tunnel across such barrier. The required doping density for such contact is 10^{19} cm^{-3} or higher.

1.7.4. I-V characteristics.

1.7.4.1. *Schottky diode current.* The current across a metal-semiconductor junction is mainly due to majority carriers. Three distinctly different mechanisms exist: diffusion of carriers from the semiconductor into the metal, thermionic emission of carriers across the Schottky barrier and quantum-mechanical tunneling through the barrier. The diffusion theory assumes that the driving force is distributed over the length of the depletion layer. The thermionic emission theory on the other hand postulates that only energetic carriers, those, which have an energy equal to or larger than the conduction band energy at the metal-semiconductor interface, contribute to the current flow. Quantum-mechanical tunneling through the barrier takes into account the wave-nature of the electrons, allowing them to penetrate through thin barriers. In a given junction, a combination of all three mechanisms could exist. However, typically one finds that only one limits the current, making it the dominant current mechanism.

The analysis displays that the diffusion and thermionic emission currents can be written in the following form [**60**]:

$$J_n = qvN_c e^{(-\frac{\phi_B}{V_t})}(e^{\frac{V_a}{V_t}} - 1) \tag{1.18}$$

This expression states that the current is the product of the electronic charge, q, a velocity, v, and the density of available carriers in the semiconductor located next to the interface. The velocity equals the mobility multiplied with the field at the interface for the diffusion current and the Richardson velocity (see section 1.7.4.3)

for the thermionic emission current. The minus one term ensures that the current is zero if no voltage is applied as in thermal equilibrium any motion of carriers is balanced by a motion of carriers in the opposite direction.

The tunneling current is of a similar form, namely:

$$J_n = qv_R n\Theta \tag{1.19}$$

where v_R is the Richardson velocity and n is the density of carriers in the semiconductor. The tunneling probability term, Θ, is added since the total current depends on the carrier flux arriving at the tunnel barrier multiplied with the probability, Θ, that they tunnel through the barrier.

1.7.4.2. *Diffusion current.* This analysis assumes that the depletion layer is large compared to the mean free path, so that the concepts of drift and diffusion are valid. The resulting current density equals [**60**]:

$$J_n = \frac{q^2 D_n N_c}{V_t}\sqrt{\frac{2q(\phi_i - V_a)N_d}{\varepsilon_s}}e^{(-\frac{\phi_B}{V_t})}(e^{\frac{V_a}{V_t}} - 1) \tag{1.20}$$

The current therefore depends exponentially on the applied voltage, V_a, and the barrier height, ϕ_B. The prefactor can more easily be understood if one rewrites it as a function of the electric field at the metal-semiconductor interface, ε_{max}:

$$\varepsilon_{max} = \sqrt{\frac{2q(\phi_i - V_a)N_d}{\varepsilon_s}} \tag{1.21}$$

yielding:

$$J_n = q\mu_n \varepsilon_{max} N_c e^{(-\frac{\phi_B}{V_t})}(e^{\frac{V_a}{V_t}} - 1) \tag{1.22}$$

so that the prefactor equals the drift current at the metal-semiconductor interface, which, for zero applied voltage, balances exactly the diffusion current.

1.7.4.3. *Thermionic emission.* The thermionic emission theory assumes that electrons, which have an energy larger than the top of the barrier, will cross the barrier provided they move towards the barrier. The actual shape of the barrier is hereby ignored. The current can be expressed as [**60**]:

$$J_{MS} = A^{*}T^{2}e^{(-\frac{\phi_B}{V_t})}(e^{\frac{V_a}{V_t}} - 1) \tag{1.23}$$

where $A^{*} = \frac{4\pi q m^{ast} k^2}{h^3}$ is the Richardson constant and ϕ_B is the Schottky barrier height.

The expression for the current due to thermionic emission can also be written as a function of the average velocity with which the electrons at the interface approach the barrier. This velocity is referred to as the Richardson velocity given by:

$$v_R = \sqrt{\frac{kT}{2\pi m}} \tag{1.24}$$

So that the current density becomes:

$$J_n = q v_R N_c e^{(-\frac{\phi_B}{V_t})}(e^{\frac{V_a}{V_t}} - 1) \tag{1.25}$$

1.7.4.4. *Tunneling.* The tunneling current is obtained from the product of the carrier charge, velocity and density. The velocity equals the Richardson velocity, with which on average the carriers approach the barrier. The carrier density equals the density of available electrons, n, multiplied with the tunneling probability, Θ, yielding eq. 1.19 where the tunneling probability is obtained from [**60**]:

$$\Theta = exp(-\frac{4}{3}\frac{\sqrt{2qm^{*}}}{\hbar}\frac{\phi_b^3/2}{\varepsilon}) \tag{1.26}$$

and the electric field equals $\varepsilon = \phi_B/L$.

1.7.4.5. *Barrier Height, Ideality Factor, and Series Resistance.* The fundamental parameter that describes electrical properties of a metal-semiconductor junction is the barrier height. According to the Mott-Schottky rule [**60**] for an ideal metal-semiconductor (p-type) junction, the barrier height ϕ_b is given by

$$q\phi_B = E_g - q(\phi_m - \chi_{sc}) \tag{1.27}$$

where ϕ_m is the work function of the metal, $q\chi_{sc}$ is the electron affinity, and E_g is the band gap of the semiconductor. In practice, the effective barrier height ϕ_{eff} together with the ideality factor, n (a dimensionless parameter to take into account

nonideal diode behaviors), were often determined from the analysis of the current density-voltage ($J-V$) characteristics using the classical thermionic emission theory

$$J = A^{*}T^{2}e^{(-\frac{q\phi_{eff}}{kT})}(e^{\frac{qV}{nkT}} - 1) \tag{1.28}$$

where V is the applied bias voltage J is the measured current density q is the absolute value of the electronic charge. A^{*} is the Richardson constant with a typical value of 32 $Acm^{-2}K^{-2}$ for p-type silicon. A problem arises if it is necessary to extract reliable values of ϕ_{eff} when the diode has a large series resistance R_s. It includes the metal resistance, ohmic contacts, and spreading resistance in the wafer. Equation 1.28 has been modified in order to model the effect of the series resistance R_s in the diode junctions [?], particularly when the region over which the plot of lnJ versus V is linear is small, and accurate extrapolation to zero voltage may be difficult. In the case of $q(V - JR_s) > kT$ we have,

$$J = A^{*}T^{2}e^{(-\frac{q\phi_{eff}}{kT})}(e^{\frac{qV-JR_s}{nkT}}). \tag{1.29}$$

equation 1.29 can be rewritten as:

$$V = JR_s + n\phi_{eff} + n\frac{kT}{q}ln\left(\frac{J}{A^{*}T^{2}}\right) \tag{1.30}$$

Differentiating eq. 1.30 with respect to J and rearranging terms, we can obtain:

$$\frac{dV}{dlnJ} = n\frac{kT}{q} + JR_s \tag{1.31}$$

From eq. 1.31, a plot of $dV/(dlnJ)$ vs J will give R_s as the slope and nkT/q as the y-axis intercept. To evaluate ϕ_{eff}, we can define a function $H(J)$

$$H(J) = V - n\frac{kT}{q}ln\left(\frac{J}{A^{*}T^{2}}\right). \tag{1.32}$$

From eq. 1.30 , we then have

$$H(J) = JR_s + n\phi_{eff} \tag{1.33}$$

According to eq 1.33, a plot of $H(J)$ vs J will also give a straight line with the y-axis intercept equal to $n\phi_{eff}$, from which ϕ_{eff} can be derived by substituting in

the n value obtained from eq. 1.31. The slope of this plot also provides a second determination of R_s, which can be used to check the consistency of this approach. We have applied the above procedure to examine the J-V characteristics of the passivated mercury-silicon junctions.

1.7.5. IPE experiment. Another powerful instrument to investigate the interface properties of meatal/insulator/semiconductor junctions is the Internal Photo-Emission (IPE). By using photons of energy close to the band gap of the semiconductor, it is possible to have exact information about the interface states which drive the barrier height of the junction.

This technique is implemented by illuminating the junction with monochromatic photons, and measuring the photon generated current flooding through the junction. The thresholds in the photocurrent versus photon energy curves reveal the energy barriers for photoexcitation in the system. Consider such curves for a heterojunction. Each feature corresponds to a given electron excitation process from valence-band or localized states to conduction band or localized gap states.

In fig. 1.10 it is shown, e.g., the band diagram of a metal/n-semiconductor junction with the formation of a barrier ϕ_B at the interface.This band bending is expected if the work function of the metal is bigger than that of the semiconductor. A photon energy scan allows to estimate the value of the barrier height by the raising of the photocurrent signal.

The condition for the electrons to escape through the junction and overcome the barrier is $E > \phi_B$; the ϕ_B value is in general found by the plot of the normalized photon yield versus the photon wavelength λ. According to the Fowler model [**61**], a quadratic slope is expected:

$$Y = N_A d C^* \lambda^2 \tag{1.34}$$

where N_A is the doping concentration, d is the film thickness and C^* is a collection of constants (effective mass, refraction index, speed of light, etc.)

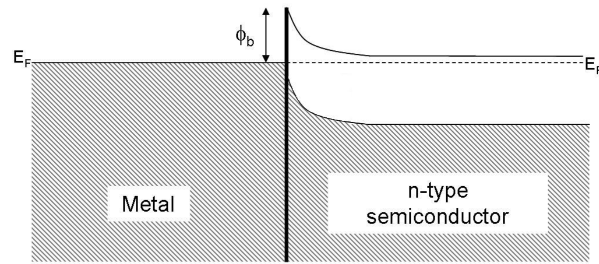

FIGURE 1.10. Band diagram of a typical metal/n-type semiconductor junction with the formation of a Schottky barrier ϕ_b.

CHAPTER 2

Experimental Apparatus and sample preparation

2.1. UHV System: setting up

Surface studies need ultra high vacuum (UHV) environment to avoid contamination. To perform UHV several conditions have to be respected:

- well dimensioned pumping system;
- UHV compatible clean materials and tools;
- outgassing.

As it is shown in the picture of fig. 2.1 our system is composed by different parts: the analysis chamber include XPS components PEEM flange and the SPM microscopes, the preparation chamber where it is possible to perform in-situ treatments, and a small load-lock chamber for fast entry operations. Both analysis and preparation

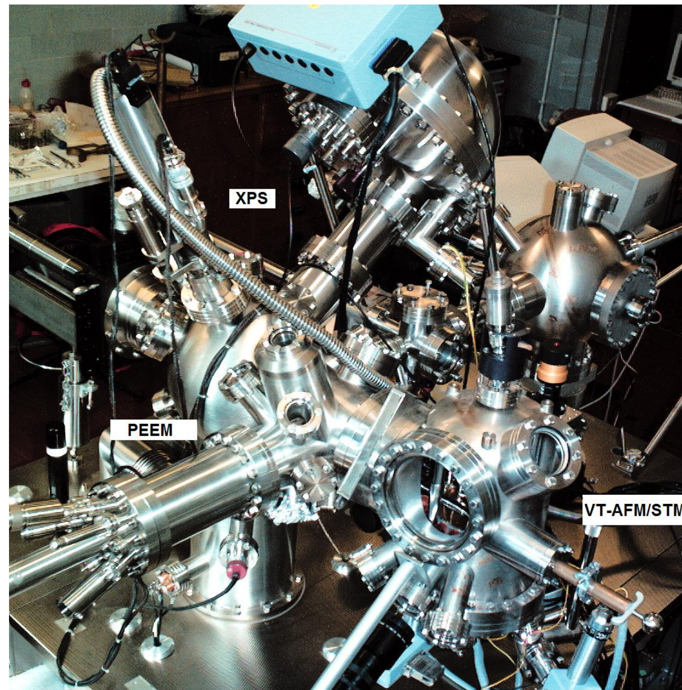

FIGURE 2.1. The UHV system: PEEM, XPS and AFM/STM are indicated

chambers have a x, y, z, θ manipulator with special wiring for sample heating. The manipulator of the analysis chamber has recently been updated with a cooling stage and an additional in plane rotation (tilt). The pumping system is composed by two ion pumps, one turbomolecular with a rotary stage and two titanium sublimation pumps (TSP). Ion pumps are necessary to reach $10^{-10} mbar$ range; their principle is to ionize residual molecules and collect them, by way of big electromagnetic fields. (For this reason 90% of the residual gases present in a UHV chamber is H_2). With gate valves in between the three main chambers and between the chambers and the pumps normal transfer operations can easily be done. The base pressure of the whole

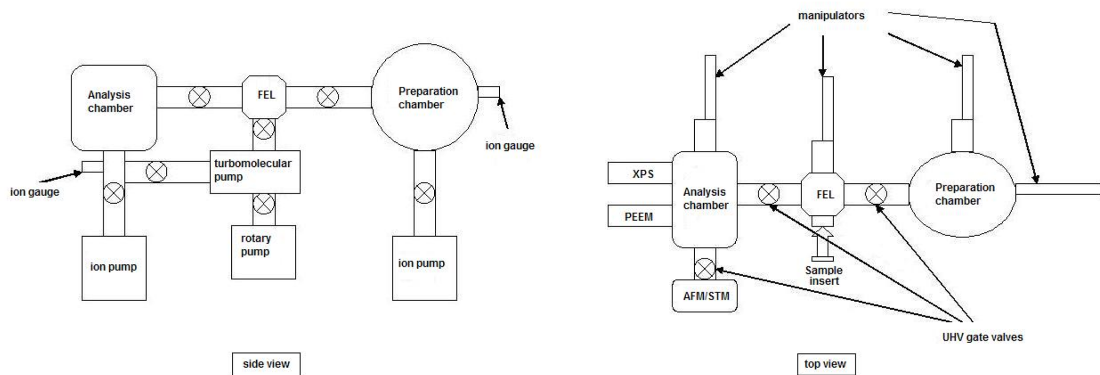

FIGURE 2.2. The UHV system scheme

system is reached exponentially with time and stays below $2.0 \times 10^{-10} mbar$. The final value of the pressure is the balance between the pumping speed and the internal parts degassing speed. Indeed this range of pressure is possible if any contaminants are avoided, where contaminants are species with high degassing speed at room temperature. Water and other ambient gas species adsorbed on the internal parts of the chamber are the limiting factor to reach UHV condition. To overcome this problem the whole system is normally *baked* for several hours to temperatures over 140 to 200°C depending on the specific instruments included. In our system the standard *bakeout* procedure is performed at a temperature of 150°C for 48 hours. Additional outgassing procedures must be done for filaments or other components

which have high temperatures during normal operations; ion gauges, TSP, X-Ray source must be outgassed after each bakeout.

In the next sections are presented the singular components of the system with their principle of operations.

2.2. AFM-STM

2.2.1. Brief introduction to NS-AFM. The use of piezoelectric resonators as distance sensors was introduced in scanning probe microscopies some years ago mainly driven by applications connected to near-field scanning optical microscopy. For dedicated scanning force microscopy (SFM), this technique was not widely taken into consideration, mainly because of low operating frequencies and the fact that dynamic non-contact or tapping mode techniques with standard cantilevers are already well established. Recently, a scanning force microscope based on a quartz needle resonator operating at a frequency of 1 MHz has become commercially available. A sketch of this force detector is shown in Fig. 2.3 The high operation frequency greatly increases the maximum possible scan speed which is the most severe limitation of this method. Moreover, as shown below, with appropriate tips this sensor even allows the acquisition of true atomic resolution images.

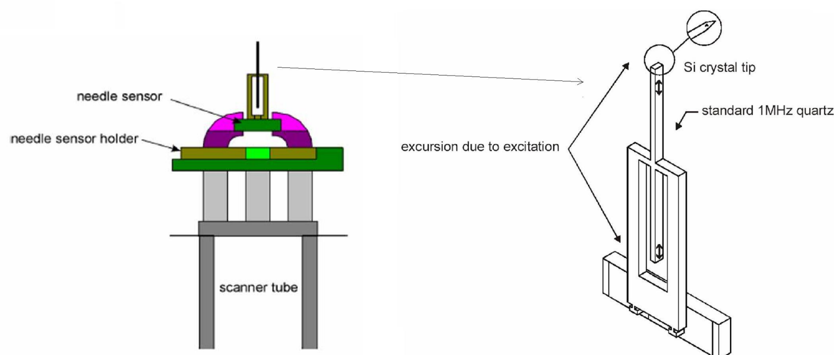

FIGURE 2.3. Scheme of the sensor stage (left) and detail of a microfabricated needle sensor (right).

We suggest that this surprisingly high resolution results from the low oscillation amplitude ($\sim 1\ nm$) made possible by the high mechanical stiffness of the quartz needle, especially in comparison to usual Si-based cantilevers. Until now, there exists no quantitative characterization of the frequency response as a function of the tip-sample interaction force. The first calibration procedure of needle sensor response has been presented by Clauss et. al [**21**] allowing at least an estimate of actual tip-sample forces. It has also been described a simple procedure to determine the amplitude of needle oscillation. In Fig. 2.4 it is shown a scheme for this procedure.[**21**].

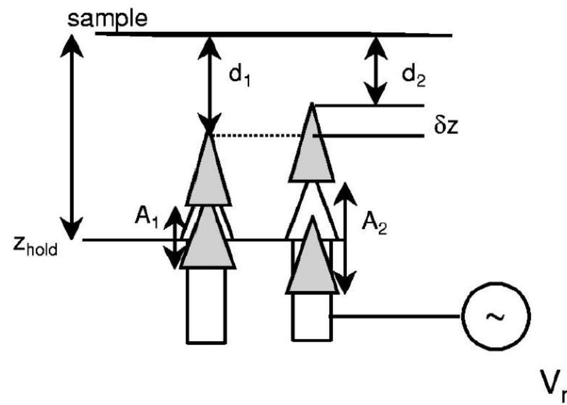

FIGURE 2.4. Setup scheme for the measurement of the oscillation amplitude. During stable tip-sample contact the distance is fixed to a value z_{hold}. Afterwards, the minimum tip-sample distance is decreased from d_1 to d_2 by increasing the amplitude from A_1 to A_2. [**21**]

The application of this procedure to many amplitudes yields values for the amplitude conversion factor D around 2 nm/mV. This can vary for individual needles due to dependence of the oscillation amplitude on Q factor. For sensor operation common excitation values are in the range of $0.3 \div 0.5\ mV$, resulting in amplitudes below or around 1 nm, small enough to explain the observed high spatial resolution. Moreover, a 1 nm oscillation amplitude will keep the tip in a distance range where

electron tunneling is possible during a large fraction of the cycle. Therefore, this sensor is well suited for simultaneous measurement of mechanical and electronic surface properties and for imaging samples with inhomogeneous electrical conductivity.

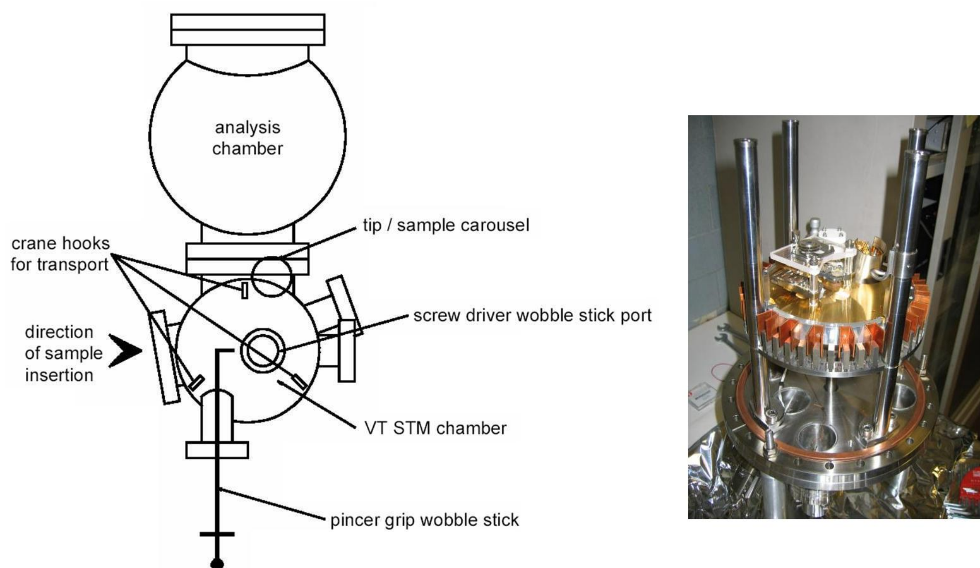

FIGURE 2.5. (left) Scheme of the UHV AFM/STM chamber. (right) The Omicron VT-AFM/STM out of its UHV chamber

2.2.2. Needle Sensor AFM. The needle sensor option for the Omicron VT SPM is a special scanner which allows AFM and combined AFM/STM operation using a needle sensor. Similar to non-contact operation in standard AFM, the needle tip is moved up and down at a frequency of about 1 MHz. Changes in the tip-surface distance (e.g. due to changes in surface topography) and in presence of a force gradient applied to the tip of needle sensor (i.e. due to interaction with sample surface) the oscillation phase is shifted respect to reference frequency. The phase shift could be used as a measure of the interaction strength between the needle sensor tip and the sample surface. Therefore it could be used as the feedback signal for Z-regulation.

2.2.2.1. *Experimental setup.* We used a Omicron $VT\ AFM/STM$ in ultrahigh vacuum (UHV) microscope. The instrument is capable of operation at temperatures below 40 K, but for the measurements reported here it was operated only under

ambient conditions. Electronic control of the microscope is provided by $SCALA^{©}$ software; it allows the operator to switch between different modes of tunneling, dynamic force, and conductive-tip force microscopy by the appropriate choice of the feedback signal and the use of either a standard metal tip or a needle sensor. In AFM mode, the feedback uses the phase shift $\Delta\phi$ between the needle output signal and the excitation frequency, which is adjusted by the software to match the piezo resonance. The sensor resonance measurement is a very important parameter for the image acquisition.

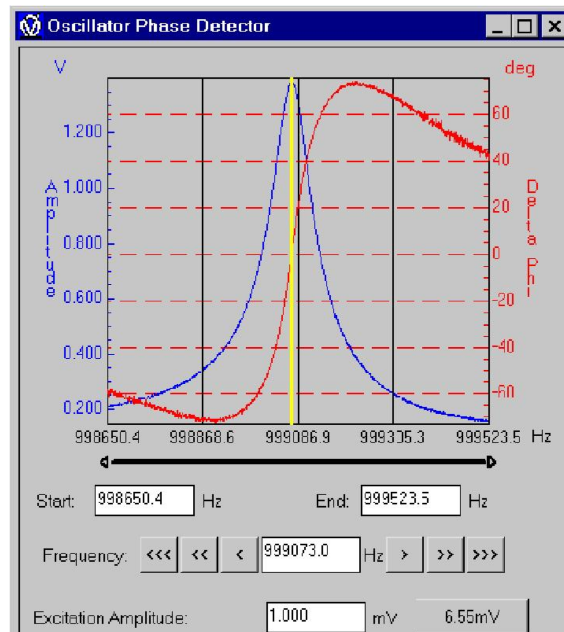

FIGURE 2.6. Example of resonance peak measurement for a NS-AFM tip. In the graph both amplitude and phase shift are plotted.

In fig. 2.6 it is reported a typical resonance curve (amplitude and phase shift) for a needle sensor tip. The right frequency value to be chosen lies in between the maximum of the amplitude (ν_{max}) and the crossing point between the two curves (ν_{cross}). The compromise is between a better z-resolution (more toward ν_{max}) and a better lateral resolution (more toward ν_{cross}).

2.2.3. STM experiments. The standard setting up experiment for the STM is the measure on atomically flat surfaces previously prepared to achieve atomic

resolution with the STM tip. This experiment is normally done on Si(111) face as it reconstruct in the 7×7 geometry as it has been described since 1983[**24**]. When (111) surface of Silicon is heated to sufficiently high temperature under UHV conditions the surface atoms rearrange for a more energetically stable configuration called 7×7 reconstruction. The new arrangement involves several types of atomic positions in the top three atomic layers to form a much larger unit cell. In fig. 2.7 is shown a typical image on Si(111) reconstructed surface. From this measurements the rhombohedral unit cell is clearly bounded by the lines of minima with deep corners. The diagonals can also be estimated: (27 ± 2) Å and (53 ± 4) Å, in good agreement with literature [**24**]. The long diagonal is less accurately determined since thermal drifts are more effective in that direction.

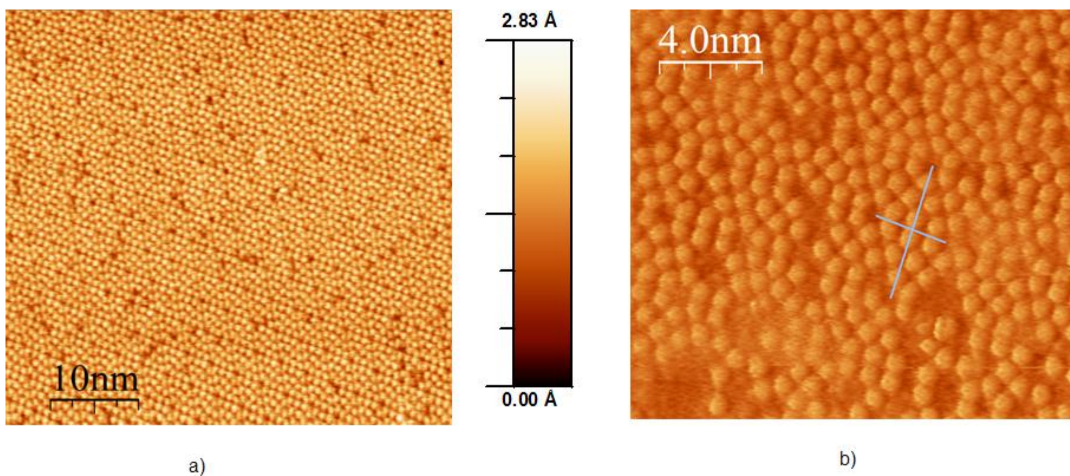

FIGURE 2.7. STM image on Si(111) with standard W tip and bias voltage of 2 V. After annealing at 1100 K and flashes at 1250 K the surface reconstruction is the well known 7×7. The measure of the rhombohedral diagonals is in good agreement with crystallographic data and literature reference.[**24**].

2.2.4. Experimental photoemission setup. An XPS photoemission spectrum measures the energy distribution of electrons which are emitted from a solid after illumination with an X-ray source. Our system include:

- the DAR400 X-ray source with Al and Mg anodes;

- the EA125 electron multi-channel analyzer.

2.2.4.1. *Electron Energy Analyzer.* Hence an essential part of the equipment to be used is the electron analyzer. Such analyzer will need to be able to collect a fraction of the emitted electrons, analyze them in energy and count them. A typical set-up used for this porpoise is the electrostatic hemispherical analyzer as schematically described in Fig. 2.8. It consists in three sections: a) the entrance lens; b) the dispersive section; e) the counting stage. It is clear that such equipment can only work in good vacuum conditions since the electrons should travel more than few centimeters and should not interact with residual gases, while high voltages should be applied without unwanted discharges.

The entrance electrostatic lens consists of an electron-optic that collects the photo-emitted electrons regardless their energy. According to the various types of experiments to be performed, such optic can be used in different way. It can select electrons coming from a small solid angle within the photoemission cone (typically less than 1 *deg*) in order to obtain the so-called angular resolution. It can select electrons coming from a small area of the sample (typically some square microns) to perform experiments of micro-spectroscopy. It can be used collecting the maximum number of electrons to enhance the transmission of the analyzer and to increase the counting rate. The dispersive section is used to analyze the energy of the electrons, which pass trough the entrance lens. Different types of dispersive lens can be used for this purpose. In fig. 2.8 it is shown a very common set-up which gives quite good performance. It consists of an electrostatic spectrometer in which the electrons are deflected between two hemispherical plates at different potential. The two plates at act as a condenser and their geometry and voltages determine energy of the electrons reaching the counter and the resolving power of spectrometer. The counting stage consists of 7 channeltrons, each connected to an electron-multiplier able to produce $10^5 - 10^8$ electrons for a single incoming electron. The number of current pulses produced by such multiplication will be counted and will be proportional to number

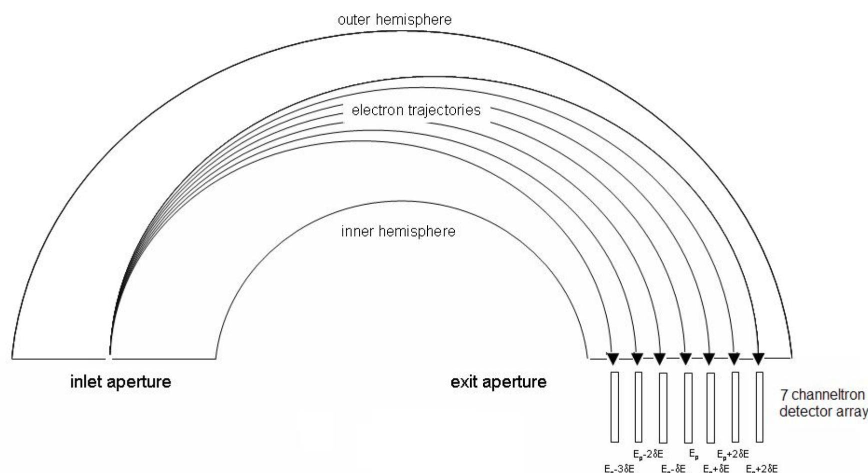

FIGURE 2.8. Schematic drawing of the hemispherical analyzer with the multi-channel energy dispersion

of photoelectron emitted at a certain energy with a given energy spread and angle of emission.

2.2.4.2. *Multi-channel acquisition.* In the Omicron EA125 multi-channel analyzer the observed intensity can be multiplied by up to a factor of seven by simply positioning extra detectors (channeltrons) at different positions in the exit plane, strongly reducing the acquisition time. When the kinetic energy is scanned, these extra detectors will measure spectra which are offset in energy from the true spectra by an amount proportional to the pass energy and also to detector position relative to central channel.

This energy offset is equal to the pass energy multiplied by an individual dispersion factor for the channeltron position in the exit plane,

$$\delta E = E_P \times D \tag{2.35}$$

where δE is the energy offset, E_P is the Pass Energy and D the dispersion factor. The software is configured to take the energy dispersion into account when scanning in MCD mode and offset the acquired spectra by the correct amount before summing each channel. After calibration there should be no significant loss in resolution when

scanning in multi-channel detector (MCD) mode, compared to scanning in single channel mode.

2.2.4.3. *Peak-width Measurement.* When the analyzer is used to measure peak position and peak shape precisely for chemical information the measured peak width is important and should be reduced to the lowest possible level for high resolution analysis. The line width of the exciting photon is often the major limitation on the resolving power of the instrument. Typical values range from a few meV (VUV discharge lamp) to 0.85 eV (unmonochromated sources: $AlK\alpha$ at 1486.6 eV and $MgK\alpha$ at 1253.6 eV). The theoretical linewidth of ultra-violet radiation from a VUV discharge lamp is limited by two processes, Doppler broadening and self-absorption. In practice, however the pressure of the discharge gas usually broadens the linewidth to between 3 and 7 meV. An X-ray monochromator will improve the resolution by reducing the width of the exciting X-radiation to about 0.2 eV to 0.3 eV.

2.2.5. XPS measurements procedure. Samples were produced and mounted on sample holders suitable for XPS in a dry-box, and transferred from the dry-box to the XPS facility in schlenk tubes, under N_2. Samples subjected to electrochemical treatments have been transferred from the dry-box to the XPS machine by schlenk tubes, shortly before the electrochemical tests. The process has required exposing the samples to air for few seconds, the time required for placing the sample on the transfer probe in the fast entry-lock chamber of the spectrometer. No sizeable sign of sample degradation under extended acquisition times under the X-rays was observed for the samples. The experimental conditions adopted were $MgK\alpha$ photons, generated operating the anode at 14-15 kV, 10-20 mA. No charging was experienced by the hybrid species, as can be inferred from the Si $2p$ peak position, collected in table 1, coincident with literature reports, which assign a value of 99.7 eV to the Si $2p_{3/2}$ bulk component [**56**]. In order to produce a satisfactory result, the energy region of bulk Si and SiH_x related peaks has been fitted with three $2p$ doublets,

one for the main component, related to the bulk, and two additional spin-orbit split components, at both sides of the bulk feature. The values for the energy positions were left free to vary independently, while the 3/2 and 1/2 spin-orbit split Si $2p$ components had a common value of $FWHM$ and of Lorentzian-Gaussian mix, optimized by the fit, and the intensity ratio was fixed to the expected 2:1 branching ratio. The effects on quantitative analysis possibly generated by XPS measurements from oriented Si wafers because of photoelectron diffraction at preferential directions of electron collection [**57**], were minimized in the comparison, by mounting the $Si(100)$ wafers always with the same orientation with respect to the analyzer axis.

2.3. Spectromicroscopy with PEEM and SR

During the three years of this PhD project big efforts has been produced to have the possibility of characterize surfaces both from spectroscopic and microscopic point of view. This has been done by means of a novel laboratory tool available in our research group, the PEEM microscope; also measurements on our system has been carried out in the ELETTRA Syncrothron Radiation Facility in the beamlines dedicated to this field of study. In the following lines it is reported a description of the systems used and tested and a brief mention on SR techniques.

2.3.1. PEEM microscope. The PEEM (Photoemission Electron Microscope) essentially consists of an imaging electrostatic lens system and a UV light source for the creation of photoelectrons via photoemission. Fig 2.9 illustrates the basic principle. The photoelectrons emitted from the surface are imaged onto a channelplate for amplification and finally onto a fluorescent screen for direct inspection or observation using a CCD camera.

In contrast to SEM, the PEEM does not use a scanned probe beam, but the sample surface is uniformly illuminated by, e.g., UV light. This way beam induced damage of delicate surfaces is avoided. The magnified image of the surface can be observed directly and in real-time (even video frequency, if the photon intensity is sufficient) on the fluorescent screen. With respect to it's parallel image acquisition,

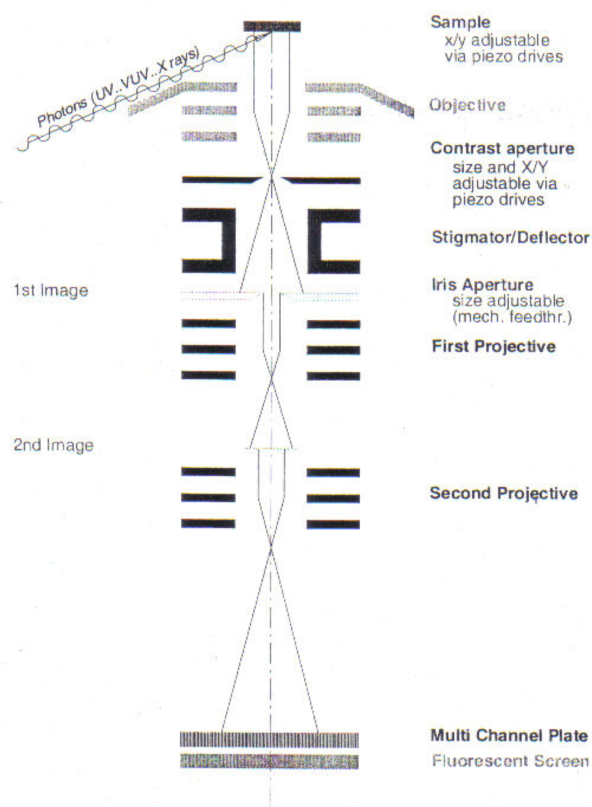

FIGURE 2.9. Principle of a PEEM.

the basic principle of operation is similar to an optical microscope. However, since electrons are used for imaging the resolution is no longer limited by the wavelength of the photon beam. Instead, a high electrostatic field in front of the sample accelerates the electrons released to energies of typically 10 to 15 keV. Thus a lateral resolution of less than typically 50 nm can be gained.

2.3.2. Syncrothron Radiation spectro-microscopic measurements. In the experimental framework of this thesis new and promising measurements have been done by means of spectro-microscopic techniques with Syncrothron light. The results obtained in the beamlines EscaMicroscopy and SpectroMicroscopy at Elettra facility in Trieste have given a big improvement to surface characterization of our samples. I will briefly mention the main characteristics of their experimental setup while a short description of the results are reported in section 3.6.

2.3.2.1. *EscaMicroscopy beamline at ELETTRA.* The ESCA microscopy beamline was designed to implement scanning photoelectron microscopy (SPEM), a technique for investigations of laterally heterogeneous materials. The light is provided by an undulator. It is tailored in order to fulfil the requirements of the zone plate focusing optics using a toroidal, pre-focusing mirror and a spherical grating monochromator with fixed entrance and exit slits. The experimental station consists of three

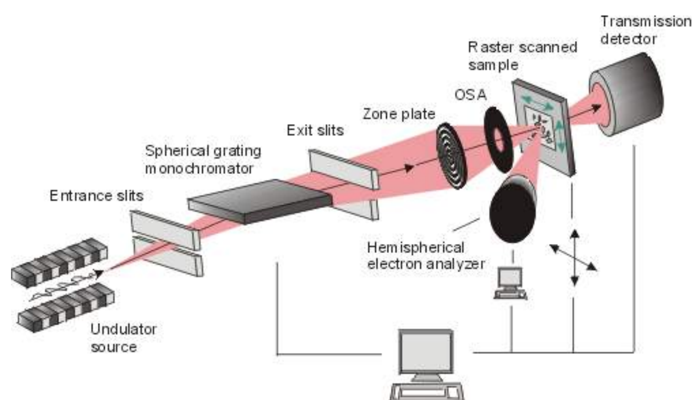

FIGURE 2.10. The experimental station of the beamline EscaMicroscopy at ELETTRA.

UHV vessels hosting the scanning photoelectron microscope, used exclusively for x-ray photoelectron (XPS) microscopy, and facilities for in-situ specimen preparation and characterization. The available photons due to undulator characteristics are at 496 eV and 780 eV.

2.3.2.2. *SpectroMicroscopy beamline at ELETTRA.* The availability of high brightness synchrotron radiation sources has led to the development of spectromicroscopy techniques which involve well-established spectroscopies that make use of x-rays and the high spatial resolution - below 1 μm - afforded by modern synchrotron radiation optical systems. Photoemission spectroscopy is one of the most important techniques in the domain of surface science. Through the analysis of the core levels, more specifically of their binding energy and "chemical shifts" thereof, one obtains information about the chemical composition of the sample's surface and about the atomic charge of the various chemical species. The investigation of the valence electrons provides insight about a manifold of electronic and optical properties of a

material and about the interaction of a material with molecules or atoms adsorbed on its surface, which is relevant for many surface chemistry phenomena such as catalytical reactions, corrosion or passivation. In the Spectromicroscopy beamline the

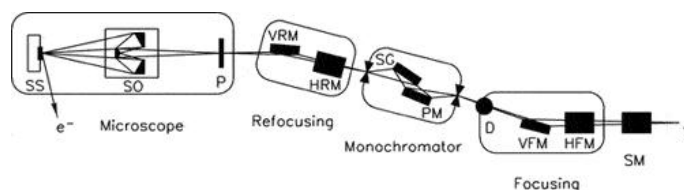

FIGURE 2.11. The experimental station of the beamline SpectroMicroscopy at ELETTRA.

high spatial resolution is obtained by focusing the radiation to a submicron spot onto the sample (full width at half maximum = 0.5 μm) while preserving good spectroscopic performances: typical count rates on prominent photoemission features are in the middle 105-counts-per-second range with an energy resolution better than 0.15 eV. This allows to collect good quality photoemission spectra from the submicron spot and/or to acquire "chemical microimages" of the sample by tuning the analyzer to a given photoemission feature and scanning the sample in the two directions perpendicular to the photon beam. The experimental station of the Spectromicroscopy beamline is a surface science facility consisting of several Ultra High Vacuum chambers interconnected through a sample transfer system which allows sample insertion from atmosphere. Besides the measurement station a sample preparation chamber is available, which is equipped with LEED, Auger, mass spectrometer, ion gun, metal evaporators, evaporation thickness monitor, gas dosing valves.

2.4. Mercury-Silicon junction apparatus

In fig.2.12 it is reported a scheme of the experimental setup used for the I-V characteristics measurements.

A microdrop syringe mercury electrode ("chemula") with a capillar diameter of 0.5 mm has been driven to the samples by an home built x, y, z micromanipulator. The contact area diameter has been estimated by a high resolution camera with 40×

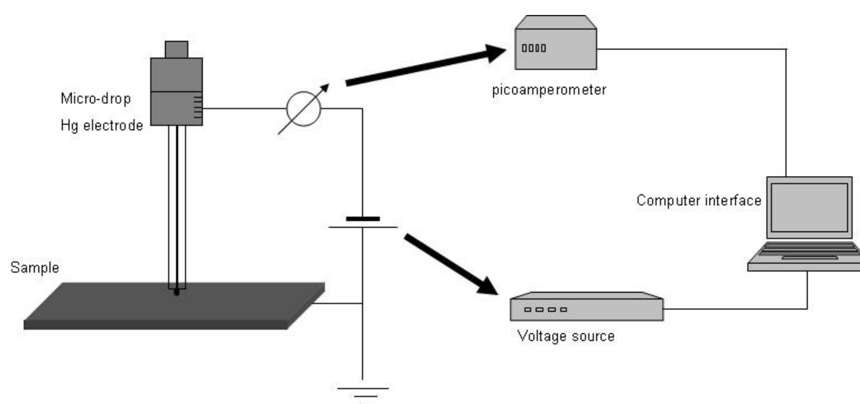

FIGURE 2.12. Scheme of the Hg-drop experimental setup.

objective. To avoid air contamination and/or electrical shorts between sample and Hg drop mainly due to water, which is always present in ambient conditions, the junction has been immersed in $n - decane$, which is a non-polar liquid.

The formed $Hg - sample$ junction has been connected with a programmable voltage source (Keithley 230) and an autoranging picoamperometer (Keithley 285) for the current measurements. Cable connections has been optimized in order to reduce noise level due to external causes. All the experiments were controlled by a self made computer program in a LabVIEW environment.

2.5. IPE experimental setup

In fig. 2.13 is presented the experimental setup of the IPE measurements implemented for the Hg drop/Si junction.

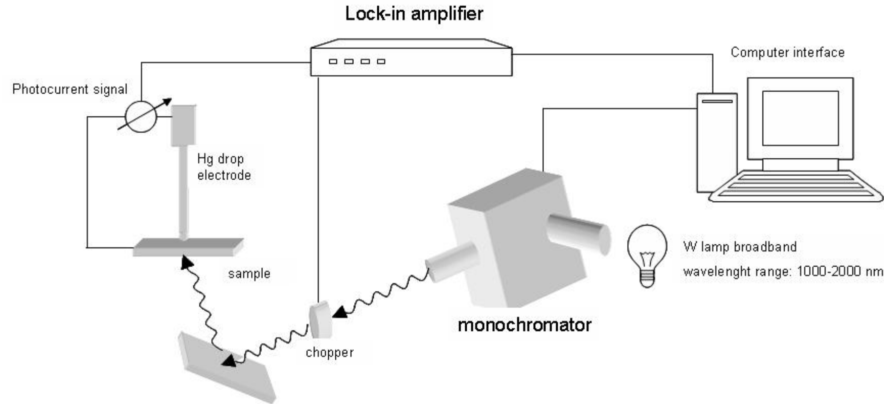

FIGURE 2.13. Schematic view of the IPE experiment integrated with the Mercury electrode system. The interface under investigation is the Hg/organic-layer/Si junction

2.6. The substrate: Si(100)

Silicon is a semiconductor with an intrinsic resistivity of $2.3 \times 10^5 \Omega cm$ and a band gap of 1.12 eV at 300 K (RT). Due to its insulating properties at RT, we used n/p doped Si substrates with a resistivity of 10^{-2} Ωcm. The increased conductivity induced by doping allowed XPS and other measurements which need conductive samples; no charging effect or binding energy peak shift has been found.

Silicon crystal structure is diamond like, typical of IV group elements, with four covalent bonds each atom. A picture of this structure is reported in fig. 2.14.

In the case of a single crystal, surface properties strongly depends on face orientation. The (111) face has the highest atom density and the lowest surface energy, while (100) has the lowest atom density and the higher surface energy. In this thesis the crystal face used for the experiments has been the (100). The lack of symmetry cause the presence onto a surface atom of dangling bonds. These atoms are particularly unstable and can quickly react with other species, mainly oxygen and water,

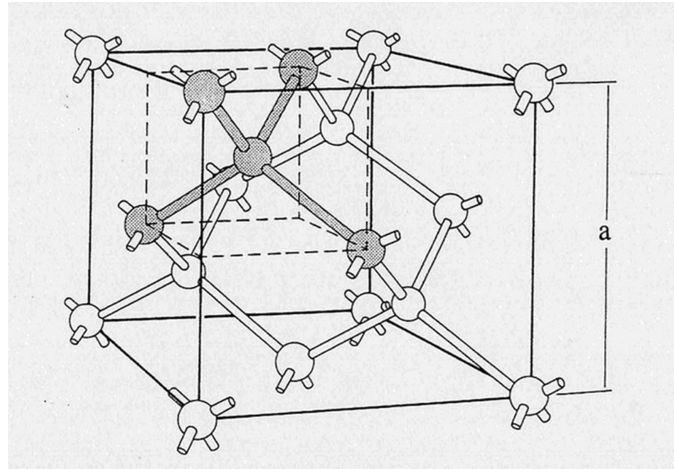

FIGURE 2.14. Si crystal structure. The shaded part shows the elementary unit cell.

to form more stable and passivating layers on the surface. In fact under ambient air condition Si surface immediately form a thin oxide layer (native oxide); in water or water solution the terminating species can be hydrogen, hydroxide, oxide. Moreover due to imperfect cleaning procedure it is possible to find metallic, organic or ceramic species adsorbed on a Si surface. Fig. 2.15 shows how a not perfectly clean Si surface can be rich of different species, normally not wanted for fine surface experiments.

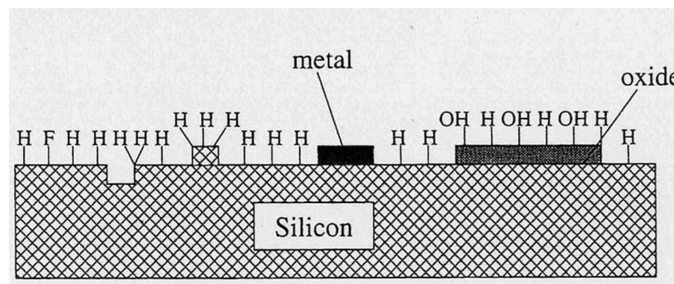

FIGURE 2.15. A possible Si surface.

2.7. Wet Chemistry process

The experimental procedure for sample preparation described in this section is what we call "wet chemistry process". All the stages from substrate cleaning to molecules anchoring are carried out ex-situ (out of the UHV system) and in solution.

N_2(g)-purged dry-box (Braun) has been used with standard preparative schlenk-line procedures to preserve samples from ambient air contaminants.

Several samples were prepared following the same route. Freshly etched Si samples were always used for the functionalization and the characterization measurements. Except for H-terminated Si samples, after functionalization, all samples were subjected to the same cleaning procedure, consisting of four sonication cycles, 5 min each, with different solvents (CH_2Cl_2 and CH_3CN), and drying in a stream of N_2. In the case of photochemical functionalization it is noteworthy that prolonged exposure times to visible light have resulted in the development of a surface deposit visible by eyes, which could not be washed out even by extended rinsing and sonication, perhaps related to a polymerization reaction of the vinyl function.

2.7.1. Hydrogen termination. Single-side polished Si(100) wafers (Si-Mat), $\sim 350\ \mu m$ thick, p-doped (0.02 Ωcm resistivity) and n-doped (0.01 Ωcm resistivity) with approximate areas of 1 cm^2, were prepared for hydrogen termination with a 5 steps procedure known from literature that we have standardized:

- washing in boiling 1,1,2- trichlorethane for 10 min and subsequently in methanol at room temperature, with sonication for 5 min;
- oxidation in $H_2O_2/HCl/H_2O$ (2:1:8) at 353 K for 15 min;
- rinsed copiously with deionized water;
- etched with 10% aqueous HF for 10 min;
- rinsed with water again, dried under a stream of N2.

All the used reactant are commercial products and they haven't been previously dehydrated since not necessary at this step. the first step itemized above perform a deep cleaning to remove any contaminant; then the oxidation make the surface smoother while removing the structural damage caused by the previous strong etching procedure. The final etching with HF remove the oxide layer to leave a perfectly clean and smooth surface. Several XPS and AFM measurements, immediately after

the hydrogenation process, show almost completely oxide free surfaces with roughness values comparable with atomically flat Si substrates.

Focusing on the substrate, all samples has been prepared starting from H-terminated Si and all the study has been based on its chemical activity. In the following paragraph three different methods of organic functionalization are described with reference to the specific molecules anchored.

2.7.2. Organic functionalization: thermochemical. The Si-C bond formation takes place at high temperatures ($\sim$ 150°C) by the typical reaction $Si–H \longrightarrow Si\cdot + H\cdot$. The functionalization is achieved by the deposition of the organic specie onto the Si wafer and heating up to necessary temperature. Linford and Chidsey [**39**] propose two distinct mechanisms to explain bond formation (see fig. 2.16). One possible way is that the residual fluorine from the reaction with HF can bind one Si atom as a nucleophile; the Si becomes pentavalent and an hydrogen atom is transferred to the alkene double bond. The forming carbanion breaks the Si-F polarized bond and forms the Si-C. Another hypothesis is that the alkene double bond has enough energy to act as nucleophile to the Si atom which becomes temporarily pentavalent while the exceeding electron is transferred to the C-C bond.

2.7.3. Organic functionalization: photochemical. UV light can cause the homolytic breaking of Si-H bond. Photochemical anchoring takes places at room temperature (RT), differently from thermochemical, and it can be useful for those kind of molecules which are strongly affected by high temperatures.

Calculation made on binding energies report that the minimal energy for the Si-H bond homolysis is around 3.5 eV corresponding to a wavelength of $\sim$ 350 nm. The formation of the free radical onto the Si surface is supported by the evidence of no polymerization processes expected if it was directly on the molecule. Stewart and Buriak have recently shown that even white light ($380 \div 730$ nm) can induce monolayer formation under ambient conditions and in few minutes[**40**]. This reaction requests for porous Si samples and from literature we found several examples

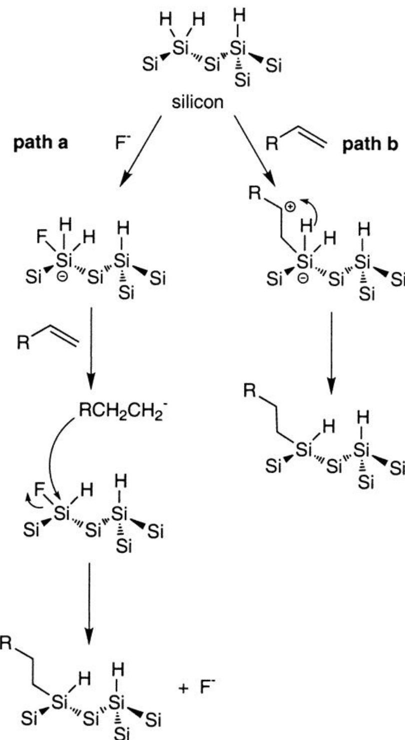

FIGURE 2.16. Scheme of the thermochemical method for anchoring organics on H-Si.

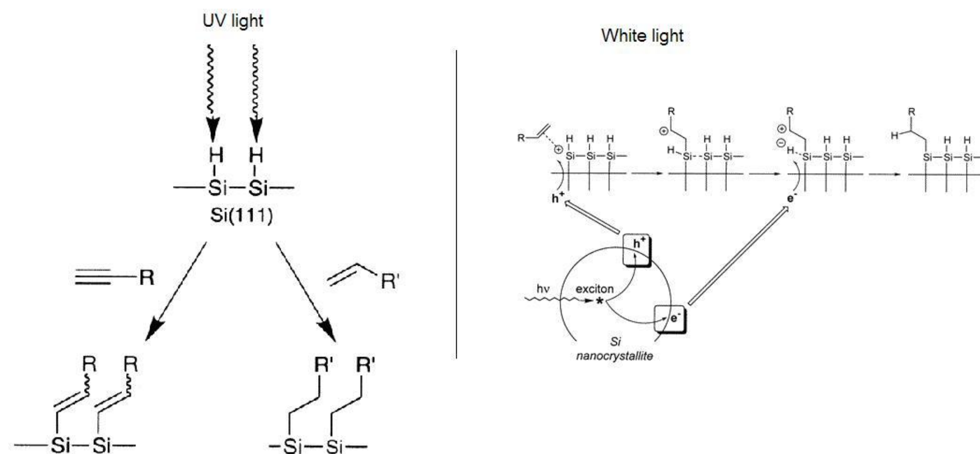

FIGURE 2.17. Scheme of the photochemical method for anchoring organics on H-Si with UV (left) or white light (right).

of photochemical anchoring on monocrystaline n-type Si which demonstrates the stability of berthed monolayers [**40**][**41**][**42**]. In the case of white light a scheme of reaction is proposed (see fig. 2.17). The mechanism is based on the formation of a

complex between the adsorbed alkene and a positive hole localized on the surface. The formed exciton is then responsible of H-Si bond breaking.

2.7.4. Organic functionalization: electrografting. The electrochemical method for the building up of compact organic monolayers on flat H:Si substrates is quite new. The big advantage of this anchoring technique is that in the electrochemical cell the Si wafer works as cathode so it can be polarized to a potential value at which oxidation cannot take place (cathodic protection); in fact the Si surface is electron rich during the cathodic electro-grafting process (CEG) so that nucleophilic behavior of water molecules present in the electrolyte is reduced, strongly limiting the probability of oxidation.

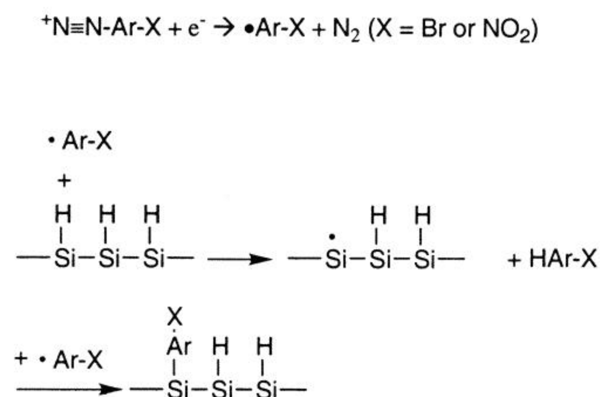

FIGURE 2.18. Typical scheme of the electrochemical method for anchoring organics on H-Si proposed by Henry de Villeneuve et al. [**43**]

The CEG method has been used to anchor alkyl chains molecules to Si. The procedure of substrate functionalization is similar to that shown in fig. 2.18. Alkyl bromide or iodide are available (commercially) which can be electrochemically reduced in-situ and form the Si-C bond. A solution 0.1 M of the alkyl halide and 0.1 M of the electrolyte, in anhydrous acetonitrile, can lead to high coverage ratios with a cathodic current of 10 mA/cm^2 for 2 minutes at RT. In the expected reaction mechanism the alkyl halide reduces to radical, followed by the extraction of a

proton which leaves a free radical onto the Si surface. At this step different ways are possible:

(1) the alkyl radical $R\cdot$ directly react with $Si\cdot$ forming the Si-C bond;
(2) $Si\cdot$ reduce to Si^- and can react as a nucleophile with a RX, producing a $Si - R$ leaving a free X^- or
(3) the in-situ reaction of $R\cdot$ to R^- can break the Si-H bond.

2.7.5. Molecules structures and properties. The molecules chosen for Si surface functionalization has been:

- ferrocene-derived;
- alkyl chains.

Ferrocene and ferrocene-derivated are metallorganic compounds characterized by one Fe atom between two cyclopentadienyl rings (see fig. 2.19). The Ferrocene ($(\pi - C_5H_5)_2Fe$) is an ambient air stable specie and it is soluble in organic solvents like benzene, ether , alcohol and insoluble in water, sodium hydroxide and chloridric acid. Its thermal stability is expected up to 500°C and it's structure is *sandwich* like, with 9° angle of out of phase between the two rings. The charge compensation state a $\pi - type$ bond between the orbitals d_{xz} and d_{yx} of the Fe, which has charge +2, and the two delocalized π orbitals of the aromatic rigs. The lost of one electron due to oxidation reaction cause the formation of the ferrocenium ion ($(\pi - C_5H_5)_2Fe^{+3}$). The charge state switching capability (redox property) of the Fe ion makes this specie a good system to study for the development of a molecule based device. While ferrocene is not covalently anchorable to Si, ferrocene-derivated molecules with a terminal group like CH_2, CH, OH or CH_2Br can be easily berthed to Si by way of the functionalizing procedure described in the previous sections. In fig. 2.19 are schematically presented the molecules studied in this work. The anchoring methods has been chosen taking into account the functional molecule group properties. An overview of the methods used are listed in table 1.

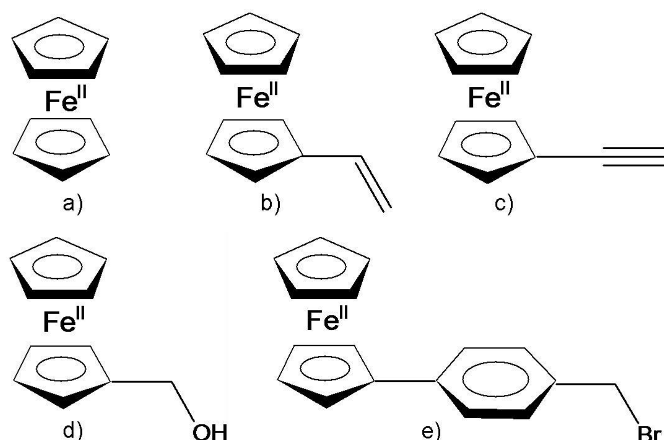

FIGURE 2.19. Schematic structures of the molecules of ferrocene (a), vinylferrocene (VFC) (b), ethinylferrocene (FCE) (c), methanolferrocene (FCM) (d) and benzilbromideferrocene (FBB) (e).

molecule	functionalization
VFC	photochemical
FCE	photochemical (electrografting)
FCM	thermochemical
FBB	electrografting

TABLE 1. Selected molecules with relative anchoring method

Alkyl chains molecules has been used to functionalize Si with the aim of reaching the highest possible coverage ratio in order to create a stable passivating layer. Indeed, the linear structure of such molecules allows packaging after functionalization better than ferrocenes. In this work we study alkyl chains with a carboxylic terminating group. In fig. 2.20 are presented the used molecules formulas. Elsewhere it has been reported an AFM and electrochemical study of these carboxylic acid molecules covalently anchored on Si surfaces. [**44**]. We report here a result which is important for our purpose. In the histogram of fig. 2.21 it is shown a comparison of the different functionalizing procedure, photochemical, thermochemical and electrografting as presented by Cattaruzza et al.; from this study as for the ferrocenes we

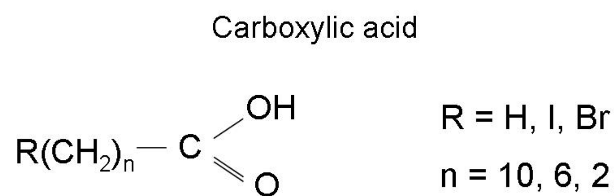

FIGURE 2.20. Schematic structures of the alkyl molecules with the carboxylic function. The halide termination is used in the electrografting fuctionalization process

can see that the CEG method is the more efficient with the highest coverage ratio (0.44 ML), close to the maximum theoretical value calculated for a flat Si surface.

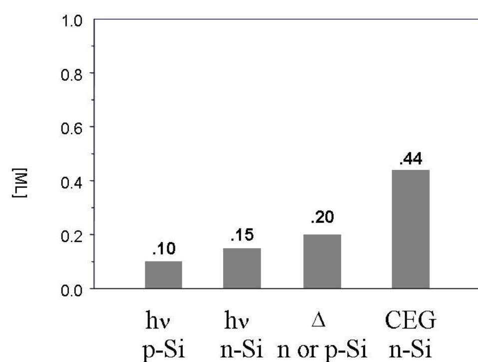

FIGURE 2.21. Carboxylic acid terminated monolayer concentration, on silicon nitride and silicon surfaces, expressed as monolayer fraction [ML], for different functionalization methods: thermal (D), photochemical (hn), cathodic electrografting (CEG).

CHAPTER 3

Ferrocenes on Si

The aim of this work was to fully characterize the molecule functionalization on the Si surface; I show, in this and in the next chapter the experimental results which confirm the covalent formation of the hybrid, the structuring onto the surface of the molecules and finally the electrical response of the interface Hg/H-Si and Hg/molecule/Si.

Two categories of anchored molecules has been investigated: ferrocene derivated and alkyl chains molecules. Although different variation of these species has been tested and studied, I report here the best results for the most promising and better reproducible systems: vinylferrocene and undecenoic acid. The first system has been fully characterized by XPS and AFM while the second was found to make a good passivation of the surface drastically changing its electrical properties.

3.1. Ferrocene on Si: Introduction

VFC on Si(100) is the object of a recent publication, where its reactivity as a gas-phase molecule on H-Si(100) (obtained by exposing a clean Si(100) surface produced in UHV to atomic H) has been explored by means of STM [**45**]. In this dry-chemistry experiment, a $Si-C$ chemical anchoring through the vinyl group has been proposed to result from the reaction. High-resolution STM images have revealed widened linear arrangements of molecules, a few nm long, and it has been proposed that the cyclopentadienyl rings form a V-shaped sequence on Si, in order to reduce the repulsive molecular interaction. The anchoring mechanism proposed is a radical chain reaction, generated by the STM tip by H abstraction from a H-Si bond [**39**],[**45**].

In the present work, the main issues are:

1. A simple and reproducible wet-chemistry recipe is proposed for VFC/Si, which leads to the establishment a robust Si-C surface-molecule bond, with negligible impact on the quality of the initial Si surface, and
2. The extent of preservation of such a bond is investigated in operating conditions of strict interest for further implementation of Si-based molecular electronics.

The substrate selected are the ones of choice in Si electronics, n- and p-doped Si(100), which have been hydrogenated via wet chemistry (see section 2.7). The first issue has been addressed by means of AFM and XPS, which have evidenced the surface morphology and composition. The second has required to follow the redox behavior of the hybrid species and its main results has been addressed in section 1.3.1. While a full electrochemical study is being reported elsewhere,[**46**] the presence of a true chemical attachment to the substrate, the hybrid stability as a function of extended redox cycles, and the redox kinetics of VFC/Si(100) are presented here, with the help of combined electrochemical and XPS measurements on the same samples.

It is widely accepted in the literature that Si surface functionalization performed with a vinyl insaturation as the molecular anchoring group, can lead to the establishment of a Si-C bond, provided that the conditions are met for a hydrosilylation reaction to take place between a surface $Si - H$ bond and the vinyl group of the molecule [**7**]. In the case of VFC, which is a solid with a low melting T (323 K), hydrosilylation can be obtained by formation of Si radicals through $Si - H$ homolysis, activated via UV- or visible-light exposure, or by heating. Alternative, more elaborate methods have been proposed for alkenes, as halogenation of the surface, [**47**] thermal reaction of Grignard compounds, [**48**] activation of the surface by radicals, [**39**] electrochemistry [**43**]. In the present study, an effort has been made to explore a simple, reproducible and mild anchoring route, which implies, i.a., to expose the H-terminated Si(100) surface only to one chemical during the delicate phase of anchoring. VFC photoimmobilization has been obtained by contacting the Si wafer,

kept slightly above the VFC melting T, with the pure substance under visible light, [**49**],[**48**],[**50**] for 1 hr, followed by extensive rinsing (see section 2.7). This is a modified procedure with respect to the visible-light assisted reactions reported in ref. [**51**] for vinyl- and ethynil-containing organics, where 0.1 M mesitilene solutions of the unsaturated molecules have been contacted with Si for 15 hr. Considering that Si-H homolysis requires UV light,[**7**] a mechanism has been proposed, originally for white-light activation of photoluminescent nanocrystalline silicon, and more recently extended to Si wafers [**51**]. The mechanism implies that photogenerated holes, produced in the silicon substrate, are subsequently attacked by a nucleophile, as a $C = C$ bond. In partial support to this hypothesis, it has been reported that more densely packed monolayers of a variety of 1-alkenes, 1-alkynes and esterified-1-alkenes can be obtained, with the same process, on low-doped hydrogenated n- or p- Si(100) with respect to highly-doped p-Si, in line with the effects of the dopant on the band bending [**51**]. While it can be hypothesized that such a mechanism is operating in the present experiment, it is due to mention that thermal promotion can be also active, since vinyl-aromatic substrates covalently anchor on Si to an appreciable extent ($\sim$ 10%) even at RT in the dark, as reported, i.a., for styrene on Si(111) [**50**]. In agreement with the previous findings commented above, no significant difference has been noticed in the extent of functionalization obtained for the present samples (as deduced from Fe/Si XPS atomic ratios, see section 3.4) for VFC on n- or p-Si(100), with closely comparable high doping levels of the substrates. A large number of VFC/Si(100) samples have been produced along the procedure reported above and, in the following, the ensemble of experimental characterization is reviewed and commented.

3.2. VFC/Si: AFM

AFM images taken on freshly prepared H-terminated n- and p-Si(100) samples (Figure 3.1 (a) and (b), respectively) and their associated linear cross-section profiles (Figure 3.1(c) and (d), respectively) show that both surfaces were flat over large ($0.5 \times 0.5\ \mu m^2$) fields of view.

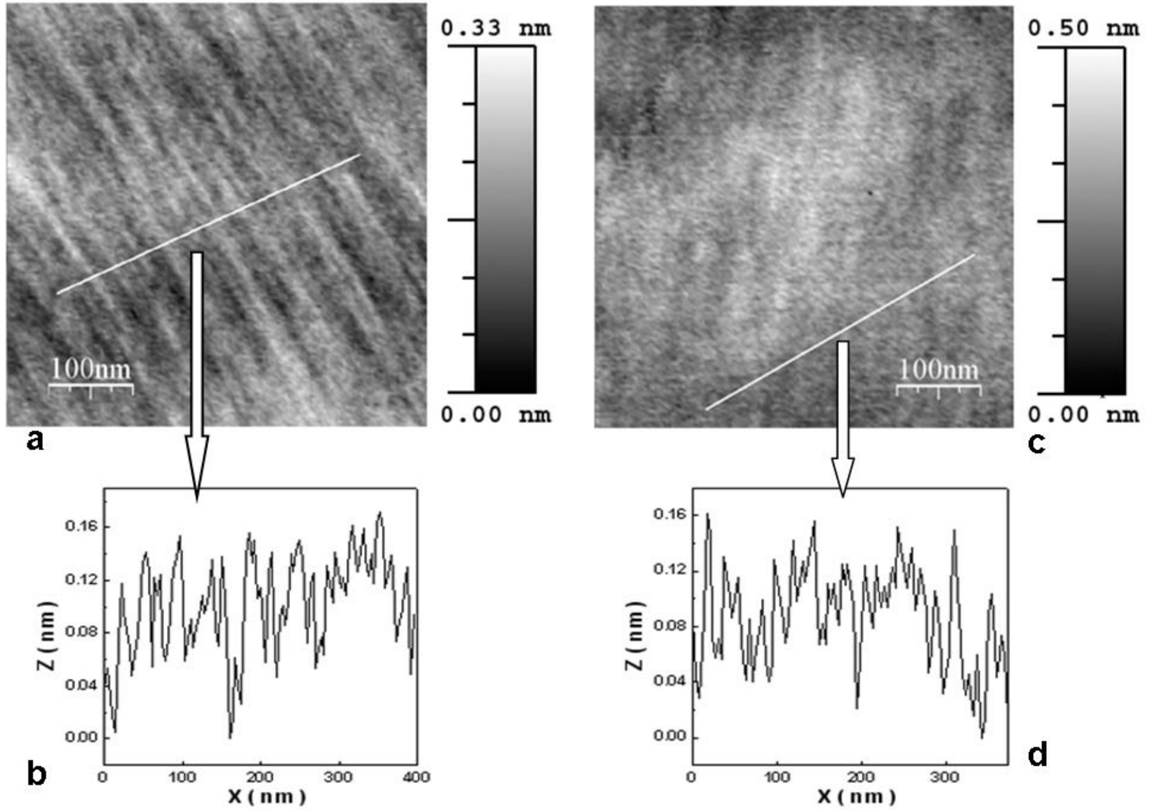

FIGURE 3.1. 500x500 nm^2 AFM images from clean n-Si(100)-H (a) and p-Si(100)-H (b) substrates. Corresponding linear cross-section profiles analysis (c, d) taken along the marked segments. The measured *rms* roughness values are 0.06 and 0.05 nm, respectively.

The corresponding values of rms roughness were 0.05 and 0.06 nm. In Figure 3.2(a), a $250 \times 250\ nm^2$ image from a freshly prepared sample of $VFC/p-Si(100)$ is shown, representative of the total area explored ($5 \times 10^5\ nm^2$). Structures like elongated grains are visible, $15 \times 30\ nm^2$ wide in the average, uniformly distributed in the whole region, without a long-range order. The *rms* roughness was 0.17 nm,

a small value, compatible with a monolayer (or a submonolayer) deposition, when compared with the roughness of the $H-Si(100)$ substrate. Close-up views (100×100 nm^2) and linear cross-section profiles analysis (Figure 3.2 (b) and (d)) show finer details of the cluster formations.

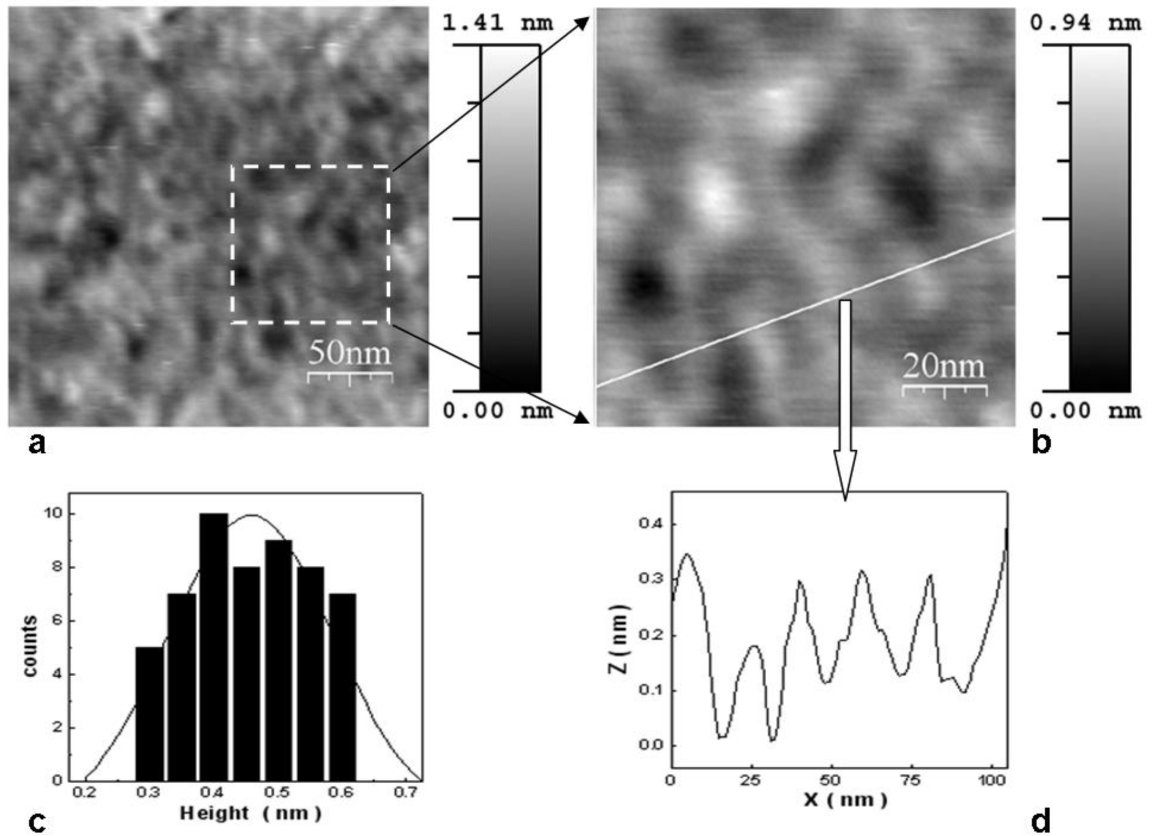

FIGURE 3.2. A 250×250 nm^2 AFM image from a freshly prepared sample of VFC/p-Si(100) (a); Close-up view (100×100 nm^2) (b) and linear cross-section profiles (d), from the same area; Gaussian distribution analysis of the heights taken from an overall 5×10^5 nm^2 area of a freshly prepared sample of VFC/p-Si(100) (c).

The average z-value of the grains has been determined by a statistical analysis from 54 height values, obtained from several cross-section profiles from the entire explored range of 5×10^5 nm^2. A Gaussian fit of their height values (Figure 3.2 (c)), taken from the entire explored area, has given a narrow distribution, peaked at 0.45 nm, with a standard deviation of 0.15 nm, and a lateral spacing among structures

in the 10-20 nm range. The obtained value of height is close to the diameter of a cyclopentadyenil ring (0.39 nm), and compatible with the distance between two cyclopentadyenil ligands in ferrocene (0.33 nm). The standard deviation of the Gaussian fit and of the rms roughness derived from large frame images closely compare (0.15 vs. 0.17 nm), and strenghten the results of the local statistical fit. Taken together, the AFM results from wet-chemistry functionalization of $VFC/H{-}Si(100)$ samples have revealed a surface morphology of the deposits compatible with the preferential molecular self-assembling in rows revealed by high-resolution STM images, reported for analogue samples obtained from gas-phase treatments [**45**].

3.3. FCE/Si: AFM

FCE/p-Si(100) samples have shown two typical structure formations. In one case (fig. 3.3 (a) and (b)) it is clear to see a rather homogeneous tissue of “bunches” with average lateral dimensions of $70 \times 70\ nm^2$; a good reproducibility of this formations on the surface has been found.

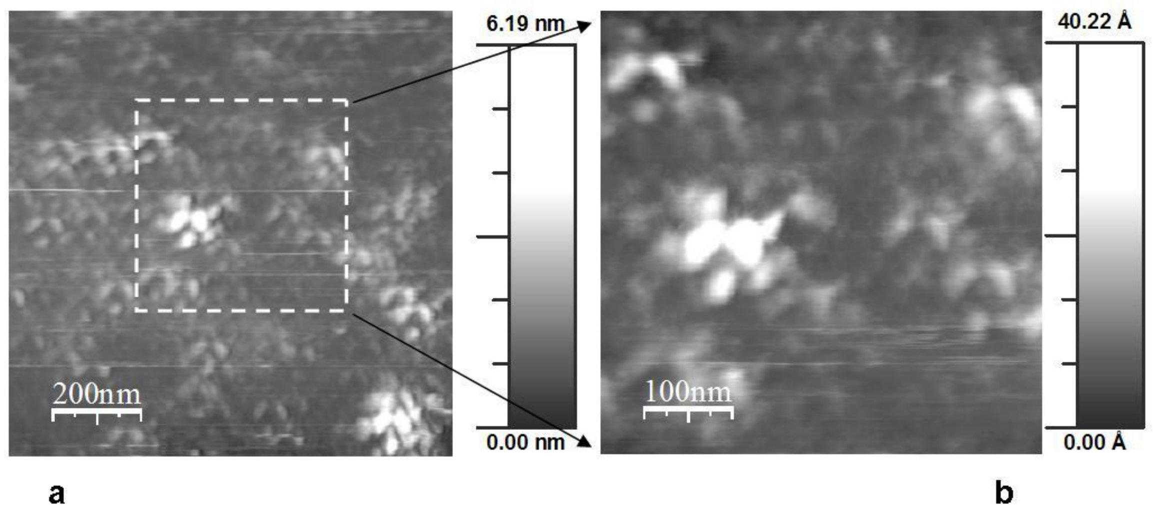

FIGURE 3.3. (a) FCE/p-Si(100) $1 \times 1\ \mu m^2$; (b) close-up view.

From the statistical analysis on these samples it was possible to estimate the values of the average height ($\bar{z}$=8.3 Å) and roughness (σ=6.7 Å). The other case (fig. 3.4 and 3.5) shows an ordered structuring of long and narrow grains disposed in the same direction. Their dimensions are approximately of 70×30 nm^2 and the height analysis returned an average of 1.9 nm for $\bar{z}$ and a σ of 0.9 nm. Indeed the structures on those samples seem to be assembled in two different ways with different values of $\bar{z}$ and σ. Since the high orientation and homogeneity in samples shown

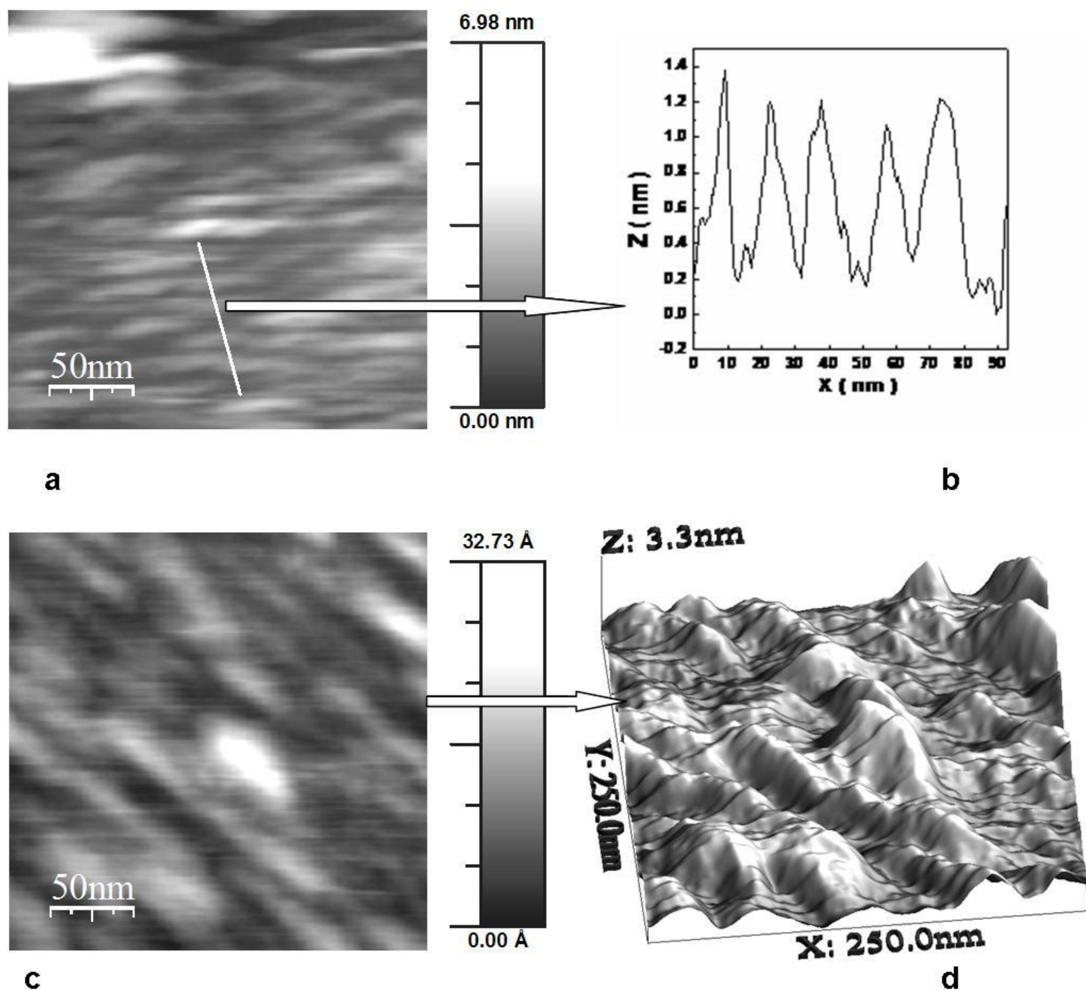

FIGURE 3.4. (a)FCE/p-Si(100) 250×250 nm^2 and (b) profilo z relativo; (c) FCE/p-Si(100) 250×250 nm^2, tilt angle $\theta = -45°$, and (d) 3D view.

in fig. 3.4 is considered a good and promising result, together with spectroscopy measurements (see. section 3.4.2), the presence of the other type of structures

remains unexplained: as it is suggested from XPS spectra, a possible hypothesis is that small silicon oxide nucleation areas are the responsible both of roughness increasing and bunches formation. Several experiment are currently under study to confirm this idea.

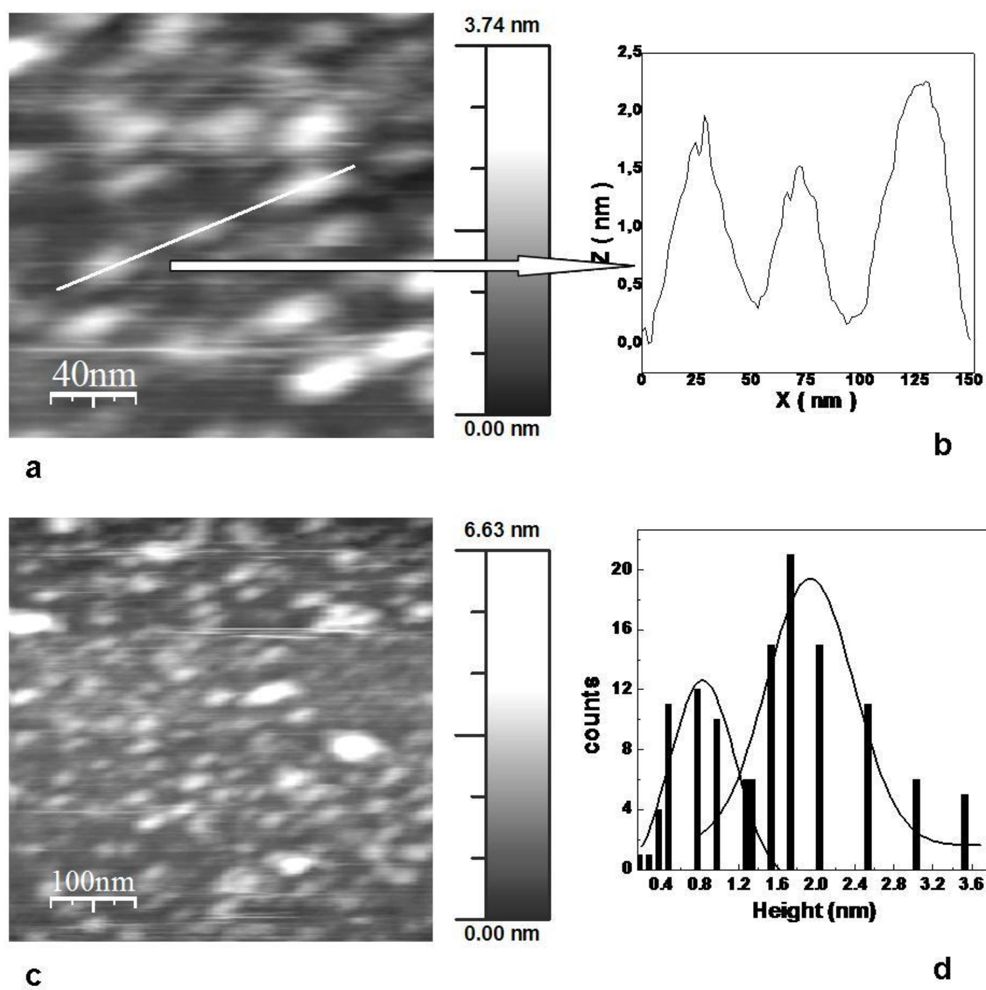

FIGURE 3.5. (a) FCE/p-Si(100) 200×200 nm^2 and (b) line profile; (c) FCE/p-Si(100) 0.5×0.5 μm^2; (d) Gaussian distribution analysis of the heights: two distinct structure heights are observed.

3.4. VFC/Si: XPS

3.4.1. Hydrogenated Si surfaces. A typical Si $2p$ XPS spectrum from a freshly prepared H-terminated $n - Si(100)$ is reported in Figure 3.6 (a), where the SiO_2 component is clearly visible as a feature separated from the bulk by 3.5-4 eV, the shift depending on the oxide thickness [**52**]. As for the hydride terminations, the Si $2p$ chemical shifts with respect to the bulk component have been previously reported as 0.2-0.3 (Si monohydride termination) and 0.35-0.6 eV (dihydride analogous), the uncertainty being related mainly to the low intensity of the components.[**53, 54, 55**].

The presence of chemically shifted Si $2p$ components, in addition to a variable amount of SiO_2, can be unambiguously inferred from inspection of Figure 3.6. A satisfactory fit was reached with the two minor components located at -0.7 and +0.55 eV and the SiO_2 characteristic feature at +3.5 eV, all referred to the bulk (see section 2.2.5 for details). The two latter values closely reproduce previous reports on H-Si. In the case of H-terminated $Si(100)$, the presence of an additional component on the low-BE side has been reported in the literature at $-0.25 \div -0.3$ eV, and related essentially to a surface correction to bulk silicon [**55**]. In a clean Si(100) reconstructed surface, the low BE region is dominated by the dimer-up subset of Si atoms, which has been located at $\sim -0.5eV$ from Si(0) [**54**]. In the present case, the negative shift is substantially larger than previously reported for the clean reconstructed Si(100) surface. Given the present limited resolution, we speculate that the negatively shifted component could be the assigned to an unsaturated Si atom bound to a positively shifted Si atom, as in SiH_2 (or even in $Si{-}F$ or $Si{-}O$). It is noticeable (and not contradictory) that a residual intensity at this energy position was found also after functionalization with VFC, since the functionalization process can generate hydrogen abstraction. The quality of the H-terminated Si wafers has been tested by determining the presence and extent of $Si - O$ components in the Si $2p$ ionization region [Figure 3.6 and Table 1].

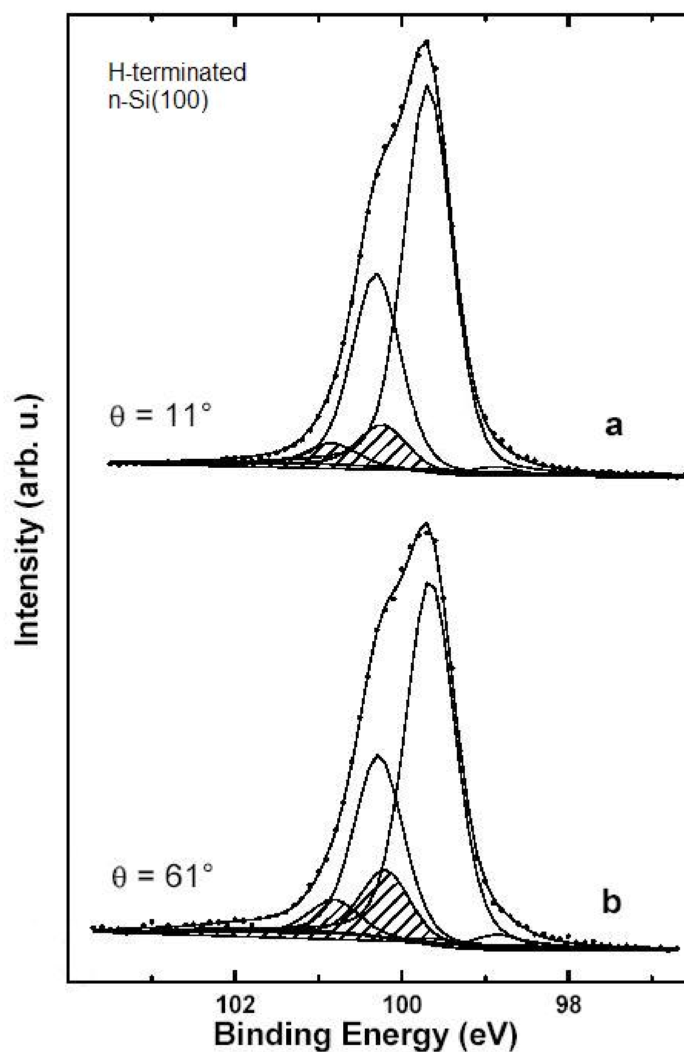

FIGURE 3.6. Si 2p XPS spectra from a freshly prepared H-terminated n-Si(100) sample, taken with non-monochromatized $MgK\alpha$ photons at a pass energy of 10 eV. The results of the curve-fitting procedure applied at two different photoelectrons collection angles, measured from the normal to the surface, are reported: (Top): 11°; (Bottom) 61°. The silicon hydride peak components are hatched.

The results related to the thickness of a silica overlayer, collected in Table 1, have been obtained from application of the already reported quantitative model for a silica layer grown on oriented Si surfaces,[**56**][**57**] which leads to the following

equation:

$$d_{ox} = \lambda_{SiO_2}(E_{Si}) \cdot cos\theta \cdot ln(1 + R_{exp}/R_0) \qquad (3.36)$$

where d_{ox} is the total oxide thickness (nm) due to the four different Si_xO_y species, $\lambda SiO_2(ESi)$ is the attenuation length of $2p$ photoelectrons from SiO_2, θ is the photoelectrons collection angle taken from the surface normal, R_{exp} is the measured $I_{Silica}/I_{Silicon}$ ratio and R_0 is the $I_{Silica}/I_{Silicon}$ ratio for the pure species. The product $\lambda SiO_2(ESi) \cdot cos\theta$ is the inelastic mean free path of Si $2p$ photoelectrons. The total oxide thickness coming from application of Equation 3.4.1 is a quantitative estimate of a continuous overlayer. The obvious implication of the very small values displayed in the case of freshly prepared VFC/Si samples is that the photochemical anchoring here adopted produces a surface well passivated by the attached molecules and by $Si - H$ residual bonds, with a surface oxidation limited to very small areas.

3.4.2. Functionalized Si surfaces. XPS was further used to characterize the presence, abundance and chemical state of the ferrocene derivatives, after anchoring. Direct assessment of the presence of a Si-C bond as a separate component in the Si $2p$ peak is routinely obtained when the substrate is clean Si, while in hydrogenated Si, mono- and dihydride components fall the same BE range. In the photoemission region of C $1s$, a confident localization of a $C - Si$ bond feature is hampered by the unfavorable ratio of the corresponding carbon atoms with respect to the saturated and unsaturated carbons belonging to the molecule (expected at 1-1.5 eV higher BE). BE positions of Fe $2p_3/2$ components and atomic ratios among characteristic elements, deduced from relative peak intensities, are collected in Table 1 for selected samples. For about 70% of the VFC/Si samples freshly prepared, the Fe/Si and the C/Fe atomic ratio were 0.06 and 12, respectively, while in the remaining cases some additional surface contamination reduced the first value and increased the latter. A value of 12 for the C/Fe equals the expected VFC stoichiometry and calls for the preservation of the molecular nature of VFC/Si. In all the investigated samples, Fe species in both (II) and (III) oxidation states have been found, the

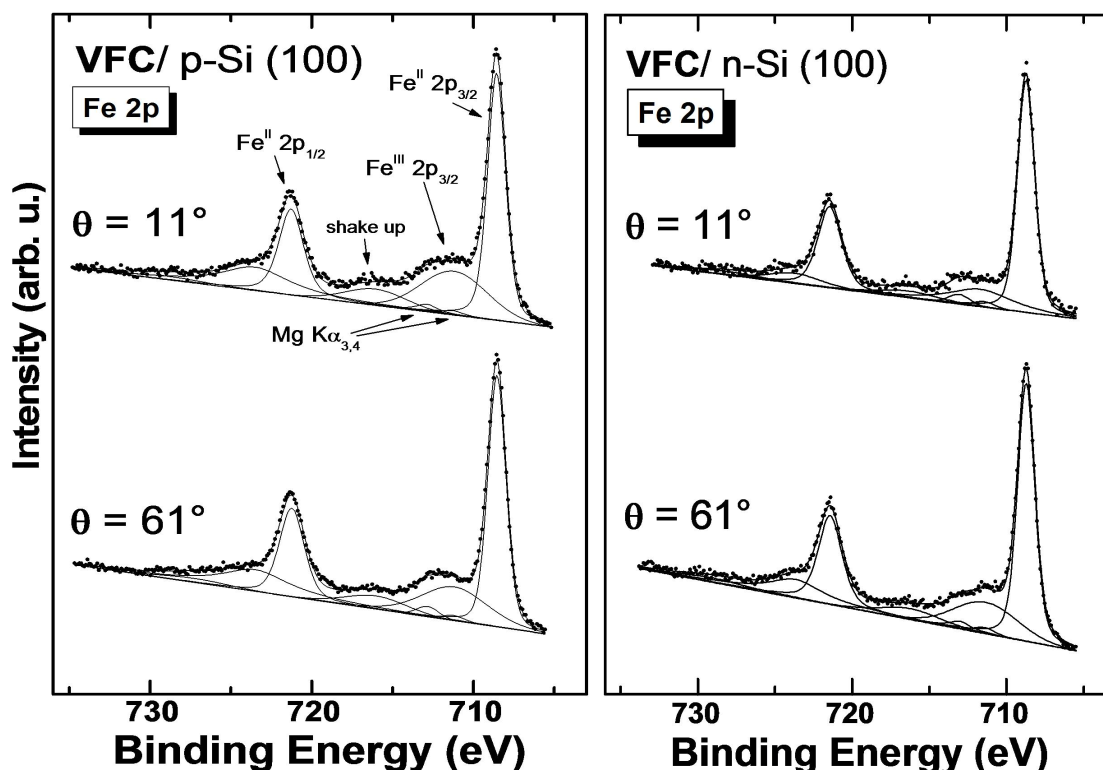

FIGURE 3.7. $Fe\ 2p_{3/2,1/2}$ XPS spectra from $VFC/n-$ (a) and $VFC/p-Si(100)-H$ (b) surfaces, taken at 11° and 61° photoelectrons collection angles, measured from the normal to the surface.

Fe(II) being largely predominant in the initially prepared ones. Curve fitting of the complex $Fe\ 2p$ peak envelopes has been applied, in order to separate Fe(II) and Fe(III) data sets.

The corresponding BE and FWHM values reproduce literature findings for pure and surface-reacted ferrocene and ferrocenium salts, respectively [**56**],[**59**]. The narrow FWHM of Fe(II) spectra for $VFC/n-Si(100)$ favors an assignment to a well-defined surface species. As for the Fe(III) species, a possible assignment to Fe_2O_3, which has been sometimes reported in surface-anchored ferrocenes,[**58**] can be confidently excluded on the basis of the main peak-to-satellite $Fe\ 2p_{3/2}$ energy separation and of the relative intensity of $Fe\ 2p_{3/2}$ satellite to main lines in Fe_2O_3 [**59**].

Sample	SiO_2 Overlayer Thickness (nm)	**AtomicRatios** Fe/Si	$Fe(II)/Fe(III)$	C/Fe	C/Si	O/Si	$Fe2p_{3/2}BE$ $(a)Fe(II)$ $(b)Fe(III)$
H – terminated **n – Si(100)**	–	–	–	–	0.14	0.059	–
H – terminated **p – Si(100)**	–	–	–	–	0.27	0.11	–
VFC/n – Si(100)	0.13	0.06	2.20	11.8	0.64	0.31	(a)708.5 (b)711.1
VFC/n – Si(100), after cv	0.70	0.035	0.97	26.7	0.93	0.73	(a)708.5 (b)711.1
VFC/p – Si(100) (sample 1)	0.25	0.06	2.09	11.3	0.67	0.33	(a)708.7 (b)711.3
sample 1, after 1min at +1V bias	1.03	0.02	1.98	49.0	1.1	0.73	(a)708.6 (b)711.2
sample 1, after 2min at +1V bias	1.12	0.02	1.97	61.5	1.3	0.88	(a)708.6 (b)711.2
VFC/p – Si(100) (sample 2)	0.37	0.035	2.31	15.9	0.53	0.35	(a)708.6 (b)711.2
sample 2, after 1st cv sequence	0.92	0.03	1.09	31.2	0.87	0.79	(a)708.7 (b)711.4
sample 2, after 2nd cv sequence	1.64	0.02	0.67	65.6	1.1	0.84	(a)708.6 (b)711.3

TABLE 1. Results from XPS measurements: Values for silica overlayer thickness (nm), obtained from application of an XPS quantitative model [**57**]; Relative atomic ratios for the reported samples, measured from XPS relative intensity ratios, after normalization to atomic cross sections and for a square root dependence of the photoelectron kinetic energy; Fe $2p_{3/2}$ binding energies (eV) for the Fe(II) and Fe(III) main components. VFC/p-Si(100) samples (1) and (2) have been obtained with the same initial procedure and subjected to different electrochemical treatments, as specified in the table.

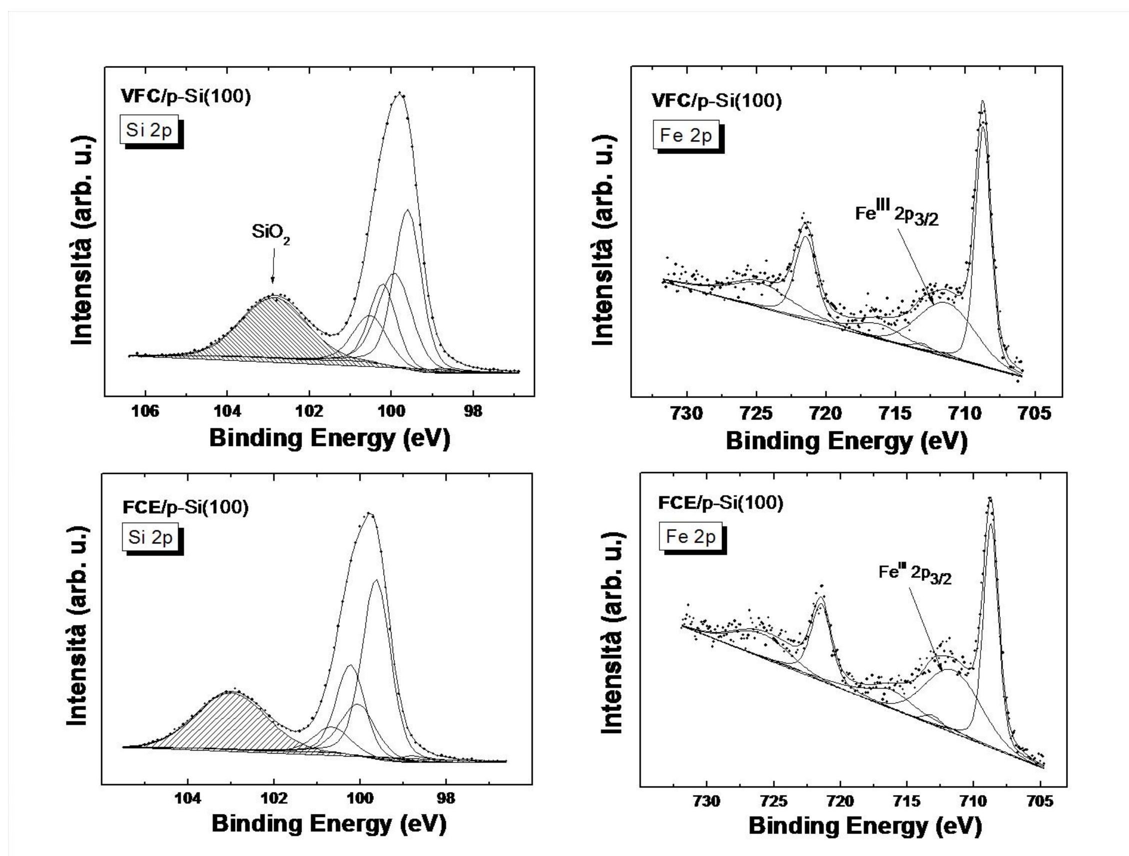

FIGURE 3.8. Si $2p$ and Fe $2p$ spectra of $VFC/p-Si(100)$ (up) and $FCE/p-Si(100)$ (bottom). It is clear the increasing of silicon oxide signal in both systems with a relative increasing of $Fe(III)$ signal respect to $Fe(II)$.

The relevant core peaks have been also taken at different photoelectron collection angles, measured from the surface normal. The $Fe(II)/Fe(III)$ atomic ratios, determined from the corresponding intensity of the Fe $2p_{3/2}$ component at 11° and 61° , are strictly comparable, as clearly visible in Figure 3.7.

The limited difference found do not present a definite trend for $n-$ and $p-Si$, and fall within the associated experimental uncertainty (10%). In the same sequence, the more noticeable effect observed has been the increase in intensity of the C $1s$ feature, which represents the topmost element, being about half of the Fe, Si, C, O atomic composition at grazing angle. The lack of a surface enrichment in one of the Fe components, while excluding local phenomena as the formation of ferrocenium

over silica, can be taken as a further direct evidence for the proposed assignment of $Fe(II)$ and $Fe(III)$ species to substituted ferrocene and ferrocenium both directly bound to silicon.

3.5. Selected Ferrocenes on Si: XPS study

In this section it is presented a selection of ferrocene-derivated molecules under spectroscopic investigation which shows differences and analogies between the different preparation processes mentioned in section 2.7. Three different systems are compared: ethinylferrocene (FCE/p-Si(100)) prepared via photochemical functionalization, methanolferrocene (FCM/p-Si(100)) via thermochemical procedure and benzylbromideferrocene (FBB/n-Si(100)) via cathodic electrografting. From the Fe

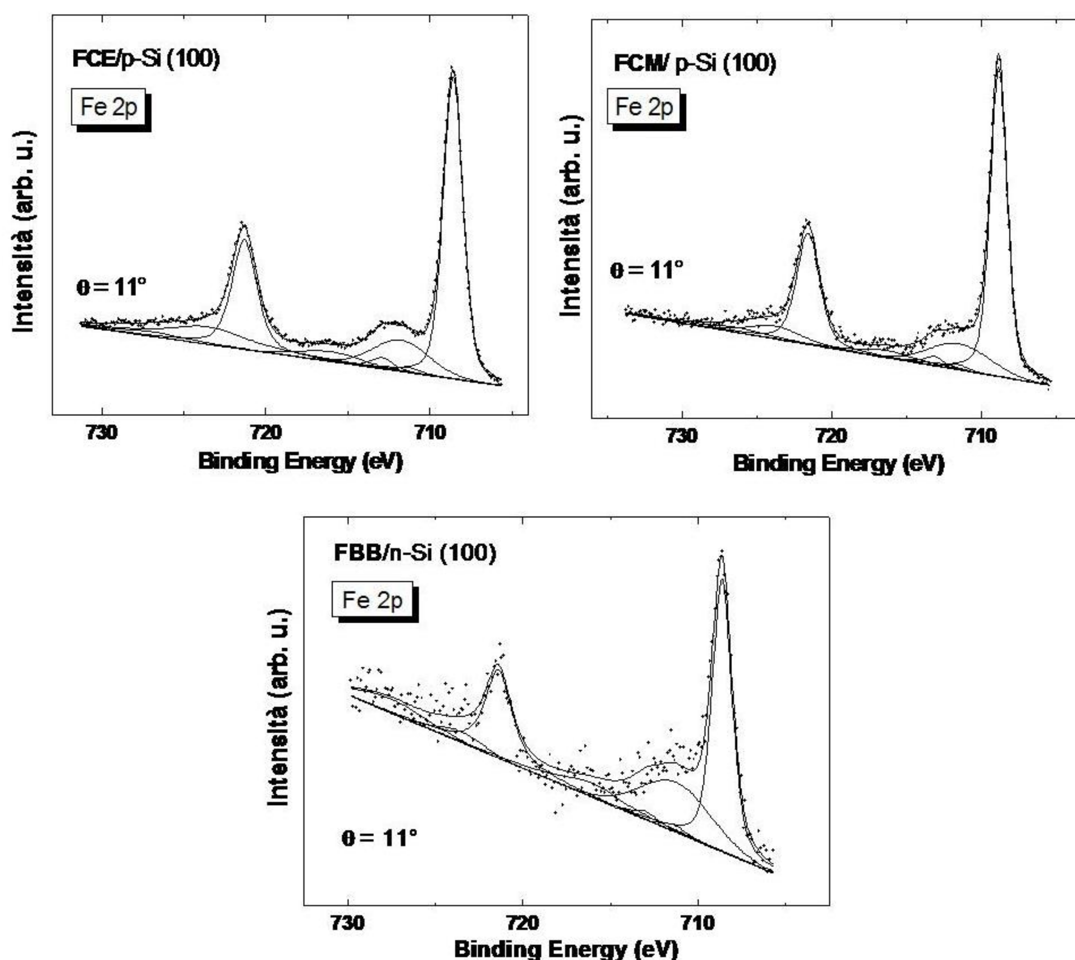

FIGURE 3.9. Fe $2p3/2, 1/2$ XPS spectra from $FCE/p - Si(100) - H$, $FCM/p - Si(100) - H$ and $FBB/n - Si(100) - H$ surfaces, taken at 11° photoelectrons collection angles, measured from the normal to the surface.

$2p$ spectra of fig. 3.9 it is clear that, except for FBB, the ferrocene/ferrocenium

species are present on the surface with the same relative amount (see also table 3). In fig. 3.10 are shown the Si 2p regions for the selected functionalized samples. The effect of the preparation procedure is evidently emphasized by the area of silica signal. Although it is expected that the surface thermally treated (anchoring of FCM) has a bigger amount of oxide due to temperature effect, the opposite is expected for the electrografted sample for that procedure works at a potential value which avoid oxidation (cathodic protection see section 2.7).

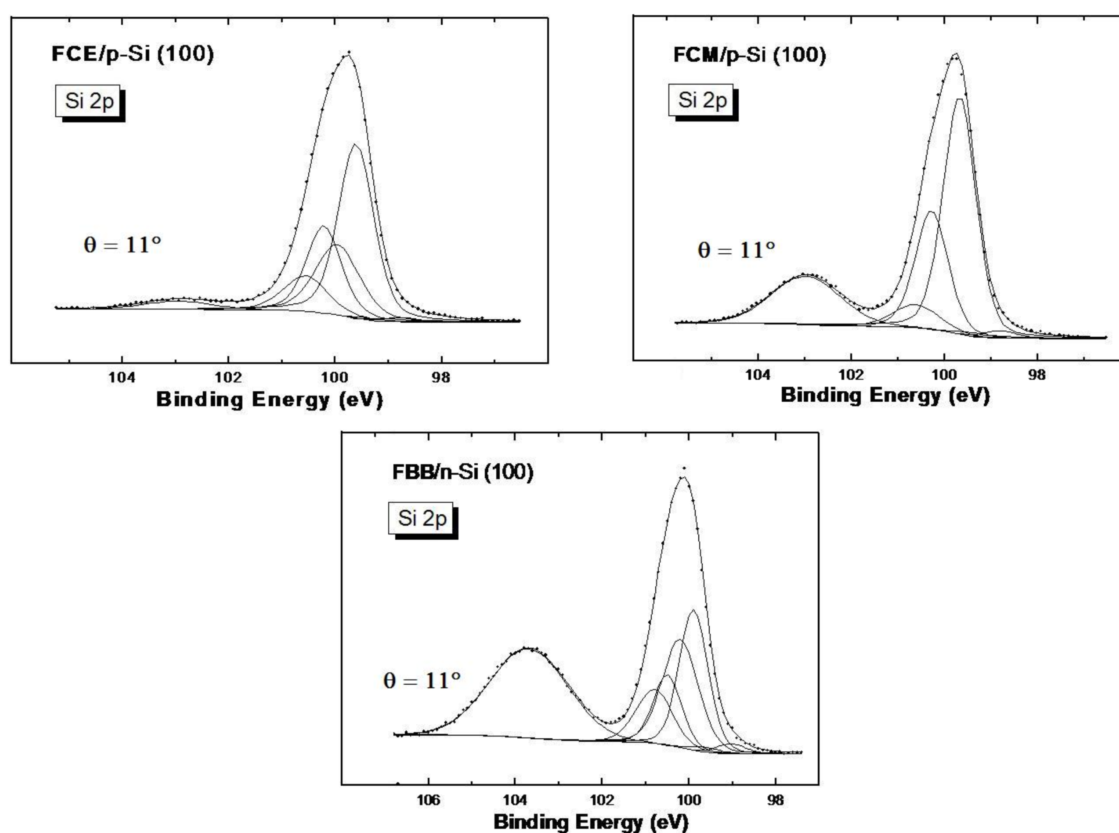

FIGURE 3.10. Si $2p3/2, 1/2$ XPS spectra from $FCE/p-Si(100)-H$, $FCM/p-Si(100)-H$ and $FBB/n-Si(100)-H$ surfaces, taken at 11° photoelectrons collection angles, measured from the normal to the surface.

The big SiO_2 signal area is explained since one takes into account the low functionalization efficiency of the FBB molecule, as it is also visible from table 3.

BE **FWHM(eV)**	**Fe(II)**	**Fe(III)**	**Fe(III) shake − up**
VFC/n − Si	708.5 1.33	711.1 4.8	716.0 4.4
VFC/p − Si	708.6 1.33	711.2 4.8	716.1 4.4
FCE/p − Si	708.6 1.42	711.8 4.0	716.1 4.4
FCM/p − Si	708.6 1.33	711.3 4.8	716.1 4.4
FBB/n − Si	708.6 1.33	711.3 4.8	716.1 4.4

TABLE 2. BEs and FWHM of selected samples from the Fe $2p_{3/2}$ ionization region.

	Fe(II)/Fe(III)	**SiO_2/Si**	**C/Fe**	*F*e/Si	**C/Si**
H/n − Si	–	< 0.01	–	–	0.14
VFC/n − Si	2.20	0.02	11.8	0.06	0.64
VFC/p − Si	2.09	< 0.01	11.3	0.06	0.67
FCE/p − Si	2.5	0.03	11.8	0.07	0.81
FCM/p − Si	2.1	0.26	17.2	0.05	0.93
FBB/n − Si	0.84	0.54	> 100	0.007	1.25

TABLE 3. Close overview o values for selected ferrocenes on Si, obtained from application of an XPS quantitative model [**57**]; relative atomic ratios for the reported samples, measured from XPS relative intensity ratios, after normalization to atomic cross sections (Scofield sensitivity factors)

The energy positions (BE) for Fe(II) and Fe(III) components shown in table 2 are in good agreement with recent studies on similar systems (ferrocene on Ag(100)) [**59**].

This is a good evidence of stability of the Fe ion independently from the system. It is worth noting that all samples showed no shifts from the expected ferrocene (Fe(II)) and ferrocenium (Fe(III)) energy position. In table 3 are collected the atomic ratios for the characteristics elements of the systems studied. It's important to notice that recurring values of the ratios $Fe(II)/Fe(III)$ (~ 2), C/Fe (~ 12) and Fe/Si (~ 0.06) reveal the reproducibility for some functionalizing procedure (VFC and FCE) and the stability of such molecules after anchoring on Si. Moreover the SiO_2/Si ratio, together with the *Silica Overlayer Thickness* value (listed in table 1), is a good indicator of surface protection.

3.6. VFC/Si: Spectromicroscopy

In this section are presented spectromicroscopy results on $VFC/n-Si(100)$, taken on the Synchrotron Radiation beamline ESCA-Microscopy at ELETTRA (TS). The raw data spectrum shown in fig. 3.11 presents the resolved spin-orbit Si $2p$ doublet with a relatively big silica signal. It's worth noting that the evident SiO_2 signal is due to the excitation photon energy used for this experiment, available at the beamline. With 446

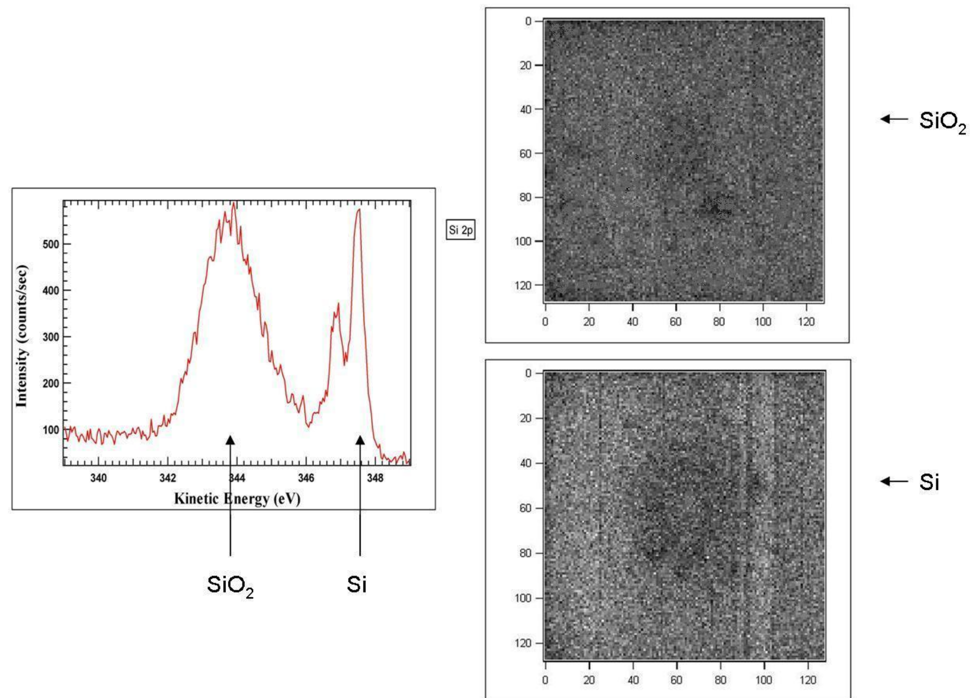

FIGURE 3.11. Spectro-microscopy analysis of $VFC-nSi(100)$ samples. Raw data spectrum in the Si $2p$ region (left) and images ($128\times128\times0.5\mu m$) taken at energies of Si ($KE=347.6\ eV$) and SiO_2 ($KE=343.8\ eV$).

eV the photoelectron escape depth is close to it's minimum value (few Å- see fig. 1.6) so that only the very first atomic layer is involved in the photoemission process. From the images shown in fig. 3.11 it is evident the prevalence of Si^0 signal (brighter lower image) over the SiO_2 one (darker upper). Moreover the lack of structures, clustering and/or contamination is a good indicator of surface homogeneous coverage within the imaging apparatus spatial resolution. The homogeneous distribution of photoemission signal is

clearly visible also in the image shown in fig. 3.12 and 3.13 taken at a kinetic energies of 391.5 eV (Fe 3p) and 163 eV (C 1s).

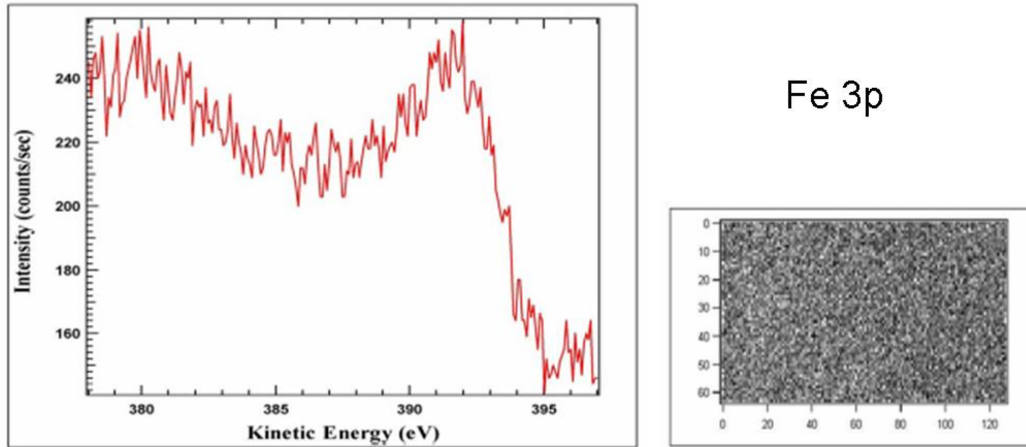

FIGURE 3.12. Spectro-microscopy analysis of $VFC - nSi(100)$ samples. Raw data spectrum in the Fe 3p region (left) and image ($128 \times 64 \times 0.5\mu m$) taken at $KE = 391.5\ eV$ (right).

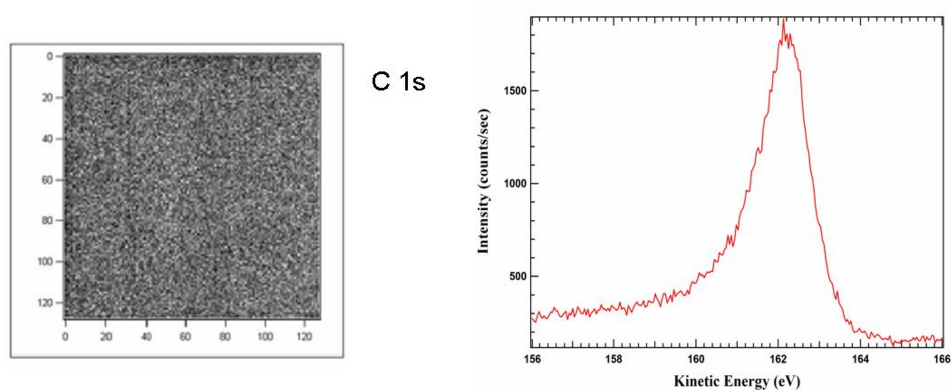

FIGURE 3.13. Spectro-microscopy analysis of $VFC - nSi(100)$ samples. Raw data spectrum in the C 1s region (right) and image ($128 \times 128 \times 0.5\mu m$) taken at $KE = 163\ eV$ (left).

CHAPTER 4

Alkyl chains on Si

4.1. Alkyl chains on Si: XPS

In this section are presented the XPS results on Si surface functionalized by undecenoic acid. As it was shown in section 2.7 the alkyl chain molecules display the best coverage ratio on the Si(100) surface with expected high packaging. Surface passivation is evidently shown by the Si 2*p* spectral region (fig. 4.1). The lack of SiO_2 signal, expected at 103.6 eV indicate that the electrografting process provided functionalization while keeping a good surface protection

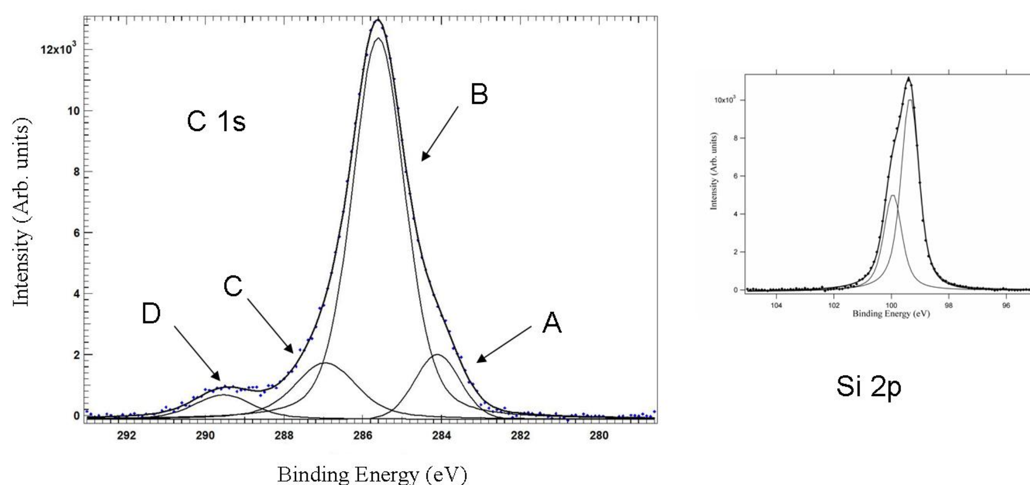

FIGURE 4.1. XPS spectra on $(CH_2)_{10}COOH/Si(100)$. The peak-fit analysis procedure for the C 1*s* signal has found four components assigned to the carbon atoms of the molecule. Si 2*p* spectrum showed no oxide presence.

A complex C 1*s* signal is also showed in fig. 4.1. From peak deconvolution analysis four mixed gaussian-lorentzian components has been found to give the best-fit. All the components can be attributed to C atoms of the molecule. Firstly it's natural to assign

the peak A lying at BE of 284.1 eV to Si-C bond. The eight equivalent atoms of the chain are assigned to peak B, lying at BE of 285.6 eV, which is coherently in a ratio of 8:1 versus the other peaks. This value is an underestimate of the real measured ratio, while we were taking into account the unavoidable presence of carbon contaminants. Peak C and D, respectively at BE of 286.9 eV and 289.5 eV, are assigned to the last two atoms of the chain. The first is in the middle between the 8 equivalent carbons of the molecule and the acid group while the other is directly bound to two oxygen atoms, providing for it the highest chemical shift. This results, together with those presented in section 2.7, address the $Si-(CH2)_{10}COOH$ system as one of the most promising hybrids for future molecule based devices.

4.2. Alkyl chains on Si: I-V characteristics

4.3. Molecule induced junction behavior

The most important process determining the current in a metal-semiconductor contact to which a bias voltage is applied is the flow of electrons over the top of the barrier from the semiconductor to the metal and viceversa. The barrier formation directly influences the behavior of the junction when a bias is applied. The transport behavior is regulated by the differences between the work function of the metal φ_m and the semiconductor φ_s (referenced to the Fermi level). These quantities gives the barrier height φ_b as it is stated by the Mott theory for a Schottky barrier.

$$\varphi_b = \varphi_m - \chi_s \tag{4.37}$$

where χ_s is the semiconductor work function measured from the conduction band minimum. If the simple Mott theory is valid the barrier height φ_b should depend on the metal work function φ_m. Experimentally it is found that the barrier height is a less sensitive function of φ_m and, under certain circumstances, φ_b is almost independent of the choice of metal [**60**]. Indeed, when φ_s is greater than φ_m the contact will have rectifying behavior for p-type semiconductors and ohmic behavior for n-type. On the other hand if the work function of the semiconductor is smaller than that of the metal the opposite will occur. The work functions of Hg and Si are respectively 4.49 eV and 5.17 eV. So we are in the first of the cases stated above. A picture of band alignment is proposed in fig. 4.2. Therefore

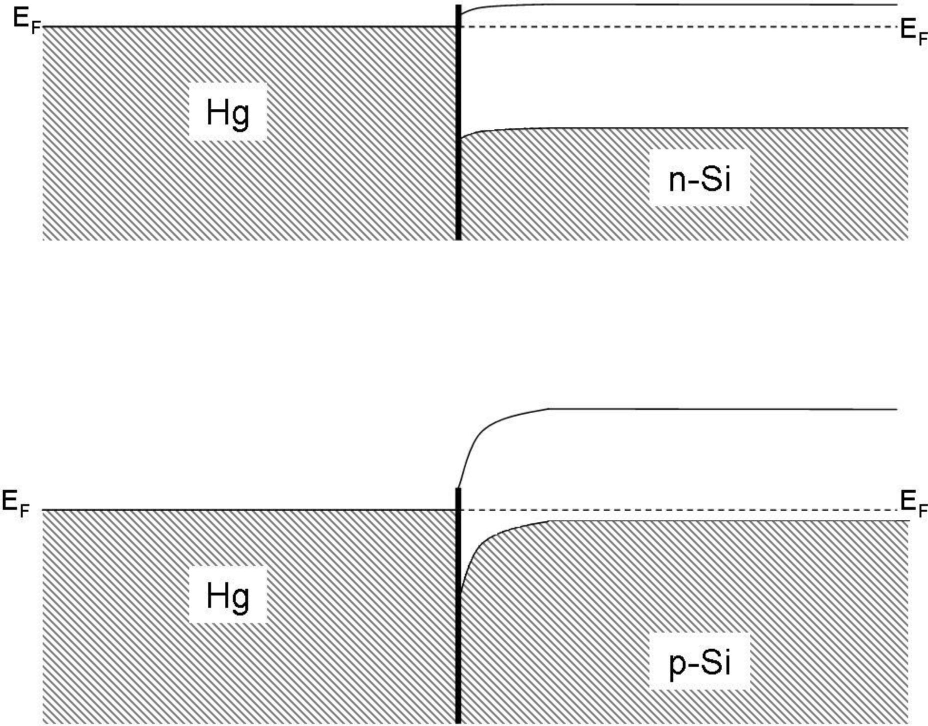

FIGURE 4.2. Schematic diagram of the proposed band bending occurring at the interface Hg/H-nSi (up) and Hg/H-pSi (down) junctions.

the electrical characterization on our systems ($Hg/H - nSi(lOO)$, $Hg/H - pSi(lOO)$, $Hg/(CH_2)_{10}COOH/Si(100)$) allows measurement of barrier height only for p-type substrates. Although this discussion helps us in the understanding the rectifying or ohmic behavior of the measured junctions this statement will require a discussion after the presentation of our results. In fig. 4.3 it is shown the slope of current density versus applied bias for the $Hg/H - nSi(lOO)$ and $Hg/H - pSi(lOO)$ junctions. In good agreement with a recent work [**14, 17**] it is shown a good rectifying behavior for the $Hg/H - pSi(lOO)$ contact while that for the $Hg/H - nSi(lOO)$ junction is close to ohmic. The conduction mechanisms can therefore be explained in the framework of the Mott theory stated above. The differences between the two type $n-$ and $p-$ of hydrogenated Si and Hg work functions is expected to be ohmic and rectifying respectively. The $Hg/H - nSi(lOO)$ system shows almost no difference between positive and negative bias and it can be considered an ohmic behavior. The $Hg/H - pSi(lOO)$ junction shows rectifying slope with 4 orders

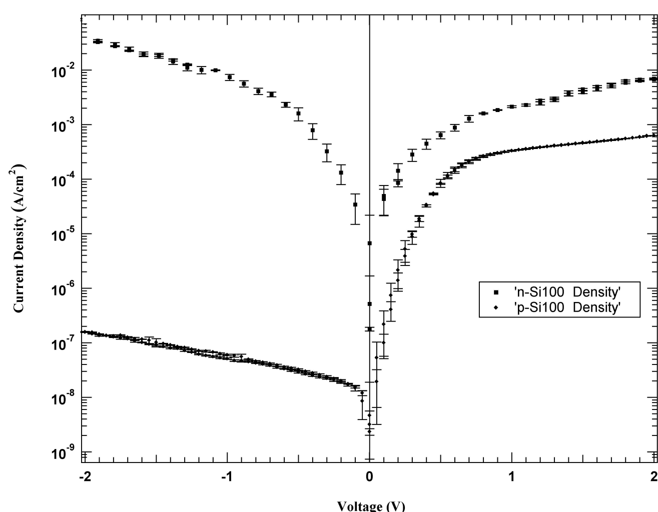

FIGURE 4.3. Density-Voltage characteristics for Hg drop contact with $H - pSi(100)$ and $H - nSi(100)$ surfaces. The first system (♦) shows a rectifying slope with 4 orders of magnitude difference between direct and reverse current density at $\pm 2\ V$ bias. The second (■) shows almost no difference between positive and negative bias.

of magnitude difference between direct and reverse current density at $\pm 2\ V$ bias. A comparison of $Hg/H - nSi(lOO)$ and $Hg/(CH_2)_{10}COOH/Si(100)$ is shown in fig. 4.4. The two systems show a drastic difference in the conduction properties induced by the covalently bound molecules. Although the contact between Hg drop and n-type Si should have

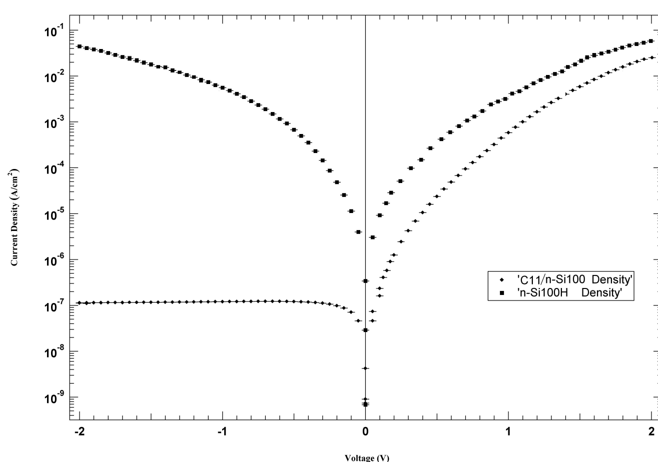

FIGURE 4.4. Density-Voltage characteristics for Hg drop contact with $H - nSi(100)$ and $(CH_2)_{10}COOH/nSi(100)$ surfaces.

$diode\ junctions$	$q\phi_{eff}(eV)$	n	$R_s(\Omega \cdot cm^{-2})$
$Hg/(CH_2)_{10}COOH/Si(100)$	$0,69$	$1,84$	$338,6$
$Hg/H-pSi(lOO)$	$0,65$	$1,44$	N/A
$Hg/H-nSi(lOO)$	N/A	N/A	$0,36$
$literature\ references$			
$Hg/SiO2-pSi(100)$	$0,56$	$1,43$	$0,24$
$Hg/C_{12}H_{25}-pSi(100)$	$0,66$	$1,33$	$0,50$
$Hg/C_{12}H_{25}SiO_3-SiO_2-pSi(100)$	$0,76$	$1,83$	$560,00$
$Hg/H-pSi(100)$	$0,83$	$1,14$	N/A

TABLE 1. Effective barrier height, ideality factor and series resistance of the junction extracted from the J/V characteristics. The reported reference data are from Liu et al. [**14**].

a (pseudo)ohmic behavior the presence of the molecules cause the changing of junction conduction mechanism to rectifying.

4.4. Barrier height measurement

In this section are presented the measurements of the photocurrent threshold for the mercury/silicon and mercury/molecules/silicon junctions. As it was described in section 1.7.4 barrier height and ideality factors can be extracted from J/V characteristics which follows the thermionic-emission theory, provided the forward bias is not too large. From the equations derived in section 1.7.4.5 the linear plots of $\frac{dV}{dlnJ}$ vs J and $H(J)$ vs J give us the values for the effective barrier height ϕ_{eff}, the diode ideality factor n and the series resistance R_s.
A comparison of the experimental data on our systems is presented in table1.

4.5. IPE experiment

IPE is a simple and direct measurement capable of unprecedented accuracy. It uses photons of sufficient energy to optically pump electrons over the conduction band discontinuities, producing a photocurrent. No complex modeling is required to extract the discontinuity from the experimental data, since it coincides with photocurrent threshold energy. Both linear and Fowler curve fits of the threshold region agree within an accuracy of $\pm 5\ meV$. The numerical values was derived by fitting the square root of the yield with a linear function: as in Fowler's theory [**61**], where $h\nu = E_g + \Delta E_c$ is the threshold energy. The linear fit according to Fowler produced the best fit; at any rate, the different power relations gave the same onset value within the experimental uncertainty.

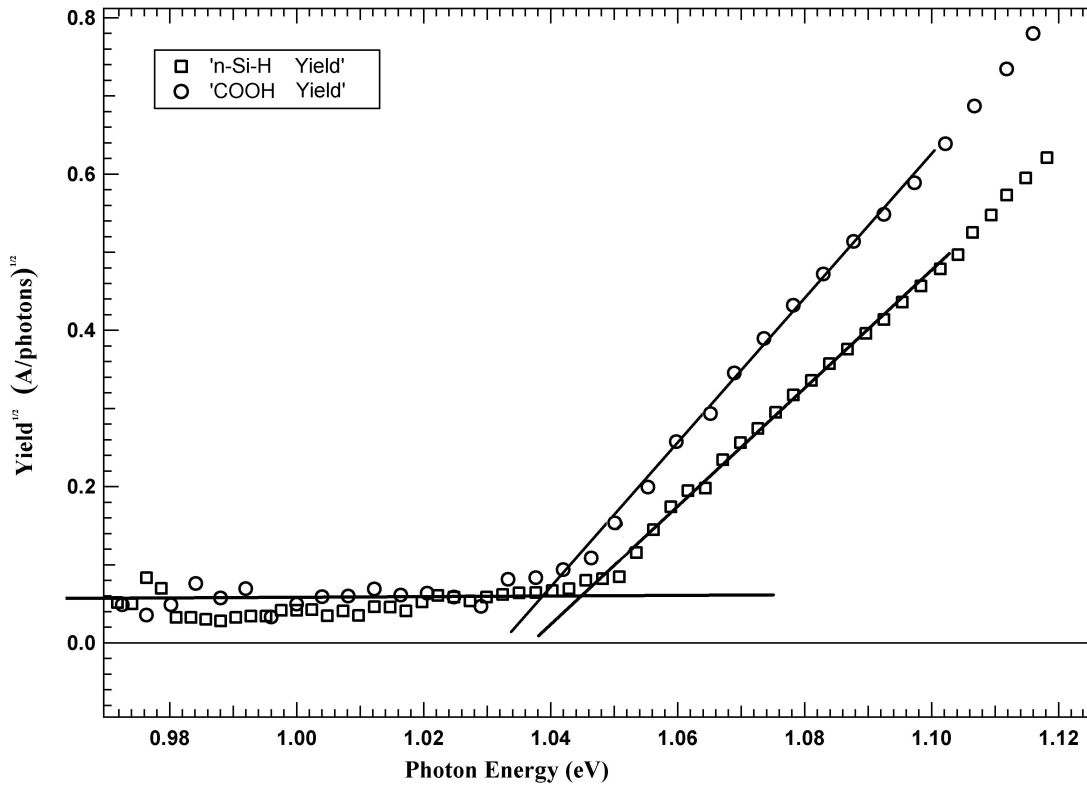

FIGURE 4.5. Photocurrent threshold for $Hg/H - Si(100)$ and $Hg/(CH_2)_{10}COOH - Si(100)$ junctions. Two different thresholds are visible in the plot of the square root of the photocurrent yield versus the photon energy.

From the photocurrent yield versus photon energy plot for the Hg/H-nSi(lOO) junction (Fig. 4.5) we could estimate a threshold at $1.045 \pm 0.003\ eV$. For $Hg/(CH_2)_{10}COOH/nSi(100)$

junction the IPE spectrum shows an onset at $1.038 \pm 0.003\ eV$. These results agree, therefore, with the intrinsic Si energy gap value of 1.12 eV reported in literature. The smaller values respect to Si energy gap and the small difference between the photocurrent thresholds of the two systems studied can be explained as follows. In both cases active doping states few eV below the conduction band minimum can contribute to photocurrent. These states can be surface defect states stabilized by H atoms. An analogous effect is expected for the functionalized Si surface. A scheme is proposed in fig. 4.6.

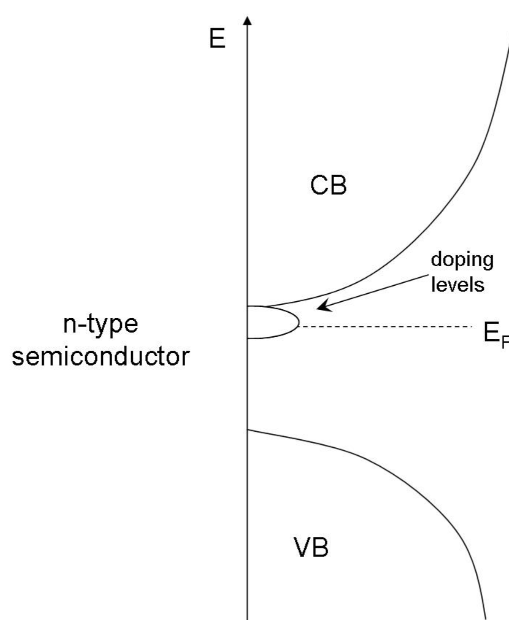

FIGURE 4.6. Schematic diagram of the proposed band bending occurring at the interface Hg/H-nSi (up) and Hg/H-pSi (down) junctions.

The expected barrier formation for which we performed IPE measurements was not found. This result seems to be a contradiction to what found, presented in the previous paragraph, from J/V characteristics. A barrier of $06 \div 07\ eV$ should be visible in the photocurrent spectrum coherently with the rectifying behavior of the $Hg/(CH_2)_{10}COOH/nSi(100)$ system. The possible explanation of this contradicting result is that the raising of the barrier is bias induced. IPE spectra are acquired with no bias to evaluate the effective barrier of the contact. The polarity character of the molecule (the acid group is strongly electronegative) can indeed play a role in the interface properties of such junctions.

Anyway even if the difference of onset values, visible in fig. 4.5 is very small and close to the experimental error, we are confident that the effect of lowering the photocurrent threshold is due to molecules. As it was shown from J/V characteristics (section 4.2) the junction properties (diode or ohmic behavior, barrier height) are modified by the presence of the alkyl acid at the interface.

Conclusion

The surface study of molecule modified Si surfaces displayed promising results from the point of view of the development of a "molecular electronic device".

- ✓ AFM and XPS has been used to characterize surface morphology and chemical composition of hydrogenated Si substrates and, consequently, of hybrid surfaces which was tested from electrochemistry measurements to be a a promising molecular switching device (VFC/Si and FCE/Si). Moreover syncrothron light spectromicroscopy experiments on VFC/Si confirmed the homogeneity of functionalized surfaces.
- ✓ The development of novel techniques such as Mercury drop soft contacts for electrical characterization of the hybrid (undecenoic acid functionalized Si surface) has allowed to extract information both on the stability and activity of such modified surfaces. Barrier height and ideality factor measurements has been extracted from current-voltage characteristics on $Hg/n-$ and $p-Si(100)$ and $Hg/(CH_2)_{10}COOH/n-Si(100)$ junctions, while photocurrent threshold has been measured by internal photoemission experiment.

The best results on the investigated hybrid systems where the local morphological ordering of the functionalized species together with the quality and stability of the modified surface; moreover the promising electrical behavior can lead to future utilizations of functionalized surfaces in micro/nano-electronics.

Bibliography

[1] Shockley, W.(1952). *A unipolar field-effect transistor* Proc. IRE 40, 1365.

[2] *Nanotechnology: Toward a Molecular Construction Kit*, *STT*, The Hague, (1998); A. J. Bard, *Integrated Chemical Systems: A Chemical Approach to Nanotecnology*, *Wiley*, New York, (1994)

[3] Campbell, S. A. Science and Engineering of Microelectronic Fabrication, Oxford University Press, Oxford, p. 536 (1996)

[4] Fujimasa, I. *Micromachines: A New Era in Mechanical Engineering*, Oxford University Press, Oxford, p. 156 (1996)

[5] L. Fabbrizzi, M. Licchelli, P. Pallavicini, *Acc. Chem. Res.*, 32 , 846 (1999)

[6] D. Cahen and G. Hodes, *Adv. Mater.* 14, 789 (2002)

[7] J. M. Buriak, *Chem. Rev.* 102, 5 (2002)

[8] Y. Selzer, A. Salomon and D. Cahen, *J. Phys. Chem. B* 106, 10432 (2002)

[9] K.M. Roth, A.A. Yasseri, Z. Liu, R.B. Dabke, V. Malinovskii, K.H. Schweikart, L. Yu, H. Tiznado, F. Zaera, J.S. Lindsey, W.G. Kuhr and D. F. Bocian, *J. Am. Chem. Soc.* 125, 505 (2003)

[10] M. R. Linford and C. E. D. Chidsey, *J. Am. Chem. Soc.* 115 (1993) 12631.

[11] L.J. Webb and N.S. Lewis, *J. Phys. Chem. B* 107, 5404 (2003)

[12] J. Cheng, D.B. Robinson, R.L. Cicero, T. Eberspacher, C.J. Barrelet and C.C. Chidsey, *J. Phys. Chem. B* 105, 10900 (2001)

[13] Z. Liu, A.A. Yasseri, J.S. Lindsey and D.F. Bocian, *Science* 302, 1543 (2003)

[14] Y.J. Liu and H.Z. Yu, *J. Phys. Chem. B* 107, 7803 (2003)

[15] N.P. Guisinger, M.E. Greene, R. Basu, A.S. Baluch and M.C. Hersam, *NanoLett.* 4, 55 (2004)

[16] C. Engtrakul and L.R. Sita, *NanoLett.* 1 (2001) 541

[17] Y.J. Liu and H.Z. Yu, *ChemPhysChem* 9, 799 (2002)

[18] a) E. P. Honig, *Thin Solid Films* 33, 231 (1976); b) B. Mann, H. Kuhn, *J. Appl. Phys.* 42, 4398 (1971)

[19] M.A. Rampi, G.M. Whitesides *Chemical Physics* 281, 373391 (2002)

[20] E. Laviron, *J. Electronal. Chem.* 101 19 (1979)

[21] W. Clauss, J. Zhang, D. J. Bergeron, and A. T. Johnson *J. Vac. Sci. Technol. B* 17(4), 1309 (1999)

[22] Binnig G., Rohrer H., Gerber Ch. and Weibel E. *Phys. Rev. Lett.*49 5760 (1982)

[23] Binnig G., Rohrer H., Gerber Ch. and Weibel E. (1982) *Appl.Phys. Lett.* 40 17880

[24] Binnig G., Rohrer H., Gerber Ch. and Weibel E. (1983) *Phys. Rev. Lett.* 50 1203

[25] Tersoff and Hamann 1985 *Phys. Rev. B* 31 80513

[26] Lang N.D. *Phys. Rev. Lett.* 55 230-3 (1985)

[27] Lucas A.A., Morawitz H., Henry G.R., Vigneron J.-G., Lambin Ph., Cutler P.H. and Feuchtwang T.E. *Phys. Rev. B* 37, 1070820 (1988)

[28] Noguera C. *Phys. Rev. B* 42, 162937 (1990)

[29] H.Hertz, *Ann. Physik* 31, 983 (1887)

[30] K.T. Compton, L.W. Ross, *Phys. Rev.* 13, 374 (1919)

[31] A.Sommerfeld, *Z.Physik* 47, 1 (1928)

[32] R.H. Fowler, *Phys. Rev.* 38, 45 (1931)

[33] E. Wigner, J. Bardeen, *Phys. Rev.* 48, 84 (1935); J. Bardeen, *Phys. Rev.* 49, 653 (1936)

[34] W.E. Spicer, R.E. Simon, *Phys. Rev. Lett.* 3, 385 (1962); W.E. Spicer, C.N. Berblung, *Phys. Rev. Lett.* 12, 9 (1964);

[35] K. Siegbahn et al., *ESCA Atomic, Molecular and Solid State Structure by Means of Electron Spectroscopy*, Nova Acta, Soc. Sci. Upsaliensis IV, 20 (1967)

[36] John B. Hudson *Surface Science*. Stoneham, MA: Butterworth-Heinemann (1992)

[37] B. Feuerbacher, B. Fitton, R.F. Willis, *Photoemission and Electron Properties of Surfaces* John Wiley & sons pag. 4-7 (1978)

[38] T. Koopmans, *Physica* 1, 104 (1933)

[39] M. R. Linford, P. Fenter, P. M. Eisemberg and C. E. D. Chidsey, *J. Am. Chem. Soc.* 117, 3145 (1995)

[40] M. P. Stewart, J. M. Buriak, *Angew. Chem. Int. Ed. Engl.* 23, 3257 (1998)

[41] J.M. Buriak , *Chem. Commun.*, 1051-1060 (1999)

[42] J.M. Buriak, *Chem. Rev.*, Vol. 102, n. 5 (2002)

[43] C. Henry de Villeneuve, J. Pinson, M.C. Bernard and P. Allongue, *J. Phys. Chem. B* 101, 2415 (1997)

[44] F. Cattaruzza, A. Cricenti, A. Flamini, M. Girasole, G. Longo, A. Mezzi and T. Prosperi *J. Mater. Chem.* 14 , 1461 (2004)

[45] P. Kruse, E. R. Johnson, G. A. DiLabio and R. A. Wolkow, *NanoLett.* 2, 807 (2002)

[46] E. A. Dalchiele, G. Bernardini, F. Cattaruzza, A. Flamini, P. Pallavicini, R. Zanoni and F. Decker, submitted

[47] D. Vuillaume, C. Boulas, J. Collet, J. V. Davidovits and F. Rondelez, *Appl. Phys. Lett.* 69, 1648 (1996)

[48] R. Boukherroub, S. Morin, F. Bensebaa and D.D.M. Wayner, *Langmuir* 15, 3831 (1999)

[49] F. Effenberger, G. Gotz, B. Bidlingmaier and M. Wezstein, *Angew. Chem.*, Int. Ed. 37, 2462 (1998)

[50] R.L. Cicero, M.R. Linford and C.E.D. Chidsey, *Langmuir* 16, 5688 (2000)

[51] Q.Y. Sun et al. *Angew. Chem. Int. Ed.* 43, 1352 (2004)

[52] F. Karadas, G. Ertas and S. Suzer, *J. Phys. Chem. B* 108, 1515 (2004)

[53] K. Hricovini, R. Gnther, P. Thiry, A. Taleb-Ibrahimi, G. Indlekofer, J.E. Bonnet, P. Dumas, Y. Petroff, X. Blase, X. Zhu, S.G. Louie, T.J. Chabal and P.A.Thiry, *Phys. Rev. Lett.* 70, 1992 (1993)

[54] R.I.G. Uhrberg, E. Landemark and Y.-C. Chao, *J. Electron Spectrosc. Relat. Phenom.* 75, 197 (1995)

[55] G.F. Cerofolini, C. Galati and L. Renna, *Surf. Interf. Anal.* 35, 968 (2003)

[56] *Practical surface Analysis* (II Ed.) Vol.1 edited by Briggs & Seah (1983)

[57] M.P. Seah and S.J. Spencer, *Surf. Interf. Anal.* 33, 640 (2002)

[58] D.O. Cowan and J. Park, *Chem. Comm.* 1444 (1971).

[59] C.M. Woodbridge, D.L. Pugmuir, R.C. Jonhson, N.M. Boag and M.A. Langell, *J. Phys. Chem.B* 104, 3085 (2000)

[60] (a) Rhoderich, E. H.; Williams, R. H. *Metal-Semiconductor Contacts*, 2nd ed.; Clarendon Press: Oxford, 1988. (b) Sze, S.M. *Physics of Semiconductor Devices*, 2nd ed.; John Wiley & Sons: New York, 1981.

[61] R.H. Fowler, Phys. Rev. 38, 45 (1931)

SUSC 15341 ARTICLE IN PRESS No. of Pages 13, DTD = 5.0.1
26 November 2004 Disk used

Available online at www.sciencedirect.com
SCIENCE DIRECT®
Surface Science xxx (2004) xxx–xxx
SURFACE SCIENCE
www.elsevier.com/locate/susc

2 # An AFM, XPS and electrochemical study of molecular
3 electroactive monolayers formed by wet chemistry
4 functionalization of H-terminated Si(1 0 0) with vinylferrocene

5 R. Zanoni [a,*], F. Cattaruzza [b], C. Coluzza [c], E.A. Dalchiele [d], F. Decker [a],
6 G. Di Santo [c], A. Flamini [b], L. Funari [a], A.G. Marrani [a]

7 [a] *Dipartimento di Chimica and INFM-RSF2, Università degli Studi di Roma "La Sapienza", piazzale Aldo Moro, 5-00185 Roma, Italy*
8 [b] *CNR-ISM, Area della Ricerca di Montelibretti, Monterotondo Stazione, C.P. 00016, Italy*
9 [c] *Dipartimento di Fisica and INFM-RSF2, Università degli Studi di Roma "La Sapienza", piazzale Aldo Moro, 5-00185 Roma, Italy*
10 [d] *Instituto de Física, Facultad de Ingeniería, Herrera y Reissig 565, C.C. 30, 11000 Montevideo, Uruguay*

Received 9 August 2004; accepted for publication 12 November 2004

13 **Abstract**

14 Molecular electroactive monolayers have been produced from vinylferrocene (VFC) via light-assisted surface
15 anchoring to H-terminated n- and p-Si(1 0 0) wafers prepared via wet chemistry, in a controlled atmosphere. The result-
16 ing Si–C bound hybrids have been characterized by means of XPS and AFM. Their performance as semiconductor
17 functionalized electrodes and their surface composition have been followed by combining electrochemical and XPS
18 measurements on the same samples, before and after use in an electrochemical cell. White-light photoactivated anchor-
19 ing at short (1 h) exposure times has resulted in a mild route, with a very limited impact on the initial quality of the
20 silicon substrate. In fact, the functionalized Si surface results negligibly oxidized, and the C/Fe atomic ratio is close
21 to the value expected for the pure molecular species. The VFC/Si hybrids can be described as $(\eta^5\text{-}C_5H_5)Fe^{2+}(\eta^5\text{-}$
22 $C_5H_4)$–CH_2–CH_2–Si species, on the basis of XPS results. Electrochemical methods have been applied in order to inves-
23 tigate the role played by a robust, covalent Si–C anchoring mode towards substrate-molecule electronic communica-
24 tion, a crucial issue for a perspective development of molecular electronics devices. The response found from cyclic
25 voltammograms for p-Si(1 0 0) functionalized electrodes, run in the dark and under illumination, has shown that the
26 electron transfer is not limited by the number of charge carriers, confirming the occurrence of electron transfer via
27 the Si valence band. The hybrids have shown a noticeable electrochemical stability and reversibility under cyclic vol-
28 tammetry (cv), and the trend in peak current intensity vs. the scan rate was linear. The molecule-Si bond is preserved
29 even after thousands of voltammetric cycles, although the surface coverage, evaluated from cv and XPS, decreases in
30 the same sequence. An increasingly larger surface concentration of Fe^{3+} at the expenses of Fe^{2+} redox centers has been

* Corresponding author. Tel.: +6 49913328; fax: +39 06 490324.
E-mail address: zanoni@uniroma1.it (R. Zanoni).

0039-6028/$ - see front matter © 2004 Published by Elsevier B.V.
doi:10.1016/j.susc.2004.11.023

UNCORRECTED PROOF

found at increasing number of cv's, experimentally associated with the growth of silicon oxide. Surface SiO^- groups from deprotonated silanol termination, induced by the electrochemical treatments, are proposed as the associated counterions for the Fe^{3+} species. They could be responsible for the observed decrease in the electron transfer rate constant with electrode ageing.
© 2004 Published by Elsevier B.V.

Keywords: Silicon; Single crystal surfaces; Surface chemical reaction; Chemisorption; Semiconducting surfaces; X-ray Photoelectron spectroscopy; Electrochemical methods; Atomic force microscopy

UNCORRECTED PROOF

1. Introduction

Several publications have addressed, in the last decade, the issue of organic derivatization of silicon surfaces, mainly in view of their potential applications in different fields, as molecular electronics, dielectric films, sensoring [1,2]. Basic issues of momentum importance are still open, notably the role played by the presence of a covalent bond, established between organic moiety and silicon, in determining the hybrid chemical behaviour, its electronic addressability and robustness [3,4]. A few recipes for a covalent molecular anchoring on silicon have been reported, sometimes associated with claims of a superior and long-term stability of the Si–C bond in hydrolytic conditions, which instead severely affects Si–O-R bonds [2,3,5–18]. The electronic communication between silicon substrate and attached molecules has also been tested, mainly by means of electrochemical methods in a solution [4,19–22] and, in a limited number of cases, in the solid state [23–26], and the importance of the nature of the contact has been discussed. However, it has not yet been clarified in the literature on Si-organics hybrids, if the roadmap to robust and reliable Si-based molecular electronics should select one among the existing Si-organics covalent bond already tested (mainly Si–C, Si–O, Si–P), or explore further ones. Part of the uncertainty could also come from a limited knowledge, from the point of view of surface science, of the resulting hybrids and of their reactivity in operating conditions. The heart of the hybrid being the peculiar molecular functionality, it has to be assessed if the molecular nature is maintained through use of the hybrid. In a wider view, it is crucial to assess the quality of the hybrid from the two sides: the molecule and the substrate, not only at the stage of as prepared species but also upon/after its use.

Some of these issues have been addressed here, by selecting a commercial molecule, vinylferrocene (VFC), as the starting material for the deposition of molecular electroactive monolayers, covalently anchored on the surface of H-terminated Si(1 0 0) through wet-chemistry methods. The electrochemical properties of free and anchored ferrocene and substituted ferrocenes have been deeply investigated in the last 50 years. More recently, ferrocenes have been proposed among the more suitable anchored electroactive species in molecular electronics, mainly because of the well-known advantages in terms of chemical and thermal stability, robustness and reversible cyclability of the ferrocene/ferrocenium redox couple, wide synthetic availability of substituted ferrocene analogues and tunability of the corresponding redox potential [4,27]. VFC on Si(1 0 0) is the object of a recent publication, where its reactivity as a gas-phase molecule on H–Si(1 0 0) (obtained by exposing a clean Si(1 0 0) surface produced in UHV to atomic H) has been explored by means of STM [28]. In this dry-chemistry experiment, a Si–C chemical anchoring through the vinyl group has been proposed to result from the reaction. High-resolution STM images have revealed widened linear arrangements of molecules, a few nm long, and it has been proposed that the cyclopentadienyl rings form a V-shaped sequence on Si, in order to reduce the repulsive molecular interaction. The anchoring mechanism proposed is a radical chain reaction, generated by the STM tip by H abstraction from a H–Si bond [6,28].

In the present paper, the main issues are: (1) A simple and reproducible wet-chemistry recipe is proposed for VFC/Si, which leads to the establish-

ment a robust Si–C surface-molecule bond, with negligible impact on the quality of the initial Si surface. (2) The extent of preservation of such a bond is investigated in operating conditions of strict interest for further implementation of Si-based molecular electronics. The substrate selected are the ones of choice in Si electronics, n- and p-doped Si(1 0 0), which have been hydrogenated via wet chemistry.

The first issue has been addressed by means of AFM and XPS, which have evidenced the surface morphology and composition, while the second has required to follow the redox behaviour of the hybrid species. While a full electrochemical study is being reported elsewhere [29], the presence of a true chemical attachment to the substrate, the hybrid stability as a function of extended redox cycles, and the redox kinetics of VFC/Si(1 0 0) are presented here, with the help of combined electrochemical and XPS measurements on the same samples.

2. Experimental

2.1. General

The functionalization experiments on the surface-activated samples were carried out in a N_2(g)-purged dry-box (Braun) or using standard preparative schlenk-line procedures. Single-side polished Si(1 0 0) wafers (Si-Mat), ~350 μm thick, p-doped (0.02 Ωcm resistivity) and n-doped (0.01 Ωcm resistivity) with approximate areas of 1 cm^2, were first washed in boiling 1,1,2-trichlorethane for 10 min and subsequently in methanol at room temperature, with sonication for 5 min. They were oxidized in $H_2O_2/HCl/H_2O$ (2:1:8) at 353 K for 15 min, rinsed copiously with de-ionized water, etched with 10% aqueous HF for 10 min, rinsed with water again, dried under a stream of N_2 and immediately used in the functionalization process, in a dry-box. Vinylferrocene was a Fluka pure product, used as received. Care has been taken in order to reduce all sources of O_2 and H_2O contamination in the preparation steps. The residual presence of ppm levels of O_2 and H_2O monitored by the dry-box sensor constitutes a possible source of oxidation for the silicon substrate.

2.2. Monolayer preparation on silicon

AH-terminated Si(1 0 0) wafer was placed in a levelled Petri dish in a dry-box, covered with VFC and subjected to a 35 mW/cm^2 visible irradiation for 1 h from a quartz-iodine lamp, while heated slightly above the melting point of VFC (⩾323 K). Several samples were prepared following the above route. Freshly etched Si samples were always used for the characterization measurements. After functionalization, all samples were subjected to the same cleaning procedure, consisting of four sonication cycles, 5 min each, with different solvents (CH_2Cl_2 and CH_3CN), and drying in a stream of N_2. It is noteworthy that prolonged exposure times to visible light have resulted in the development of a surface deposit visible by eyes, which could not be washed out even by extended rinsing and sonication, perhaps related to a polymerization reaction of the vinyl function. A systematic study of the effect of VFC/Si resistance to oxidation in air was outside the scope of the present paper. The resistance to oxidation was checked by XPS for samples stored in schlenk tubes under N_2 for different extent of times. This procedure has resulted in no sizeable effects in the XPS spectra within one week storage, and in a very limited increase in the relative intensity of the Si 2p component related to SiO_2 plus a negligible decrease in the Fe/Si(tot) ratio, as judged from XPS spectra taken after one month from the preparation and first XPS measurements.

2.3. AFM

A needle-sensor atomic force microscope (VT-AFM, Omicron NanoTechnology) was used, which is attached to a UHV chamber where XPS measurements were also run (see infra). The silicon nitride micro-fabricated tip had a nominal curvature radius <10 nm and a resonance frequency of 997,500 kHz. The values of average *z*-height and of root mean square (rms) roughness (defined as the standard deviation from the average *z*-height

UNCORRECTED PROOF

values), were determined by Scala Pro software (Omicron NanoTechnology).

2.4. X-ray photoelectron spectroscopy

XPS results have been obtained on a new experimental apparatus in UHV consisting of: a modified Omicron MXPS system, with a preparation chamber equipped with sample cleaning facilities and evaporative sources; an on-line analyzer chamber with a dual X-ray anode source (Omicron DAR 400) and an Omicron EA-125 energy analyzer; an Omicron VT-STM/AFM flange. Sample transfer between the various experimental areas is conducted by means of linear magnetic transfer rods or manipulators. All measurements have been conducted in the least possible time after sample preparation. Samples were produced and mounted on sample holders suitable for XPS in a dry-box, and transferred from the dry-box to the XPS facility in schlenk tubes, under N_2. Samples subjected to electrochemical treatments have been transferred from the dry-box to the XPS machine by schlenk tubes, shortly before the electrochemical tests. The process has required exposing the samples to air for few seconds, the time required for placing the sample on the transfer probe in the fast entry-lock chamber of the spectrometer. No sizeable sign of sample degradation under extended acquisition times under the X-rays was observed for the samples. The experimental conditions adopted were MgKα photons ($h\nu = 1253.6$ eV), generated operating the anode at 14–15 kV, 10–20 mA. No charging was experienced by the hybrid species, as can be inferred from the Si 2p peak position, collected in Table 1, coincident with literature reports, which assign a value of 99.7 eV to the Si $2p_{3/2}$ bulk component [30]. The experimental

Table 1
Results from XPS measurements

Sample	SiO_2 overlayer thickness (nm)	Atomic ratios					Fe $2p_{3/2}$ BE (a) Fe(II) (b) Fe(III)
		Fe/Si	Fe(II)/Fe(III)	C/Fe	C/Si	O/Si	
H-terminated n-Si(100)	–	–	–	–	0.14	0.059	–
H-terminated p-Si(100)	–	–	–	–	0.27	0.11	–
VFC/n-Si(100)	0.13	0.06	2.20	11.8	0.64	0.31	(a) 708.5 (b) 711.1
VFC/n-Si(100), after cv	0.70	0.035	0.97	26.7	0.93	0.73	(a) 708.5 (b) 711.1
VFC/p-Si(100) (sample 1)	0.25	0.06	2.09	11.3	0.67	0.33	(a) 708.7 (b) 711.3
Sample 1, after 1 min at +1 V bias	1.03	0.02	1.98	49.0	1.1	0.73	(a) 708.6 (b) 711.2
Sample 1, after 2 min at +1 V bias	1.12	0.02	1.97	61.5	1.3	0.88	(a) 708.6 (b) 711.2
VFC/p-Si(100) (sample 2)	0.37	0.035	2.31	15.9	0.53	0.35	(a) 708.6 (b) 711.2
Sample 2, after first cv sequence	0.92	0.03	1.09	31.2	0.87	0.79	(a) 708.7 (b) 711.4
Sample 2, after second cv sequence	1.64	0.02	0.67	65.6	1.1	0.84	(a) 708.6 (b) 711.3

Values for silica overlayer thickness (nm), obtained from application of an XPS quantitative model [31,44,45]. Relative atomic ratios for the reported samples, measured from XPS relative intensity ratios, after normalization to atomic cross-sections and for a square root dependence of the photoelectron kinetic energy. Fe $2p_{3/2}$ binding energies (eV) for the Fe(II) and Fe(III) main components. VFC/p-Si(100) samples (1) and (2) have been obtained with the same initial procedure and subjected to different electrochemical treatments, as specified in the table.

UNCORRECTED PROOF

uncertainty associated with the XPS measurements is within ±0.2 eV. Based on a comparison on about 10 samples, the Si Auger parameter values for hydrogenated n- and p-Si samples were found coincident within ±0.1 eV. A common reference has then been chosen for the binding energy scale in both n- and p-Si samples, by assigning the value of 99.7 eV to Si $2p_{3/2}$ bulk-related component. In VFC/n- or p-Si samples, the energy distance between Fe $2p_{3/2}$ (Fe^{2+} component) and Si $2p_{3/2}$ (bulk component) was found to be constant, within the experimental uncertainty. Therefore, the different band bending for n- and p-Si functionalized samples does not affect the assignments reported. In order to produce a satisfactory result, the energy region of bulk Si and SiH_x-related peaks has been fitted with three 2p doublets, one for the main component, related to the bulk, and two additional spin-orbit split components, at both sides of the bulk feature. The values for the energy positions were left free to vary independently, while the 3/2 and 1/2 spin-orbit split Si 2p components had a common value of FWHM and of Lorentzian-Gaussian mix, optimized by the fit, and the intensity ratio was fixed to the expected 2:1 branching ratio. The effects on quantitative analysis possibly generated by XPS measurements from oriented Si wafers because of photoelectron diffraction at preferential directions of electron collection [31], were minimized in the comparison, by mounting the Si(100) wafers always with the same orientation with respect to the analyzer axis.

2.5. Electrochemical measurements

After monolayer formation, ohmic contact was made to the back of the derivatized Si samples by scratching the Si surface, rubbing it with Ga–In eutectic and attaching a copper contact to it. The electrode set-up was obtained by pressing the Si crystal against an O-ring sealing a small aperture in the PTFE cell. At the opposite side of the cell, a flat glass window allowed for illumination of the silicon electrode by a laser light. The O-ring defined exactly the electrode area (0.3 cm^2). The electrochemical properties of the monolayers covalently bound to n- and p-Si(100) surfaces were explored by cyclic voltammetry in 0.1 M NEt_4ClO_4 (tetraethylammonium perchlorate, TEAP) in dry CH_3CN. The electrolyte solution contained no deliberately added electroactive species. All electrochemical measurements were performed inside a dry-box with a three electrode cell, using an AUTOLAB 12 potentiostat-galvanostat. The counter-electrode was a platinum coil wire, and a silver wire immersed in 0.01 M $AgNO_3$ in acetonitrile, separated from the main solution by a porous fritted glass + agar plug, served as reference electrode. During cyclic voltammetries under illumination, a red semiconductor laser (5 mW, 670 nm) was used. The cyclic voltammograms have been corrected for IR drop.

3. Results and discussion

It is widely accepted in the literature that Si surface functionalization performed with a vinyl insaturation as the molecular anchoring group, can lead to the establishment of a Si–C bond, provided that the conditions are met for a hydrosilylation reaction to take place between a surface Si–H bond and the vinyl group of the molecule [2]. In the case of VFC, which is a solid with a low melting T (323 K), hydrosilylation can be obtained by formation of Si radicals through Si–H homolysis, activated via UV- or visible-light exposure, or by heating. Alternative, more elaborate methods have been proposed for alkenes, as halogenation of the surface [8], thermal reaction of Grignard compounds [15], activation of the surface by radicals [6], electrochemistry [11,32]. In the present study, an effort has been made to explore a simple, reproducible and mild anchoring route, which implies, i.e., to expose the H-terminated Si(100) surface only to one chemical during the delicate phase of anchoring. VFC photoimmobilization has been obtained by contacting the Si wafer, kept slightly above the VFC melting T, with the pure substance under visible light [13,15,16,33–39], for 1 h, followed by extensive rinsing (see Section 2). This is a modified procedure with respect to the visible-light assisted reactions reported in Ref. [34] for vinyl- and ethynil-containing organics, where 0.1 M mesitilene solutions of the unsaturated molecules

UNCORRECTED PROOF

have been contacted with Si for 15 h. Considering that Si–H homolysis requires UV light [2], a mechanism has been proposed, originally for white-light activation of photoluminescent nanocrystalline silicon [2], and more recently extended to Si wafers [34]. The mechanism implies that photogenerated holes, produced in the silicon substrate, are subsequently attacked by a nucleophile, as a C=C bond. In partial support to this hypothesis, it has been reported that more densely packed monolayers of a variety of 1-alkenes, 1-alkynes and esterified-1-alkenes can be obtained, with the same process, on low-doped hydrogenated n- or p-Si(100) with respect to highly-doped p-Si, in line with the effects of the dopant on the band bending [34]. While it can be hypothesized that such a mechanism is operating in the present experiment, it is due to mention that thermal promotion can be also active, since vinyl-aromatic substrates covalently anchor on Si to an appreciable extent (~10%) even at RT in the dark, as reported, i.e., for styrene on Si(111) [16]. In agreement with the previous findings commented above [34], no significant difference has been noticed in the extent of functionalization obtained for the present samples (as deduced from Fe/Si XPS atomic ratios, see infra) for VFC on n- or p-Si(100), with closely comparable high doping levels of the substrates. A large number of VFC/Si(100) samples have been produced along the procedure reported above and, in the following, the ensemble of experimental characterization is reviewed and commented.

3.1. AFM

AFM images taken on freshly prepared H-terminated n- and p-Si(100) samples (Fig. 1(a) and (b), respectively) and their associated linear cross-section profiles [Fig. 1(c) and (d), respectively] show that both surfaces are flat over large (0.5×0.5 μm^2) fields of view. The corresponding values of rms roughness are 0.05 and 0.06 nm. In Fig. 1(e), a 250×250 nm^2 image from a freshly prepared sample of VFC/p-Si(100) is shown, representative of the total area explored (5×10^5 nm^2). Structures like elongated grains are visible, 15×30 nm^2 wide in the average, uniformly distributed in the whole region, without a long-range order. The rms roughness is 0.17 nm, a small value, compatible with a monolayer (or a submonolayer) deposition, when compared with the roughness of the H–Si(100) substrate. Close-up views (100×100 nm^2) and linear cross-section profiles analysis (Fig. 1(f) and (h)) show finer details of the cluster formations. The average z-value of the grains has been determined by a statistical analysis from 54 height values, obtained from several cross-section profiles from the entire explored range of 5×10^5 nm^2. A Gaussian fit of their height values (Fig. 1(g)), taken from the entire explored area, gives a narrow distribution, peaked at 0.45 nm, with a standard deviation of 0.15 nm, and a lateral spacing among structures in the 10–20 nm range. The obtained value of height is close to the diameter of a cyclopentadyenil ring (~0.39 nm), and compatible with the distance between two cyclopentadyenil ligands in ferrocene (~0.33 nm). The standard deviation of the Gaussian fit and of the rms roughness derived from large frame images closely compare (0.15 vs. 0.17 nm), and strengthen the results of the local statistical fit. Taken together, the AFM results from wet-chemistry functionalization of VFC/H–Si(100) samples have revealed a surface morphology of the deposits compatible with the preferential molecular self-assembling in rows revealed by high-resolution STM images, reported for analogue samples obtained from gas-phase treatments [28].

3.2. XPS

3.2.1. Hydrogenated Si surfaces

A typical Si 2p XPS spectrum from a freshly prepared H-terminated n-Si(100) is reported in Fig. 2(a), where the SiO_2 component is clearly visible as a feature separated from the bulk by 3.5–4 eV, the shift depending on the oxide thickness [40]. As for the hydride terminations, the Si 2p chemical shifts with respect to the bulk component have been previously reported as 0.2–0.3 (Si monohydride termination) and ~0.35–0.6 eV (dihydride analogous), the uncertainty being related mainly to the low intensity of the components [41–43]. The presence of chemically shifted Si 2p components, in addition to a variable amount of SiO_2, can be unambiguously inferred from inspection

UNCORRECTED PROOF

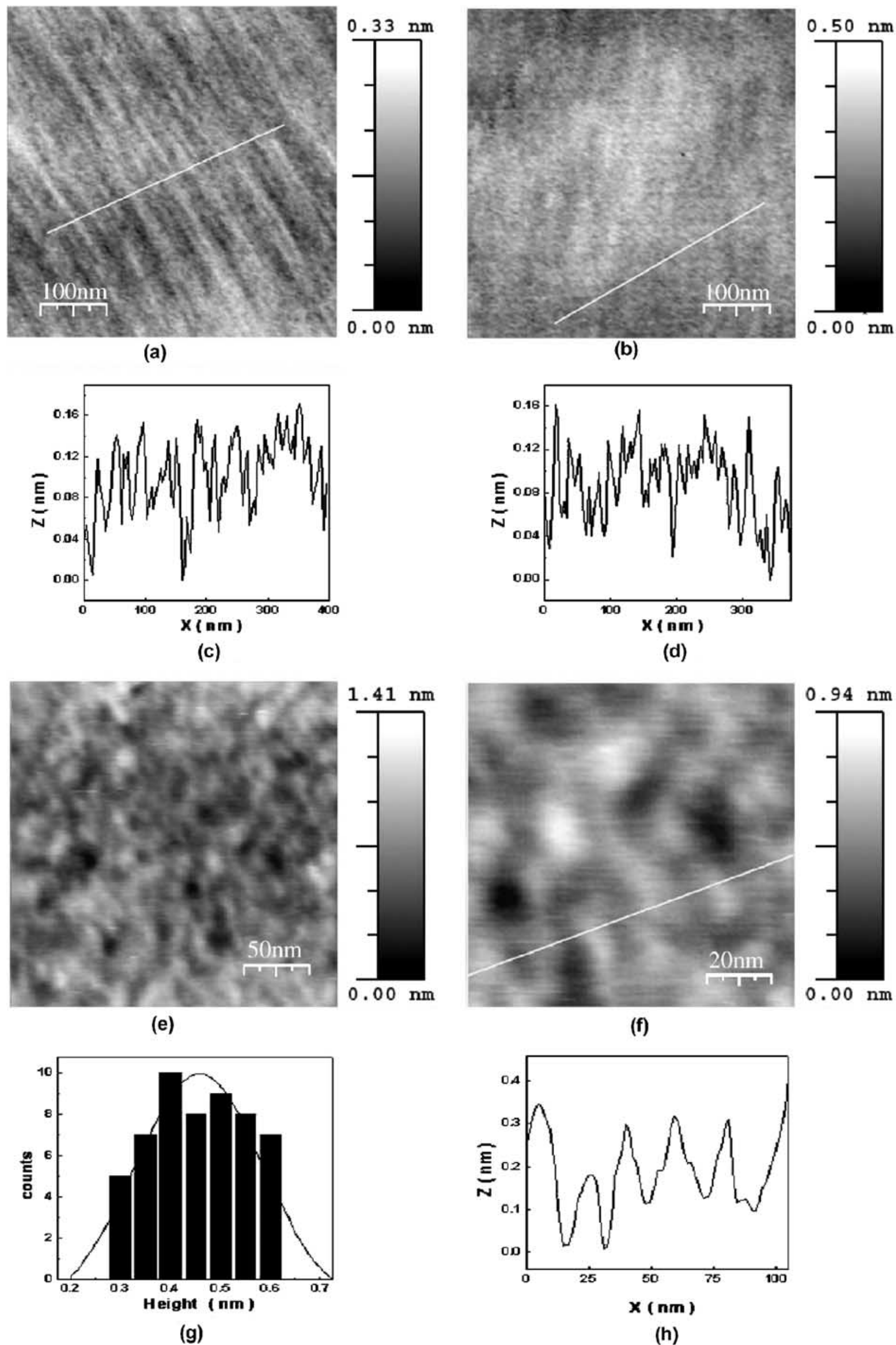

Fig. 1. 500×500 nm^2 AFM images from clean n-Si(1 0 0)-H (a) and p-Si(1 0 0)-H (b) substrates. Corresponding linear cross-section profiles analysis (c, d) taken along the marked segments. The measured rms roughness values are 0.06 and 0.05 nm, respectively. A 250×250 nm^2 AFM image from a freshly prepared sample of VFC/p-Si(1 0 0) (e); close-up view (100×100 nm^2) (f) and linear cross-section profiles (h), from the same area; Gaussian distribution analysis of the heights taken from an overall 5×10^5 nm^2 area of a freshly prepared sample of VFC/p-Si(1 0 0) (g).

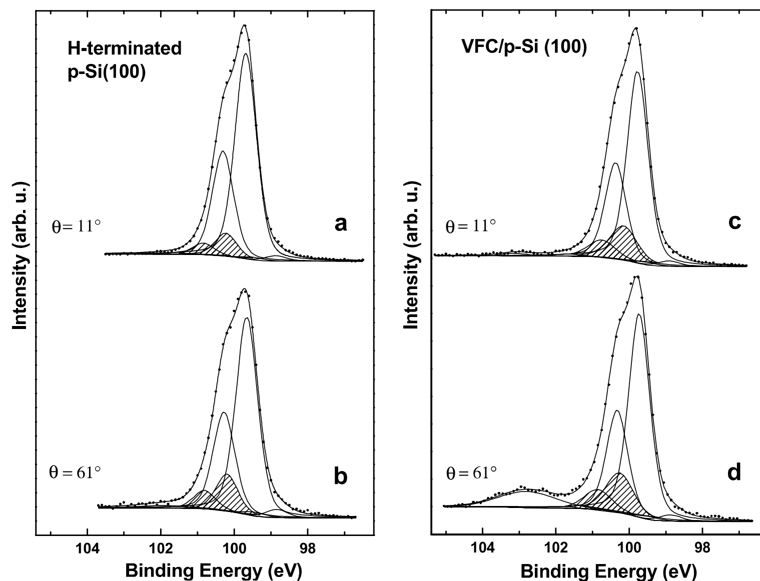

Fig. 2. Si 2p XPS spectra from freshly prepared samples respectively of: H-terminated p-Si(1 0 0) (left) and VFC/p-Si(1 0 0) (right). The spectra have been taken with non-monochromatized MgKα photons at a pass energy of 10 eV. The results of the curve-fitting procedure applied at two different photoelectrons collection angles, measured from the normal to the surface, are reported: (Top) 11°; (Bottom) 61°. The areas corresponding to silicon hydride peak components are hatched.

of Fig. 2(left). A satisfactory fit was reached with the two minor components located at −0.7 and +0.55 eV and the SiO_2 characteristic feature at +3.5 eV, all referred to the bulk (see Section 2 for details). The two latter values closely reproduce previous reports on H–Si. In the case of H-terminated Si(1 0 0), the presence of an additional component on the low-binding energy side has been reported in the literature at −0.25 to −0.3 eV, and related essentially to a surface correction to bulk silicon [43]. In a clean Si(1 0 0) reconstructed surface, the low BE region is dominated by the dimer-up subset of Si atoms, which has been located at ∼−0.5 eV from Si(0) [42]. In the present case, the negative shift is substantially larger than previously reported for the clean reconstructed Si(1 0 0) surface. Given the present limited resolution, we speculate that the negatively shifted component could be the assigned to an unsaturated Si atom bound to a positively shifted Si atom, as in SiH_2 (or even in Si–F or Si–O). It is noticeable (and not contradictory) that a residual intensity at this energy position was found also after functionalization with VFC, since the functionalization process can generate hydrogen abstraction.

The quality of the H-terminated Si wafers has been tested by determining the presence and extent of Si–O components in the Si 2p ionization region (Fig. 2(left) and Table 1). The results related to the thickness of a silica overlayer, collected in Table 1, have been obtained from application of the already reported quantitative model for a silica layer grown on oriented Si surfaces [30,44,45], which leads to the following equation:

$$d_{ox} = L_{SiO_2}(E_{Si}) \cos\theta \ln(1 + R_{exp}/R_o) \qquad (1)$$

where d_{ox} is the total oxide thickness (nm) due to the four different Si_xO_y species, $L_{SiO_2}(E_{Si})$ is the attenuation length of 2p photoelectrons from SiO_2, θ is the photoelectrons collection angle taken from the surface normal, R_{exp} is the measured $I_{silica}/I_{silicon}$ ratio and R_o is the $I_{silica}/I_{silicon}$ ratio for the pure species. The product $L_{SiO_2}(E_{Si}) \cos\theta$ is the inelastic mean free paths of Si 2p photoelectrons.

The total oxide thickness coming from application of Eq. (1) is a quantitative estimate of a con-

UNCORRECTED PROOF

467 tinuous overlayer. One monolayer of silica grown
468 on silicon is 0.35 nm thick [45]. The obvious impli-
469 cation of the very small values displayed in the
470 case of freshly prepared VFC/Si samples is that
471 the photochemical anchoring here adopted pro-
472 duces a surface well passivated by the attached
473 molecules and by Si–H residual bonds, with a sur-
474 face oxidation limited to very small areas.

475 *3.2.2. Functionalized Si surfaces*

476 XPS was further used to characterize the pres-
477 ence, abundance and chemical state of the ferrocene
478 derivatives, after anchoring. Direct assessment of
479 the presence of a Si–C bond as a separate compo-
480 nent in the Si 2p peak is routinely obtained when
481 the substrate is clean Si, while in hydrogenated Si,
482 mono- and dihydride components fall the same
483 binding energy range [41–43]. From inspection of
484 the Si 2p complex peak, reported in Fig. 2(right),
485 the presence of a component related to both Si–H
486 and Si–C bonds (from 0.4 to 0.5 eV associated shift
487 from the bulk), is confirmed. Si unsaturated states,
488 reported above for the H–Si(1 0 0) samples, have
489 been experimentally determined also after function-
490 alization, by the peak component at low binding en-
491 ergy. The presence of this component calls for a
492 limited electronic passivation of silicon. In the pho-
493 toemission region of C 1s, a confident localization
494 of a C–Si bond feature is hampered by the unfa-
495 vourable ratio of the corresponding carbon atoms
496 with respect to the saturated and unsaturated car-
497 bons belonging to the molecule (expected at 1–1.5
498 eV higher BE). BE positions of Fe $2p_{3/2}$ compo-
499 nents and atomic ratios among characteristic ele-
500 ments, deduced from relative peak intensities, are
501 collected in Table 1 for selected samples. For about
502 70% of the VFC/Si samples freshly prepared, the
503 Fe/Si and the C/Fe atomic ratio were 0.06 and 12,
504 respectively, while in the remaining cases some
505 additional surface contamination reduced the first
506 value and increased the latter. A value of 12 for
507 the C/Fe equals the expected VFC stoichiometry
508 and calls for the preservation of the molecular nat-
509 ure of VFC/Si. In all the investigated samples, Fe
510 species in both (II) and (III) oxidation states have
511 been found, the Fe(II) being largely predominant
512 in the initially prepared ones. Curve fitting of the
513 complex Fe 2p peak envelopes has been applied,
514 in order to separate Fe(II) and Fe(III) data sets.
515 The corresponding BE and FWHM values repro-
516 duce literature findings for pure and surface-re-
517 acted ferrocene and ferrocenium salts, respectively
518 [30,46]. The narrow FWHM of Fe(II) spectra for
519 VFC/n-Si(1 0 0) favours an assignment to a well-de-
520 fined surface species. As for the Fe(III) species, a
521 possible assignment to Fe_2O_3, which has been
522 sometimes reported in surface-anchored ferrocenes
523 [47], can be confidently excluded on the basis of the
524 main peak-to-satellite Fe $2p_{3/2}$ energy separation
525 and of the relative intensity of Fe $2p_{3/2}$ satellite to
526 main lines in Fe_2O_3 [46]. The relevant core peaks
527 have been also taken at different photoelectron col-
528 lection angles, measured from the surface normal.
529 The Fe(II)/Fe(III) atomic ratios, determined from
530 the corresponding intensity of the Fe $2p_{3/2}$ compo-
531 nent at 11° and 61°, are strictly comparable, as
532 clearly visible in Fig. 3. The limited difference found
533 do not present a definite trend for n- and p-Si, and
534 fall within the associated experimental uncertainty
535 (±10%). In the same sequence, the more noticeable
536 effect observed has been the increase in intensity of
537 the C 1s feature, which represents the topmost ele-
538 ment, being about half of the Fe, Si, C, O atomic
539 composition at grazing angle. The lack of a surface
540 enrichment in one of the Fe components, while
541 excluding local phenomena as the formation of
542 ferrocenium over silica, can be taken as a further di-

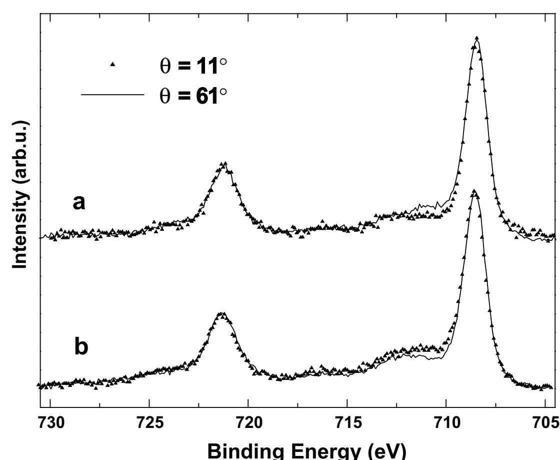

Fig. 3. Fe $2p_{3/2,1/2}$ XPS spectra from VFC/n- (a) and p-Si(1 0 0)-H (b) surfaces, taken at 11° and 61° photoelectrons collection angles, measured from the normal to the surface.

543 rect evidence for the proposed assignment of Fe(II)
544 and Fe(III) species to substituted ferrocene and
545 ferrocenium both directly bound to silicon.
546 In the n-doped samples a large band bending is
547 indeed present. In fact, in the dark there is no sig-
548 nal and only under light it is possible to inject
549 charges into VFC.

550 4. Electrochemical measurements

551 Representative cyclic voltammograms (cv) for
552 VFC/p-Si(1 0 0) are shown in Fig. 4(a). The electro-
553 lyte solution contained no deliberately added elect-

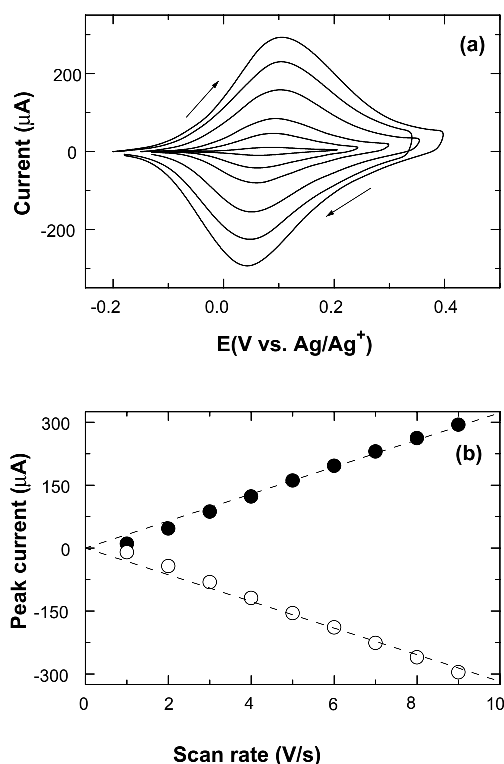

Fig. 4. (a) Representative cyclic voltammograms of a VFC/p-Si(1 0 0) functionalized electrode in 0.1 M TEAP/CH_3CN, as a function of the potential scan rate. The scan rates are 1, 2, 3, 5, 7 and 9 V/s, from smallest to largest amplitude. Geometrical electrode area = 0.3 cm^2. Experiments were done in darkness conditions. (b) Anodic (●) and cathodic (○) peak currents as a function of cyclic voltammetry scan rate, obtained from Fig. 4a. Dashed lines correspond to linear fittings, with correlation coefficients of 0.9999.

roactive species, and the voltammetric peaks can 554
be unambiguously attributed to the attached redox 555
species. The electrode potential was scanned from 556
the lower to the higher limit and back, at scan rates 557
varying from 1 to 9 V/s, inducing the reversible 558
oxidation of the ferrocene derivative group. The 559
cv's were run in the dark and under laser light, 560
and no difference was found in VFC/p-Si. On the 561
contrary, a huge photoeffect was found in VFC/ 562
n-Si, for which the redox reaction was controlled 563
by the photon flux used to generate electron-hole 564
pairs. The experimental obtainment of the same 565
cv curve for p-Si in the dark and under light indi- 566
cates that in this semiconductor, the electron 567
transfer is not limited by the number of charge car- 568
riers, and that it occurs via the valence band. 569

The scan rate dependence of cv was further ana- 570
lyzed. As can be inferred from inspection of Fig. 571
4(b), the anodic and cathodic peak currents were 572
found to scale linearly with the scan rate v rather 573
than with $v^{1/2}$, indicating a surface redox process. 574
Furthermore, this trend is characteristic of a 575
reversible (Nernstian) electrochemical process, 576
wherein the relative activity of the ferrocene and 577
ferrocenium sites is uniform throughout the film 578
and at equilibrium with each applied electrode po- 579
tential [48,49]. According to such an electroactive 580
species confinement at the Si electrode surface, dif- 581
fusion plays no role in current control. Peak cur- 582
rents are then directly proportional to the scan 583
rate, as is given by [50]. 584

$$I_{\text{peak}} = n^2F^2vA\Gamma(4RT)^{-1} \quad (2)$$

where n is the number of electrons, F is the Fara- 588
day constant, v is the scan rate (V/s), A is the elec- 589
trode surface area (cm^2), Γ is the surface coverage 590
in moles of attached molecules per unit surface 591
area, R and T have their usual meanings. 592

The surface coverage of the covalently attached 593
molecules can be determined by either using the 594
scan-rate dependence of the anodic and cathodic 595
peak currents via the above equation, or directly 596
integrating the voltammetric waves. The first pro- 597
cedure yields surface coverage values of 598
1.0×10^{-10} mol cm^{-2} for the VFC/p-Si(1 0 0) mon- 599
olayers, taking for A the geometric area of the elec- 600
trode. Such values are slightly lower than the 601
results obtained by integrating the voltammo- 602

UNCORRECTED PROOF

UNCORRECTED PROOF

grams, because the values based on peak currents may be affected by broadening of the voltammetric peaks.

The values of the cathodic peak widths at half-maximum, ΔE_{FWHM}, vary from 200 to 265 mV for potential scan rates from 1 to 9 V/s, larger than the theoretical (entropically determined) value of 91 mV, expected for identical, independent sites at room temperature [50]. Therefore, the broadness of the cv waves hint at a substantial repulsive interactions between nearest neighboring ferrocenyl groups on the surface [51]. Evidence for broadened cyclic voltammetric peaks ($\Delta E_{FWHM} \sim 140$–350 mV) have been reported in the literature for different FC-derivatives groups attached to Si [4,51].

Note in Fig. 4(a) that the difference between the peak potential of the anodic and cathodic peaks, ΔE_{pp}, increases with the scan rate. These values differ from the zero (and independent of scan rate) peak-to-peak separation theoretically predicted for an ideal surface-confined redox couple [52]. The increase in peak splitting indicates that the scan rate becomes comparable to the electron transfer rate at higher sweep speeds. ΔE_{pp} was found to scale linearly with $\ln v$ at high scan rates. From the peak-to-peak separation values in these cv's, the standard electron transfer rate constants, k_o, were obtained, according to Laviron's approach for the reaction of electroactive species immobilized onto an electrode surface [52]. The k_o values found from such analysis of the redox reaction were 10^2 s^{-1}.

In spite of the fact that the voltammetric waves for p-Si(100)/VFC were quite persistent to repeated oxidation-reduction reaction (over 1000 cycles), the ΔE_{pp} increases with the number of redox cycles performed, suggesting a progressive departure from reaction reversibility. At the same time, also the redox capacitance of the monolayers drops with ageing [29]. Both results indicate that the electron transfer rate constant decreases with electrode ageing, and this has been interpreted as due to the hindrance to the motion of the counterions by the growing Si oxide layer. The role of counterions in transporting electronic charge in redox-active assemblies is, in fact, widely recognized [53,54]. The interaction of the Fe^{3+} moiety with O^- sites from deprotonated silanol termination, induced on the Si surface by the electrochemical treatments, may considerably reduce the ion-pairing capability of the electrolyte anions with immobilized ferrocenium, therefore reducing the electron transfer kinetics. These results demonstrate that silicon surfaces modified with VFC, even without suffering substantial loss of electroactive material from the electrode, usually evolve with time, according to the chemical reactions taking place at those surface sites that have not been adequately protected from the formation of silica by the presence of the attached organic molecules.

4.1. Effects of electrochemical ageing on the surface composition

Electrochemical ageing of VFC/Si has been conducted on two samples along distinct procedures, and the respective behaviours have been related to their actual surface composition (Table 1). Sample (1) has been biased at +1 V, in order to force Si oxidation, and checked by XPS and cv, after application of each of the two anodic polarizations. Sample (2) has been subjected to a few thousands cv cycles, with an upper potential limit never exceeding 0.5 V (Fig. 4). A relative increase of SiO_2/Si ratio for both samples can be clearly seen from the data in Table 1. The Fe(II)/Fe(III) atomic ratio, on the contrary, has decreased only after repeated cycling. The growth of the Fe(III) component in the Fe 2p core line is clearly seen in Fig. 5. The reduction of the Fe/Si ratio, invariably observed after ageing, has been interpreted in terms of surface detachment of ferrocene molecules, as independently tested by the determination of the coverage values, from cv curves. It is noticeable that only after repeated cycling a close correlation can be drawn between the decrease in the Fe(II)/Fe(III) atomic ratio and in the coverage values. From XPS data analysis of the Fe 2p core line, Fe(III) can be assigned to ferrocenium ions, without signs of decomposition to iron oxide(s). The presence of ferrocenium could be originated in a substrate-assisted redox process, and the overall +1 charge of the surface complex could be neutralized by surface O^- groups. This is consistent with the absence of other anionic species, revealed by

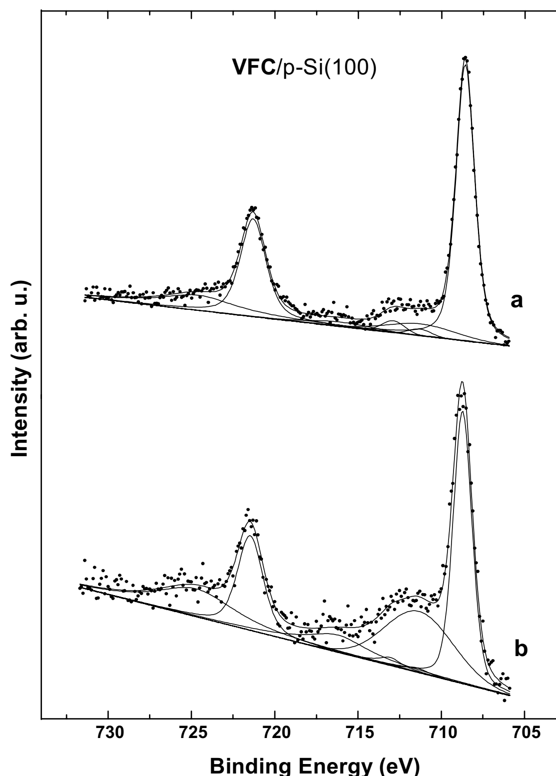

Fig. 5. Si 2p XPS spectra from a VFC/p-Si(1 0 0) sample, taken with non-monochromatized MgKα photons. (a) As prepared samples; (b) after 10^4 voltammetry cycles, performed at 5 V s^{-1} in 0.1 M TEAP in dry CH_3CN, in a voltage range −0.2 to 0.5 V.

697 XPS, and with the partial irreversibility of Fe^{2+} 698 oxidation, selectively found for the anodically 699 polarized sample.

700 5. Conclusions

701 White-light photoactivated anchoring of VFC 702 has produced redox-functionalized Si(1 0 0) surfaces 703 negligibly oxidized, with the C/Fe atomic ratio close 704 to the value expected for the pure molecular species. 705 On the basis of XPS results, the VFC/Si hybrids 706 can be described as $(\eta^5\text{-}C_5H_5)Fe^{2+}(\eta^5\text{-}C_5H_4)$– 707 CH_2–CH_2–Si species. The hybrids have shown a 708 noticeable stability at high number of redox cycles, 709 reversibility and linearity of the current intensity 710 with the scan rate. The response found in the dark 711 and under illumination for p-Si(1 0 0) functionalized electrodes has shown that the electron transfer is 712 not limited by the number of charge carriers, con- 713 firming the occurrence of electron transfer via the 714 Si valence band. The molecule-Si bond is preserved 715 even after thousands of voltammetric cycles, 716 although the surface coverage, evaluated from cv 717 and from XPS, decreases in the same sequence. 718 Some of the known advantages [27] of a ferrocene- 719 based approach to the formation of electroactive 720 molecular monolayers have been explored in the 721 present investigation, notably the robustness of 722 the ferrocene/ferrocenium redox couple and its 723 reversible cyclability. However, some limitations 724 connected to its use for the development of molecu- 725 lar-based charge-storage devices have been evi- 726 denced. In fact, an increasingly larger surface 727 concentration of Fe^{3+} at the expenses of Fe^{2+} redox 728 centers has been found at increasing number of cv's, 729 experimentally associated with the growth of silicon 730 oxide. The results demonstrate that silicon surfaces 731 modified with VFC, even without suffering substan- 732 tial loss of electroactive material from the electrode, 733 usually evolve with time, according to the chemical 734 reactions taking place at those surface sites that 735 have not been adequately protected from the forma- 736 tion of silica by the presence of the attached organic 737 molecules. 738

Acknowledgments 739

The work has been supported by MIUR (Min- 740 istero dell'Istruzione, Università e Ricerca) 741 through COFIN 2003 National Program, and by 742 Università degli Studi di Roma ''La Sapienza''. 743 One of us (E.A.D.) carried out this work with 744 the support of the ICTP Programme for Research 745 and Training in Italian Laboratories (Associate 746 Member), Trieste, Italy, which is kindly 747 acknowledged. 748

References 749

[1] D. Cahen, G. Hodes, Adv. Mater. 14 (2002) 789. 750
[2] J.M. Buriak, Chem. Rev. 102 (2002) 5. 751
[3] Y. Selzer, A. Salomon, D. Cahen, J. Phys. Chem. B 106 (2002) 10432. 752 753

UNCORRECTED PROOF

[4] K.M. Roth, A.A. Yasseri, Z. Liu, R.B. Dabke, V. Malinovskii, K.-H. Schweikart, L. Yu, H. Tiznado, F. Zaera, J.S. Lindsey, W.G. Kuhr, D.F. Bocian, J. Am. Chem. Soc. 125 (2003) 505.
[5] M.R. Linford, C.E.D. Chidsey, J. Am. Chem. Soc. 115 (1993) 12631.
[6] M.R. Linford, P. Fenter, P.M. Eisemberg, C.E.D. Chidsey, J. Am. Chem. Soc. 117 (1995) 3145.
[7] G. Cleland, B.R. Horrocks, A. Houlton, J. Chem. Soc. Faraday Trans. 91 (1995) 4001.
[8] A. Bansal, X.L. Li, I. Lauermann, N.S. Lewis, S.I. Yi, W.H. Weinberg, J. Am. Chem. Soc. 118 (1996) 7225.
[9] D. Vuillaume, C. Boulas, J. Collet, J.V. Davidovits, F. Rondelez, Appl. Phys. Lett. 69 (1996) 1648.
[10] A. Teyssot, A. Fidélis, S. Fellah, F. Ozanam, J.-N. Chazalviel, Electrochim. Acta 47 (2002) 2565.
[11] C. Henry de Villeneuve, J. Pinson, M.C. Bernard, P. Allongue, J. Phys. Chem. B 101 (1997) 2415.
[12] A.B. Sieval, A.L. Demirel, J.W.M. Nissink, M.R. Linford, J.H. van der Maas, W.H. de Jeu, H. Zuilhof, E.J.R. Sudhölter, Langmuir 14 (1998) 1759.
[13] F. Effenberger, G. Gotz, B. Bidlingmaier, M. Wezstein, Angew. Chem., Int. Ed. 37 (1998) 2462.
[14] J.M. Buriak, Chem. Commun. 1051 (1999).
[15] R. Boukherroub, S. Morin, F. Bensebaa, D.D.M. Wayner, Langmuir 15 (1999) 3831.
[16] R.L. Cicero, M.R. Linford, C.E.D. Chidsey, Langmuir 16 (2000) 5688.
[17] T. Okubo, H. Tsuchiya, M. Sadakata, T. Yasuda, K. Tanaka, Appl. Surf. Sci. 171 (2001) 252.
[18] L.J. Webb, N.S. Lewis, J. Phys. Chem. B 107 (2003) 5404.
[19] J. Cheng, D.B. Robinson, R.L. Cicero, T. Eberspacher, C.J. Barrelet, C.C. Chidsey, J. Phys. Chem. B 105 (2001) 10900.
[20] D.J. Michalak, N.S. Lewis, Appl. Phys. Lett. 80 (2002) 4458.
[21] Q. Li, G. Mathur, M. Homsi, S. Surthi, V. Misraa, V. Malinovskii, K.-H. Schweikart, L. Yu, J.S. Lindsey, Z. Liu, R.B. Dabke, A. Yasseri, D.F. Bocian, W.G. Kuhr, Appl. Phys. Lett. 81 (2002) 1494.
[22] Z. Liu, A.A. Yasseri, J.S. Lindsey, D.F. Bocian, Science 302 (2003) 1543.
[23] Y.J. Liu, H.Z. Yu, J. Phys. Chem. B 107 (2003) 7803.
[24] Y.J. Liu, H.Z. Yu, ChemPhysChem 3 (2002) 799.
[25] Y.J. Liu, H.Z. Yu, ChemPhysChem 4 (2003) 335.
[26] N.P. Guisinger, M.E. Greene, R. Basu, A.S. Baluch, M.C. Hersam, Nano Lett. 4 (2004) 55.
[27] C. Engtrakul, L.R. Sita, Nano Lett. 1 (2001) 541.
[28] P. Kruse, E.R. Johnson, G.A. DiLabio, R.A. Wolkow, Nano Lett. 2 (2002) 807.
[29] E.A. Dalchiele, G. Bernardini, F. Cattaruzza, A. Flamini, P. Pallavicini, R. Zanoni, F. Decker, submitted for publication.
[30] D. Briggs, M.P. Seah, Practical Surface Analysis, vol. 1, 2nd ed., J. Wiley & Sons, Chichester, 1990.
[31] M.P. Seah, S.J. Spencer, Surf. Interf. Anal. 33 (2002) 640.
[32] M. Warntjes, C. Vieillard, F. Ozanam, J.-N. Chazalviel, J. Electrochem. Soc. 142 (1995) 4138.
[33] L.C.P.M. de Smet, G.A. Stork, G.H.F. Hurenkamp, Q.-Y. Sun, H. Topal, P.J.E. Vronen, A.B. Sieval, A. Wright, G.M. Visser, H. Zuilhof, E.J.R. Sudhőlter, J. Am. Chem. Soc. 125 (2003) 13916.
[34] Q.-Y. Sun, L.C.P.M. de Smet, B. van Lagen, A. Wright, H. Zuilhof, E.J.R. Sudhőlter, Angew. Chem. Int. Ed. 43 (2004) 1352.
[35] T. Strother, W. Cai, X. Zhao, R.J. Hamers, L.M. Smith, J. Am. Chem. Soc. 122 (2000) 1205.
[36] T. Strother, R.J. Hamers, L.M. Smith, Nucl. Acids Res. 28 (2000) 3535.
[37] R. Boukherroub, S. Morin, D.D.M. Wayner, F. Bensebaa, G.I. Sproule, J.-M. Baribeau, D.J. Lockwood, Chem. Mater. 13 (2001) 2002.
[38] Z. Lin, T. Strother, W. Cai, X. Cao, L.M. Smith, R.J. Hamers, Langmuir 18 (2002) 788.
[39] D. Xu, E.T. Kang, K.G. Neoh, Y. Zhang, A.A.O. Tay, S.S. Ang, M.C.Y. Lo, K. Vaidyanathan, J. Phys. Chem. B 106 (2002) 12508.
[40] F. Karadas, G. Ertas, S. Suzer, J. Phys. Chem. B 108 (2004) 1515.
[41] K. Hricovini, R. Günther, P. Thiry, A. Taleb-Ibrahimi, G. Indlekofer, J.E. Bonnet, P. Dumas, Y. Petroff, X. Blase, X. Zhu, S.G. Louie, T.J. Chabal, P.A. Thiry, Phys. Rev. Lett. 70 (1993) 1992.
[42] R.I.G. Uhrberg, E. Landemark, Y.-C. Chao, J. Electron Spectrosc. Relat. Phenom. 75 (1995) 197.
[43] G.F. Cerofolini, C. Galati, L. Renna, Surf. Interf. Anal. 35 (2003) 968.
[44] M.P. Seah, R. White, Surf. Interf. Anal. 33 (2002) 960.
[45] M.P. Seah, S.J. Spencer, Surf. Interf. Anal. 35 (2003) 515.
[46] C.M. Woodbridge, D.L. Pugmuir, R.C. Jonhson, N.M. Boag, M.A. Langell, J. Phys. Chem. B 104 (2000) 3085.
[47] D.O. Cowan, J. Park, Chem. Commun. 1444 (1971).
[48] P. Daum, R.W. Murray, J. Electroanal. Chem. 103 (1979) 289.
[49] L.M. Han, K. Rajeshwar, R.B. Timmons, Langmuir 13 (1997) 5941.
[50] H.O. Finklea, in: R.A. Meyers (Ed.), Encyclopedia of Analytical Chemistry, John Wiley and Sons Ltd., Chichester, 2000, pp. 1–26.
[51] R.D. Eagling, J.E. Bateman, N.J. Goodwin, W. Henderson, B.R. Horrocks, A. Houlton, J. Chem. Soc., Dalton Trans. 1273 (1998).
[52] E. Laviron, J. Electronal. Chem. 101 (1979) 19.
[53] H. Ju, D. Leech, Phys. Chem. Chem. Phys. 1 (1999) 1549.
[54] J.J. Sumner, S.E. Creager, J. Phys. Chem. B 105 (2001) 8739.

UNCORRECTED PROOF

Curriculum Vitae of
Giovanni DI SANTO

Born: 29 December in 1977 in Campobasso (Italy).

Education:

- University degree: In October 2000 I started my master thesis work in the group of prof. Carlo Coluzza on Scanning Tunneling and Atomic Force Microscopy in UHV conditions. My university degree ("Laurea in Fisica") was awarded by the University "La Sapienza" in 2001 with the grade of 108/110. Thesis title: "A Scanning Tunnelling Microscopy study on metal cluster formation above the reconstructed InAs(100) surface", supervisor: prof. C.Coluzza.

- High school: "Diploma di Liceo Scientifico" in 1996 with the grade of 60/60.

Research Experience:

- 1999 - Stage in the Twente University of Enschede (NL), with an Erasmus-Socrates fellowship. In this period I worked in the solid state physics group learning different surface science techniques: Thermal Helium Atom Scattering (TEAS); Spot Profile Analysis Low Energy Electron Diffraction (SPA-LEED); Auger Electron Spectroscopy (AES); Surface Magneto Optic Kerr Effect (SMOKE).
- Beamtime at Elettra SR facility in Trieste in October 2000 (VUV beamline), April 2002 (EscaMicroscopy), February 2003 (SpectroMicroscopy), March 2003 (EscaMicroscopy), October 2003 (SpectroMicroscopy)

Languages: Italian(mothertongue), English(good written and spoken), French(elementary level)
Hobbies: football, table-tennis and martial arts.

Actual position: In 2001 I started the PhD in Materials Science at "La Sapienza" as a winner of the national fellowship. The PhD thesis title is: "Functionalised crystalline Silicon surfaces for nanoscopic devices". The PhD thesis defence is expected within January 2005.
During the three years of the PhD course of study I was involved in a main project on "Silicon surface functionalization with organics" working in collaboration with proff. C.Coluzza (Phys. Dept), F.Decker and R.Zanoni (Chem. Dept). Further collaborations gave me the opportunity to work also in other research projects.

Research activities:

- The main project, argument of my PhD thesis, is in the field of molecular electronics and its research topics are presented in the following lines. I started from substrate (crystalline Si[100]): H-terminated Si surfaces has been prepared by wet chemistry processes and characterized by AFM and XPS. Then we passed to the functionalization, in three different ways, with organic species like ferrocene-derivated compunds. These organic mono-layers are redox species and their capability of charge transfer after anchoring has been shown by electrochemistry measurements. The project indeed was addressed to the understanding of the basic interactions between the molecules and Si and the development of a simple procedure where the two active part of the hybrid can be integrated in an electronic device. In the last period of my thesis project a novel study technique has been also designed: a soft metal contact by mercury micro-drop on alkyl layer berthed on Si to measure current-voltage characteristics at the junction. Moreover by using monochromatic light, in the visible and near infra-red range, as a pumping probe for controlling the transport mechanisms it is possible to get accurate measurements on the interface properties. Internal Photoemission experimental setup has indeed been built to have information on barrier height at the interface but also to recognize interface states, mainly due to defects, which deeply affect the conduction mechanisms over the junction.

- In parallel my responsibility was the setting up and the maintenance of a new UHV system including a VT-STM/AFM, an XPS analysis chamber and a PEEM. These three technique experimental setup has been designed to achieve a full characterization of a surface both from the point of view of chemical analysis and morphological structuring. This approach was the basis for the different projects I was involved in during my PhD.
- Li intercalation thin films for electrochromic devices in collaboration with the electrochemistry group of prof. F.Decker; surface composition and structure of mixed oxides of In, Ni and V has been studied both on as deposited and aged samples.
- From a collaboration with the thin films lab of ENEA, I investigated the surface chemistry and morphology of thin films (Ag on SiO_2,TiO_2,SiN_x) for optics application by XPS and AFM.
- In collaboration with a research group of INFN in Bari, we found interesting results on CsI photocathodes expecially with PEEM microscope giving rise to a new explanation of reducing quantum efficiency of aged samples. PEEM indeed allows to measure local (in the submicrometer scale) variations of work function, what is very useful to study the local quantum efficiency.

Publications:

- **Growth-induced uniaxial anisotropy in grazing-incidence deposited magnetic films** Sebastiaan van Dijken, Giovanni Di Santo, and Bene Poelsema Appl. Phys. Lett. **77**, 13 (September 2000)

- **Influence of the deposition angle on the magnetic anisotropy in thin Co films on Cu(001)** Sebastiaan van Dijken, Giovanni Di Santo, and Bene Poelsema Physical Review B 63, 104431 (February 2001)

- **Surface evolution of Ni-V transparent oxide films upon Li insertion reactions**. Zanoni, R.; Decker, F.; Coluzza, C.; Artuso, F.; Cimino, N.; Di Santo, G.; Masetti, E. Surface and Interface Analysis (2002), 33(10/11), 815-824

- **Surface analyses of In-V oxide films aged electrochemically by Li insertion reactions.** Coluzza, C.; Cimino, N.; Decker, F.; Di Santo, G.; Liberatore, M.; Zanoni, R.; Bertolo, M.; La Rosa, S. Physical Chemistry Chemical Physics (2003) 5(24), 5489-5498

- **Ellipsometric and XPS analysis of the interface between silver and SiO2, TiO2 and SiNx thin films.** Masetti, E.; Bulir, J.; Gagliardi, S.; Janicki, V.; Krasilnikova, A.; Di Santo, G.; Coluzza, C. Thin Solid Films (2004), 455-456 468-472
- **An afm, xps and electrochemical study of molecular electroactive monolayers formed by wet chemistry functionalisation of H-terminated Si(100) with vinylferrocene** R. Zanoni, F. Cattaruzza, C. Coluzza, E. A. Dalchiele, F. Decker, G. Di Santo, A.Flamini, L. Funari and A.G. Marrani accepted for publication in Surface Science
- **Evidence of time-dependent surface charging using spectro-microscopic techniques** Di Santo G., Decker F.,Zanoni R., Bertolo M., and Coluzza C. in preparation
- **Influence of grain boundaries formation on CsI aged photocathods** Di Santo G., Singh B., De Lucia M. and Coluzza C. in preparation
- **UV-induced radiation aging in CsI thin film photocathodes** B.K. Singh, C. Coluzza, G. Di Santo, E. Nappi, M.A. Nitti, A. Valentini and R. Zanoni in preparation

Schools:

- 2001 School on Syncrothron Light Applications 18-21 October CNR – Area della ricerca di Montelibretti Roma
- 2002 National School on Physics of Matter 9-25 September Villa Gualino – Torino
- 2003 National School on Syncrothron Radiation 13-26 September S.Margherita di Pula (CA)